THE UNIVERSITY of EDINBURGH

Edinburgh Research Explorer

Metabolite-based inter-kingdom communication controls intestinal tissue recovery following chemotherapeutic injury

Citation for published version:
Anderson, CJ, Boeckaerts, L, Chin, P, Cardas, JB, Xie, W, Goncalves, A, Blancke, G, Benson, S, Rogatti Granados, S, Simpson, M, Davey, A, Choi, SM, Desmet, S, Bushman, SD, Goeminne, G, Vandenabeele, P, Desai, MS, Vereecke, L & Ravichandran, KS 2024, 'Metabolite-based inter-kingdom communication controls intestinal tissue recovery following chemotherapeutic injury', *Cell Host & Microbe*. https://doi.org/10.1016/j.chom.2024.07.026

Digital Object Identifier (DOI):
10.1016/j.chom.2024.07.026

Link:
Link to publication record in Edinburgh Research Explorer

Document Version:
Peer reviewed version

Published In:
Cell Host & Microbe

General rights
Copyright for the publications made accessible via the Edinburgh Research Explorer is retained by the author(s) and / or other copyright owners and it is a condition of accessing these publications that users recognise and abide by the legal requirements associated with these rights.

Take down policy
The University of Edinburgh has made every reasonable effort to ensure that Edinburgh Research Explorer content complies with UK legislation. If you believe that the public display of this file breaches copyright please contact openaccess@ed.ac.uk providing details, and we will remove access to the work immediately and investigate your claim.

OPEN ACCESS

Download date: 03. Oct. 2024

Metabolite-based inter-kingdom communication controls intestinal tissue recovery following chemotherapeutic injury

Christopher J. Anderson[1,2,3,9], Laura Boeckaerts[1,2], Pricilla Chin[3], Javier Burgoa Cardas[1,2], Wei Xie[1,2], Amanda Gonçalves[2,4], Gillian Blancke[1,5], Sam Benson[3], Sebastian Rogatti[3], Mariska S. Simpson[3], Anna Davey[3], Sze Men Choi[1,2], Sandrien Desmet[6], Summer D. Bushman[7], Geert Goeminne[6], Peter Vandenabeele[1,2], Mahesh S. Desai[7], Lars Vereecke[1,5], and Kodi S. Ravichandran[1,2,8,9,10]

1. VIB-UGent Center for Inflammation Research, Ghent, Belgium
2. Department of Biomedical Molecular Biology, Ghent University, Ghent, Belgium
3. Centre for Inflammation Research, Institute for Regeneration and Repair, University of Edinburgh, Edinburgh, United Kingdom
4. VIB BioImaging Core, Ghent, Belgium
5. Department of Internal Medicine and Pediatrics, Ghent University, Ghent, Belgium
6. VIB Metabolomics Core, Ghent, Belgium
7. Department of Infection and Immunity, Luxembourg Institute of Health; L-4354 Esch-sur-Alzette, Luxembourg
8. Division of Immunobiology, Department of Pathology and Immunology, Washington University School of Medicine, St. Louis, MO, USA
9. Corresponding authors
10. Lead Contact

Emails of corresponding authors: cj.anderson@ed.ac.uk, kodi@wustl.edu

Lead Contact: Kodi S. Ravichandran; kodi@wustl.edu

Summary:

Cytotoxic chemotherapies have devastating side effects, particularly within the gastrointestinal tract. Gastrointestinal toxicity includes death and damage of the epithelium and an imbalance in the intestinal microbiota, otherwise known as dysbiosis. Whether dysbiosis is a direct contributor to tissue toxicity is a key area of focus. Here, from both mammalian and bacterial perspectives, we uncover an intestinal epithelial cell death-Enterobacteriaceae signaling axis that fuels dysbiosis. Specifically, our data demonstrate that chemotherapy-induced epithelial cell apoptosis, and the purine-containing metabolites released from dying cells, drives the inter-kingdom transcriptional re-wiring of the Enterobacteriaceae, including fundamental shifts in bacterial respiration and promotion of purine utilization-dependent expansion, which in turn delays the recovery of the intestinal tract. Inhibition of epithelial cell death or restriction of the Enterobacteriaceae to homeostatic levels reverses dysbiosis and improves intestinal recovery. These findings suggest that supportive therapies that maintain homeostatic levels of Enterobacteriaceae may be useful in resolving intestinal disease.

Keywords:

Dysbiosis, intestinal epithelium, Enterobacteriaceae, chemotherapy, apoptosis

Introduction

Cytotoxic chemotherapeutics, though largely effective in their primary purpose of killing tumor cells, have long-lasting impacts on a cancer patient's physical and mental health[1]. One of the most common side effects of these drugs, impacting 40-80% of patients, is the onset of gastrointestinal toxicity[2,3]. In addition, chemotherapy-induced intestinal injury restricts the ability of cancer patients to maintain appropriate therapeutic dosing and duration, in turn limiting efficacy[4]. Therefore, a better understanding of intestinal tissue injury and repair in response to these treatments is desperately needed.

Maintaining an appropriately balanced intestinal microbiota is a critical feature of health. Changes to the microbial community, broadly referred to as dysbiosis, occur in a diverse range of intestinal pathologies, including chemotherapy-induced gastrointestinal toxicity[5]. Dysbiosis often involves the enrichment of the Proteobacteria (Pseudomonadota) and the Enterobacteriaceae family of organisms[6] and is similarly observed in treatment-naïve patients with Inflammatory Bowel Disease (IBD) and corresponding animal models[7,8]. Although relationships between intestinal pathologies and dysbiosis are well documented[9,10], the functional implications of the inter-kingdom communication events that shape dysbiosis are unclear[11-14]. While antibiotic therapies are an option to counter dysbiosis[15-19], complications include disruption of the homeostatic microbiota and lowering "colonization resistance", which makes it easier for invading pathogens[20]. The benefits of therapeutic interventions that seek to maintain the homeostatic microbial community are less explored.

Many gastrointestinal pathologies, including chemotherapy-induced intestinal toxicity and IBD, display increases in regulated cell death during disease[5,21]. Regulated cell death, in particular caspase-dependent apoptosis, is an essential part of homeostasis and development[22], and the coordinated response to dying cells is paramount for tissue health[23]. However, the role that apoptotic cells play in re-establishing homeostasis, both mammalian and microbial, during intestinal injury has remained undefined. Thus, we set out to address the underlying relationship between cell death, bacterial dysbiosis, and intestinal disease.

Results

Linkage between intestinal epithelial apoptosis, tissue damage, and dysbiosis during chemotherapy

Doxorubicin, an anthracycline, is an actively used cancer chemotherapeutic targeting a diverse range of tumors[24] that frequently causes intestinal toxicity and mucositis[25]. To better understand the factors involved in gastrointestinal disease, we utilized a mouse model of doxorubicin toxicity[26]. Briefly, mice received a single systemic dose of doxorubicin and were monitored for signs of disease (Figure 1A). Typically, mice lost weight (Figure 1B) and had shortened colons (Figure 1C) within the first 2-3 days before returning to baseline weight by day 7. Doxorubicin induces intestinal stem cell death within the crypts of the small intestine[27], and we observed a significant increase in dead cells (TUNEL$^+$) with maximal staining coinciding with peak disease (Figure 1D-E). Interestingly, we also observed dying cells along the tips of the intestinal villi that appeared to be in the process of being shed into the lumen (Figure 1D). Given that intestinal epithelial cells can undergo different forms of regulated cell death, we probed for specific cell death effectors. Following doxorubicin administration *in vivo*, intestinal epithelial cells prominently engaged the apoptotic caspases (Figure 1F), increased TUNEL positivity at day 2 after treatment (Figure S1A), stained positive for cleaved caspase 3 in the lumenal space (Figure S1B), and did not substantially activate other forms of regulated cell death (Figure S1C). Further, we noted that doxorubicin also activated colonic apoptosis (Figure S1D-E).

Mucositis is one of the most common and severe side effects for cancer patients receiving doxorubicin, a process that significantly impacts therapeutic dosing and duration[28]. Typical signs of mucositis include structural changes to the intestinal villi, increasing numbers of mucus-producing goblet cells, and inflammation[27,29]. Indeed, doxorubicin-treated animals exhibited striking mucoid pathology, increased immune cells, and greatly expanded the number of Alcian Blue and Periodic Acid-Schiff (AB-PAS) positive cells within small intestine[30] (Figure S2A-E). To confirm this, we stained sections with the lectin UEA1[31,32] and noted that doxorubicin treatment significantly increased ileal mucus production and the number of mucus-producing cells (Figure 1G-H, Figure S2F); but not within the colon where baseline mucus production was much higher (Figure S2G). Interestingly, the hyperproduction of mucus persisted beyond the peak of cell death.

We next asked how epithelial cell apoptosis may link to microbial dysbiosis. Given the physical proximity between the apoptotic intestinal epithelial cells and the microbial community, and that pathogenic bacteria can use nutrients released from apoptotic cells for growth[33], we hypothesized that such inter-kingdom nutrient exchange may underlie some of the dysbiosis associated with chemotherapy. The commensal Enterobacteriaceae population, which we identified as a mouse commensal strain of *Escherichia coli* (*E. coli*)[33], was relatively low in untreated control mice; however, doxorubicin administration triggered a significant enrichment of Enterobacteriaceae throughout the intestinal tract and spleen, with an approximately 10,000 to one million-fold increase in tightly adherent or invasive 'tissue-associated' bacteria within the first day (Figure 1I). The Enterobacteriaceae bloom could be monitored by collecting daily fecal samples and shedding of commensal *E. coli* mirrored the kinetics of tissue-associated burden (Figure 1J), with peak Enterobacteriaceae expansion aligning with peak epithelial cell apoptosis. Thus, doxorubicin administration in mice recapitulates the induction of intestinal cell death, mucositis, and dysbiosis that is frequently observed in patients. Further, the overlap and similarity in kinetics suggested that there might be a potential link between these three hallmark events.

Epithelial apoptosis drives acute disease and dysbiosis

To test the connection between intestinal epithelial cell apoptosis, mucositis, and/or dysbiosis, we utilized mice deficient in apoptotic executioner caspases 3 and 7 specifically within the epithelial cell compartment; for this, we crossed villin-Cre transgenic mice to mice carrying floxed alleles of caspase 3 and caspase 7 (*Vil-Cre*$^{Tg/wt}$::*Caspase 3/7*$^{fl/fl}$). These mice are normal at homeostasis and do not develop spontaneous disease or dysbiosis[34]. At a systemic level, doxorubicin was comparably toxic to both control and apoptosis-deficient mice (Figure S3A). However, the apoptosis-deficient mice were significantly protected from intestinal disease. Apoptosis-deficient mice were protected from doxorubicin-induced cell death (Figure 2A), had significantly less weight loss (Figure 2B), and complete protection from treatment-driven reductions in cecal weight and in colon length (Figure 2C) compared to littermate controls. Even further, apoptosis-deficient animals had a significant reduction in doxorubicin-driven mucus hypersecretion (Figure 2D-E) and protection from reductions in ileal mucosal thickness (Figure 2F). These data established that the induction of epithelial apoptosis is instrumental in the downstream development of intestinal disease.

Normally, the lumenal Enterobacteriaceae population is relatively low in healthy mice and humans; consistent with this, untreated control animals exhibited a very stable Enterobacteriaceae population (Figure S3B-C). Following doxorubicin administration, the Enterobacteriaceae bloom was significantly blunted in apoptosis-deficient mice. While littermate control animals displayed the expected 10,000-fold increase in *E. coli* within the first day after treatment, *Vil-Cre*$^{Tg/wt}$::*Caspase 3/7*$^{fl/fl}$ mice showed much smaller expansion, with some animals failing to expand the Enterobacteriaceae population altogether (Figure 2G).

Members of the Enterobacteriaceae family benefit from additional species within the commensal community releasing sugars from host-produced mucus[35]. To test whether epithelial apoptosis could induce the Enterobacteriaceae bloom independently of rampant mucus production, we treated mice with a nonlethal dose of cisplatin, a platinum-based chemotherapeutic agent. Cisplatin induces time and dose-dependent intestinal apoptosis and villi damage in rodent systems[36-38] and has a high incidence of gastrointestinal toxicity in humans[39]. However, in contrast to doxorubicin, cisplatin treatment reduces the number of goblet cells in mice[40]. Following a single systemic injection of cisplatin, wildtype mice exhibited sustained weight loss (Figure S3D) but did not display prolonged signs of intestinal disease (Figure S3E) or reductions in spleen weight (Figure S3F). However, wildtype animals did undergo an Enterobacteriaceae bloom, with increases in tissue-associated (Figure S3G) populations of *E. coli* [41]. In agreement with prior studies, cisplatin triggered cell death in both the ileum and colon without increasing the number of mucus producing cells or mucus production in the ileum (Figure S3H-J) and decreased mucus producing cells and mucus production in the colon (Figure S3K-M). Interestingly, the apoptosis-deficient mice were not protected from cisplatin-induced weight loss (Figure S3N) and maintained similar colon lengths (Figure S3O) and spleen weights as controls (Figure S3P). Control animals displayed much more gradual increases in lumenal Enterobacteriaceae following cisplatin treatment (Figure 2H-I). However, *Vil-Cre*$^{Tg/wt}$::*Caspase 3/7*$^{fl/fl}$ mice had complete abrogation of the peak Enterobacteriaceae bloom (Figure 2J). Collectively, these data demonstrate that epithelial cell apoptosis is an upstream driver of chemotherapy-induced dysbiosis, independent of intestinal mucositis. Further, although epithelial cell apoptosis and dysbiosis are not sufficient to promote mucositis, epithelial apoptosis is necessary for full-fledged disease when mucositis is induced.

Chemotherapy-driven dysbiosis imparts a conserved microbial gene signature

At this point, we surmised that doxorubicin or cisplatin-mediated apoptosis induces transcriptional changes in the microbiota that would promote dysbiosis. To test this, we undertook comprehensive unbiased approaches to uncover microbial transcriptional changes during dysbiosis, ask whether there is a specific death-dependent Enterobacteriaceae response, and match bacterial transcriptional response patterns to specific death-dependent metabolites.

To reveal the active transcriptional responses of the microbial community, we performed metatranscriptomic analyses during dysbiosis *in vivo* (Figure 3A)[42]. Here, we chose to profile the metatranscriptome of the cecal microbiota because the cecum displayed the highest magnitude and consistency in dysbiosis and the selected time points represented the peak onset of the Enterobacteriaceae bloom for each chemotherapy. Strikingly, the transcriptional profile of the microbiota from control, doxorubicin, or cisplatin-treated animals were distinct from one another (Figure 3B, Figure S4A), and were significantly different in transcriptional diversity (Figure 3C, Figure S4B-C). Given the differences in time post-treatment and disease status that may complicate any comparisons across chemotherapies, we next attempted to identify common transcriptional signatures compared to untreated animals.

First, aerobic respiration gene signatures were significantly enriched by treatment with either cytotoxic agent. Aerobic respiration drives Enterobacteriaceae expansion and is a feature commonly identified within the inflamed gut[43-45]. Genes associated with aerobic respiration were detected at low levels during homeostasis but were significantly increased during peak dysbiosis induced by either chemotherapy (Figure 3D). This was further supported by an enrichment of associated GO terms (Figure S4D). Therefore, our findings identify a shared signature between chemotherapy-induced dysbiosis and diseases displaying inflammation-driven dysbiosis, such as IBD.

Second, both chemotherapies reduced the expression of seven distinct gene clusters related to purine biosynthesis and salvage (Figure 3E) and increased the expression of genes related to purine ribonucleoside degradation (Figure 3F). These metatranscriptomic data strongly suggest that cytotoxic chemotherapies impart functional alterations in bacterial metabolism that likely influence dysbiosis.

Epithelial apoptosis reprograms *E. coli* metabolic pathways

The complexity of the intestinal tract makes it difficult to directly attribute bacterial gene expression changes to epithelial cell death. To understand how cytotoxic chemotherapy influences the Enterobacteriaceae population, we designed an *in vitro* model system where “donor” intestinal epithelial cells, in the absence of bacteria, were treated with doxorubicin with or without a pan caspase inhibitor (QVD) to block apoptosis (Figure S4E). Following treatment, mammalian cell-free supernatants were collected and used as a growth medium and the “recipient” *E. coli* transcriptional response was profiled (Figure 3G). We utilized the murine colonic cell line CT26, which transcriptionally mirror healthy primary epithelial cells[46], and confirmed similar sensitivity in a human colonic epithelial cell line (HCT116; Figure S5A-B). The resultant *E. coli* transcriptional profiles were distinct from one another, revealing significant mammalian apoptosis-dependent changes (Figure 3H).

As seen in our *in vivo* systems, doxorubicin-treated supernatants induced the expression of pathways related to aerobic respiration and amino acid biosynthesis (Figure S5C). Specifically, mammalian supernatants increased the expression of *E. coli* genes involved in aerobic respiratory complex 1 (Figure 3I) and cytochrome c (Figure S5D) in an apoptosis-dependent fashion. Concurrently, apoptotic supernatants significantly downregulated anaerobic respiration genes, most notably the genes involved in molybdopterin biosynthesis[43,47] (Figure 3J). The production of molybdenum, a structural component of molybdopterin, is incorporated into the active site of nitrate, S-oxide, and N-oxide reductases and is thus required for bacterial growth across a spectrum of alternative electron acceptors. These findings were surprising given that these transcriptional studies were performed under standard aerobic culture conditions (approximately 17% O_2) and suggest that mammalian-derived death-dependent soluble factors can act as accessory signals to rewire respiration-associated gene expression.

With regards to amino acid biosynthesis, growth in apoptotic supernatants significantly increased *E. coli* histidine biosynthesis genes (Figure S5E). Histidine biosynthesis splits from purine biosynthesis from a common precursor[48], and the purine biosynthesis fork was simultaneously decreased (Figure S5F). Concomitantly, recipient *E. coli* up-regulated genes to incorporate exogenous sources of purine-related molecules; specifically, expression of multiple purine transporters[49,50] (Figure 3K) and multiple purine hydrolases, including *rihC*[51] (Figure 3L) were significantly up-regulated. Bacteria, including *E. coli*, can breakdown purines to use as a carbon source under anaerobic conditions[52]. However, in our aerobic system, expression of these genes were not detected. Besides carbon sources, purines are also essential building blocks for DNA replication and energy production (i.e., ATP/GTP). Along these lines, death-dependent mammalian donor cell secretions significantly enhanced *E. coli* ATP synthase gene expression (Figure S5G).

Collectively, these data recapitulate the notable findings from our complex *in vivo* metatranscriptomics dataset and show that apoptosis drives the ability of responding *E. coli* to shift to aerobic respiration metabolism and purine uptake and utilization.

Chemotherapeutic agents trigger epithelial cell death-dependent metabolite profile

The above data strongly suggested that the metabolite secretome of apoptotic epithelial cells heavily influences the transcriptional profile of the intestinal microbiota. Thus, we performed unbiased metabolomics of epithelial cell supernatants treated with chemotherapeutics in the absence of bacteria. To identify specific apoptotic mechanisms of action, we compared three drugs: doxorubicin and cisplatin (which both target DNA to induce apoptosis) and staurosporine (which induces apoptosis via kinase inhibition) (Figure 4A), and each induced similar levels of caspase-dependent death (Figure S4E, Figure S6A). LC-MS analysis detected 9,985 unique m/z features, of which nearly half were significantly altered in at least one test condition. We performed a principal component analysis of significant features and observed clear clustering and separation from apoptosis-inhibited counterparts (Figure 4B). Within the list of significant features, we performed hierarchical cluster analysis to identify targets that were significantly enriched in all three cancer drug treatments and were apoptosis-dependent, resulting in 114 features (Figure 4C; Figure S6B). Structural annotation of these features was then attempted via *in silico* fragmentation using MS-Finder and 40 were determined to have a potential structural match to known metabolites. The best result for 65% of those structurally characterized features had a nucleobase backbone in combination with a pentose and phosphate substructure. This included 11 features with a purine substructure, 6 with a pyrimidine substructure, and 9 with both substructures all carrying 1 or more phosphate groups and a pentose (or derivative). In particular, this list included adenosine monophosphate (AMP) isomers and guanosine monophosphate (GMP) (Figure 4D), whose identities were confirmed by reference standards.

Death-dependent metabolites rewire *E. coli* transcription

To correlate host-derived metabolites present within the chemotherapeutic-induced apoptotic secretome with bacterial transcriptional responses, we focused on death-dependent metabolites with known biological functions. A group of 6 core apoptotic metabolites, including purine ribonucleoside monophosphates, critically impact mammalian signalling[53]. To test how these core death-dependent metabolites alter *E. coli* gene expression, we performed RNA sequencing of *E. coli* grown with or without supplementation of the 6-metabolite mixture (M6) or a 3-metabolite mixture (M3) (Figure 5A). Supplementation with either apoptotic metabolite cocktail significantly altered *E. coli* transcription (Figure 5A), with purine biosynthesis genes some of the most highly regulated genes (Figure S7A). Pleasingly, metabolite supplementation alone was able to recapitulate increased expression of genes for purine transport (Figure S7B), purine ribonucleoside hydrolases (Figure 5B), histidine biosynthesis (Figure S7C), and ATP synthase (Figure S7D).

Unexpectedly, we observed *E. coli* transcriptional changes to both anaerobic and aerobic respiration machinery grown in the presence of death-dependent metabolites. Supplementation with metabolite mixtures significantly down-regulated anaerobic respiration (Figure 5C) while increasing genes encoding for aerobic respiratory complex 1 (Figure 5D) and cytochrome c (Figure S7E). These findings reveal the sufficiency of chemotherapy-induced mammalian apoptotic metabolites, including purine containing metabolites, to prime *E. coli* for adaptation to an aerobic environment.

Death-responsive *E. coli* genes promote intestinal colonization

To determine the functional relevance of the observed apoptosis-dependent transcriptional reprogramming, we performed competitive *E. coli* infections *in vivo* (Figure 5E). Briefly, mice were infected with a 1:1 ratio (input) of wildtype and mutant strains of *E. coli* and the relative fitness of the two strains (output) was assessed. Untreated animals had undetectable levels of exogenously introduced *E. coli* in both ileum and colon and roughly 10,000-fold lower levels in the cecum compared to doxorubicin treated mice (Figure 5F); therefore, bacterial fitness with or without doxorubicin could only be compared within the cecum. To distinguish exogenously introduced *E. coli* from the blooming endogenous population, we generated unresolved deletions of *lacZ* with chromosomal insertions of either chloramphenicol (Chl^R) or kanamycin (Kan^R) resistance cassettes, which does not impact Enterobacteriaceae colonization[54] (Table 1). Importantly, the two antibiotic selection cassettes did not influence competitive index analyses (Figure 5G).

Given that our data suggest an apoptosis-dependent shift away from anaerobic respiration, we first tested a series of anaerobic respiration-deficient strains. Anaerobic respiration pathways are critical for the Enterobacteriaceae to colonize antibiotic-treated animals[55] while intestinal inflammation drives increased *moaA*-dependent[56], nitrate-dependent[56,57] and hydrogen peroxide-dependent[47] fitness. In contrast to general inflammation, doxorubicin treatment significantly reduced *moaA*-dependent fitness and did not induce either nitrate or hydrogen peroxide-dependent fitness (Figure 5H-J), which is in line with *in vitro* gene expression (Figure 3J, Figure S8A). Importantly, similar competitive indices were observed across the intestinal tract following doxorubicin treatment (Figure S8B-D). We next tested the impact of the high oxygen affinity cytochrome CydAB system, which is important for growth in low oxygen abundance[58]. Apoptotic supernatants significantly decreased expression of *cydAB* (Figure S8E) and this system was completely dispensable following doxorubicin treatment *in vivo* (Figure S8F-G) indicating that the doxorubicin-induced intestinal environment has no functional requirement for the high-affinity, low oxygen abundance cytochrome.

Finally, to assess the impact of purine utilization, we constructed a mutant strain of *E. coli* that lacks purine hydrolases. One hydrolase, *adk*, is essential for *E. coli* viability[59] so we constructed a strain deficient for both *rihC* and *ndk*. This purine hydrolase-deficient mutant had a significant fitness defect following doxorubicin treatment (Figure 5K) throughout the various intestinal compartments (Figure S8H), demonstrating the functional requirement of this death-induced program. Importantly, none of the mutants used *in vivo* had any growth defects *in vitro* (Figure S8I).

Collectively, the combination of unbiased approaches revealed that epithelial cell apoptosis leads to the release of metabolites that alter specific transcriptional programs within the intestinal microbiota and to modify bacterial metabolism and drive Enterobacteriaceae expansion.

Targeted antibiotic therapy improves intestinal recovery

Chemotherapy enriches Enterobacteriaceae abundance in human cancer patients[5,60]; however, it remains unclear if the Enterobacteriaceae bloom is an active driver of gastrointestinal toxicity. During the course of our studies, we accidentally noticed that a proportion of our internal mouse colony had undetectable levels of Enterobacteriaceae prior to treatment. The ‘uncolonized mice’ returned to baseline weights faster after doxorubicin treatment compared to *E. coli* colonized littermates (Figure 6A), suggesting that the abundance of this organism could be a predictive indicator of recovery.

While previous studies using broad-spectrum antibiotic pre-treatment and germ-free mice highlighted the importance of the microbial community at the time of injury[61,62], we asked whether the actively changing microbiota influences tissue recovery. We devised an antibiotic intervention strategy wherein mice were administered oral antibiotics concurrently with doxorubicin injection (Figure 6B). Mice received oral therapy with the Gram-positive targeting antibiotic vancomycin, the Gram-negative targeting aztreonam and polymyxin B, or vehicle (water) with doxorubicin injection. As with prior cohorts, mice receiving doxorubicin alone displayed a 10,000-fold increase in lumenal Enterobacteriaceae (Figure 6C; Figure S9A). Treatment with vancomycin, which kills many Enterobacteriaceae competitors[63], prolonged dysbiosis while the Gram-negative targeting cocktail completely blunted the Enterobacteriaceae bloom in fecal samples (Figure 6C; Figure S9A). Importantly, this antibiotic intervention strategy restricted Enterobacteriaceae abundance to near homeostatic levels (Figure 6D). In the absence of the Enterobacteriaceae bloom, mice had an accelerated recovery from injury including faster weight improvement, improved mucosal thickness, fewer mucus-producing cells, and less mucus production compared to mice that received doxorubicin alone (Figure 6E-I). These data suggest that chemotherapy-induced dysbiosis, and possibly the Enterobacteriaceae bloom, is a contributor to host disease. Further, the total abundance of the Enterobacteriaceae, rather than a binary presence, is critical to recovery.

Enterobacteriaceae bloom delays intestinal recovery

We next sought to solidify the link between the Enterobacteriaceae abundance and changes in disease state. For this, we modified two factors that improve disease outcome: time and antibiotic intervention, with the hypothesis that disease-relevant changes would be ablated by both factors (Figure 7A). Despite improvements in weight loss for both interventions, the microbial communities remained distinct by Beta Diversity and principal component analysis (Figure 7B-C). We observed a variety of total abundances across treatment conditions (Figure S10A), including some phyla that did not change and some that were time-dependent but antibiotic insensitive (Figure 7D). In contrast, the Proteobacteria (Pseudomonadota, which include the Enterobacteriaceae) fit our predicted pattern in that they were significantly enriched post-doxorubicin treatment but were found at homeostatic abundance following either antibiotic intervention or time-dependent resolution (Figure 7D, Figure S10B-C). Thus, these data suggest targeting the Enterobacteriaceae could be useful for influencing intestinal disease state.

Next, we devised a strategy to directly test the impact of one single species of Enterobacteriaceae (*E. coli*) on intestinal recovery. Previous studies have identified and utilized a defined 14-member microbial community derived from human stool samples, which includes *E. coli*[64,65]. We re-colonized germ-free mice with this synthetic human microbiota containing *E. coli* (14-SM) or the same community without *E. coli* (13-SM) and then treated these mice with doxorubicin (Figure 7E, Figure S10D). Treatment of germ-free mice with doxorubicin failed to induce weight loss or cecal damage (Figure 7F-G) compared to untreated germ-free controls. Importantly, reconstitution with the 14-SM community restored significant weight loss and cecal damage, that was completely lost with the omission of *E. coli* (13-SM mice). Although germ-free animals do not display doxorubicin-induced expansion of mucus-producing cells[61], re-colonization of germ-free mice with the full 14-SM community was able to restore intestinal mucositis (Figure 7H-K). Remarkably, removal of *E. coli* alone was sufficient to significantly protect these animals from pronounced mucositis, including significantly less mucus production and fewer mucus-producing cells (Figure 7H-K). These data, using both antibiotic interventions defined reconstitution of germ-free mice, demonstrate that chemotherapy-induced dysbiosis is not merely a symptom of intestinal disease, rather that the Enterobacteriaceae bloom specifically contributes to the malady. These data agree with models of colitis[66] and suggest that the influence of the Enterobacteriaceae bloom may be widespread across different intestinal pathologies.

Discussion

Whether to view dysbiosis as occurring in response to intestinal disease or driving the disease process is a challenge[9], as clinical trials trying to target the microbiota in cancer patients receiving chemotherapy have produced conflicting results[16-19]. Here, we provide compelling pre-clinical data indicating that the Enterobacteriaceae bloom specifically contributes to disease outcome. Our data also suggest a threshold of tolerance that may be crossed during dysbiosis that negatively impacts tissue health. A better understanding of this threshold may lead to better diagnostic or disease prognosis indicators relevant to patient care and may extend beyond models of chemotherapy-induced gastrointestinal toxicity. Even further, changing the desired clinical outcome from complete sterilization of specific microbes to homeostatic maintenance may resolve conflicting clinical trial results.

Our data raise the question of what benefit there is to the host to shed apoptotic epithelial cells from the barrier if these dying cells are such potent inducers of dysbiosis. Failure to extrude apoptotic cells from the epithelial barrier can shift the apoptotic process into a pro-inflammatory one[67]. Thus, for the good of the tissue, these apoptotic cells must be shed. This renders the apoptotic process vulnerable to microbial exploitation in external environment-facing tissues like the intestinal tract. As host cells have elaborate networks to ensure cell death[68], and dying cells must be shed from the epithelial barrier[67], targeting the bacterial response may be the best bet for improving disease outcome.

Unexpectedly, we discovered that death-dependent soluble factors, including purine containing metabolites, are sufficient to alter aerobic and anaerobic respiration gene signatures. Traditionally, the presence of electron acceptors (oxygen, nitrate, etc) are thought to drive gene regulation due to the differential redox potential of each electron acceptor[69]. In contrast, our data suggest that epithelial cell death-dependent factors act as accessory signals to fine tune these critical transcriptional programs. Our findings place epithelial apoptosis as a biological source of these critical metabolites during intestinal pathology and may have wide-reaching implications across host-microbe interactions, as purine availability and utilization are critical components of additional bacterial pathogens[70] and have been implicated in the bacterial response during IBD[71].

Our current study provides justification for further investigation into the potential of therapeutically targeting the intestinal Enterobacteriaceae to improve recovery time from injury. Our findings are in line with work using DSS colitis; however, *E. coli* utilize anaerobic respiration to expand within this DSS colitis context[66]. One possible explanation for such differences is the modalities of programmed cell death that each trigger induces. While chemotherapy treatment and IBD patients frequently display signs of apoptosis[21], mouse models of DSS colitis depend, at least in part, on pyroptosis machinery[72]. Although specific metabolic pathways may be associated with particular intestinal insults and forms of programmed cell death, continued investigation may reveal a wider applicability across additional pathologies with known Enterobacteriaceae blooms including cancer patients, IBD/Crohn's Disease, and intestinal infections.

Acknowledgements: We thank members of the Ravichandran laboratory, particularly Irina Lambertz, and members of the Edinburgh Cell Death Collective for discussions and input on this work and manuscript. We thank the IRC-VIB BioImaging Core for training, support, and access to the instrument park. We thank the Germ-Free and Gnotobiotic Mouse Facility (UGent/UZ Gent/VIB), particularly Vanessa Andries, for support and Stephanie Willieme for help preparing the synthetic microbiota cocktails. We thank the IRC-VIB IT services for computational server support. C.J.A was supported by a FWO Postdoctoral Fellowship (1225421N), a Young Investigator Proof-of-Concept from the Cancer Research Institute Gent, and is currently supported by a Wellcome Trust Career Development Award (225923/Z/22/Z). K.S.R. is supported by FWO (Odysseus grant G0F5716N, EOS DECODE 30837538), Special Research Fund UGent (iBOF BOF20/IBF/037), European Research Council (ERC) under the European Union's Horizon 2020 research and innovation programme (grant agreement no. 835243). L.V. is supported by Ghent University (BOF.GOA031-22, BOF.IBF037-20), the FWO (EOS-747 G0H2522N-40007505) and Foundation against Cancer (F/2020/1421). M.S.D is supported by the Luxembourg National Research Fund (FNR) CORE grants (C15/BM/10318186 and C18/BM/12585940) and BRIDGES grant (22/17426243). P.V is supported by Special Research Fund UGent (Methusalem grant BOF16/MET_V/007, iBOF ATLANTIS grant 20/IBF/039) and grants from the Foundation against Cancer (F/2016/865, F/2020/1505). For the purpose of open access, the authors have applied a Creative Commons Attribution (CC BY) licence to any Author Accepted Manuscript version arising from this submission.

Author Contributions: C.J.A and K.S.R designed all experiments, supervised the work, and wrote the manuscript. C.J.A performed most experiments. L.B, S.M.C, G.B, A.G, W.X, P.C, S.B, S.R, M.S.S, and A.D performed some experiments. J.B.C performed RNA sequencing analyses. S.D and G.G performed, analyzed, and provided conceptual advice for LC-MS. P.V provided conceptual advice, mice, and reagents. M.S.D provided conceptual advice and synthetic microbiota (SM) cocktails and S.D.B assisted with preparation of SM cocktails. L.V provided conceptual advice and mice for germ-free and gnotobiotic experiments.

Declaration of Interests

Mahesh S. Desai works as a consultant and an advisory board member at Theralution GmbH, Germany. The other authors declare no competing financial interests.

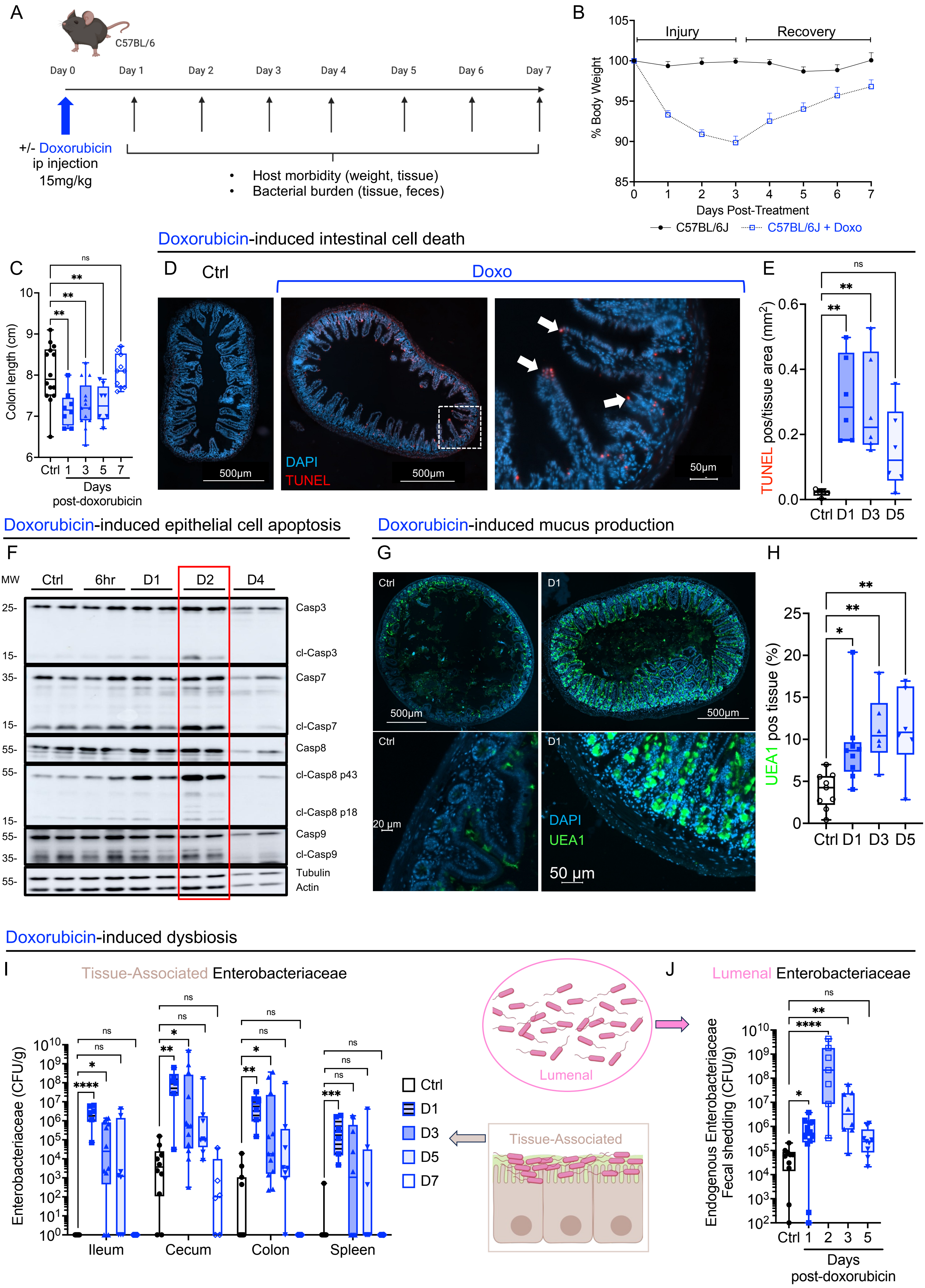
A
C57BL/6
Day 0
Day 1
Day 2
Day 3
Day 4
Day 5
Day 6
Day 7
+/- Doxorubicin
ip injection
15mg/kg
Host morbidity (weight, tissue)
Bacterial burden (tissue, feces)
B
Injury
Recovery
% Body Weight
105
100
95
90
85
0 1 2 3 4 5 6 7
Days Post-Treatment
C57BL/6J
C57BL/6J + Doxo
Doxorubicin-induced intestinal cell death
C
ns
**
**
**
Colon length (cm)
10
9
8
7
6
Ctrl 1 3 5 7
Days
post-doxorubicin
D
Ctrl
Doxo
DAPI
TUNEL
500µm
500µm
500µm
50µm
E
ns
**
**
TUNEL pos/tissue area (mm²)
0.6
0.4
0.2
0.0
Ctrl D1 D3 D5
Doxorubicin-induced epithelial cell apoptosis
F
MW
Ctrl
6hr
D1
D2
D4
25-
15-
35-
15-
55-
55-
15-
55-
35-
55-
Casp3
cl-Casp3
Casp7
cl-Casp7
Casp8
cl-Casp8 p43
cl-Casp8 p18
Casp9
cl-Casp9
Tubulin
Actin
Doxorubicin-induced mucus production
G
Ctrl
D1
500µm
500µm
Ctrl
D1
20 µm
DAPI
UEA1
50 µm
H
**
**
*
UEA1 pos tissue (%)
25
20
15
10
5
0
Ctrl D1 D3 D5
Doxorubicin-induced dysbiosis
I
Tissue-Associated Enterobacteriaceae
ns
ns
*
****
ns
ns
*
**
ns
ns
*
**
ns
ns
ns
***
Enterobacteriaceae (CFU/g)
10^{10}
10^{9}
10^{8}
10^{7}
10^{6}
10^{5}
10^{4}
10^{3}
10^{2}
10^{1}
10^{0}
Ileum
Cecum
Colon
Spleen
Ctrl
D1
D3
D5
D7
Lumenal
Tissue-Associated
J
Lumenal Enterobacteriaceae
ns
**
****
*
Endogenous Enterobacteriaceae
Fecal shedding (CFU/g)
10^{10}
10^{9}
10^{8}
10^{7}
10^{6}
10^{5}
10^{4}
10^{3}
10^{2}
Ctrl 1 2 3 5
Days
post-doxorubicin

Figure 1. Doxorubicin-induced acute dysbiosis correlates with epithelial apoptosis.

- **A.** Schematic of doxorubicin injection created with BioRender.com.
- **B.** Weight loss of control (n= 12) or doxorubicin-treated (n= 18) wildtype C57BL/6J mice across 4 cohorts. Daily weight measurements were normalized to the starting (day 0) weight of each mouse to calculate % body weight. Mean + standard deviation is shown.
- **C.** Colon length (cm) of control untreated or mice at the indicated days post-doxorubicin treatment (n= 8-14, n=3 cohorts). Significance determined by one-way ANOVA with Holm-Sidak multiple comparisons test.
- **D.** Representative DAPI and TUNEL stained images of the ileum of control untreated or day 1 post-doxorubicin treated animals. Dotted white box (center) indicates enhanced region (right). White arrows indicate TUNEL positive cells.
- **E.** TUNEL positive cells per ileum tissue section area (mm^2) at indicated days post-doxorubicin (n= 5-6 mice per group, averaged values of 5-10 sections per mouse shown, n=2 cohorts).
- **F.** Immunoblot of the indicated apoptosis or loading control (tubulin, actin) proteins. Cell lysates were prepped from ileal intestinal epithelial cells isolated at the indicated time post-doxorubicin treatment *in vivo* (n= 2 per time point shown, representative of n=6 samples per time point across n=3 gels).
- **G.** Representative DAPI and UEA1 stained ileal tissue sections of control untreated or day 1 post-doxorubicin treated animals.
- **H.** UEA1 positive fluorescence as a percentage of ileum tissue area (n= 6-9 mice per group, averaged values of 5-10 tissue sections per mouse shown, n=2 cohorts).
- **I.** Tissue-associated Enterobacteriaceae levels within the indicated tissue compartments at the indicated times post-doxorubicin treatment. Colony forming units (CFU) per gram of tissue weight (n= 6-12 per time point, n=3 cohorts).
- **J.** Enterobacteriaceae CFU per gram of fecal content from wildtype C57BL/6J mice at the indicated day post-doxorubicin treatment (n= 9-13 per time point, n=3 cohorts).

For **A-J**: ns $p > 0.05$, * $p \leq 0.05$, ** $p \leq 0.005$, *** $p \leq 0.0005$, **** $p \leq 0.0001$.

For **E, H**: Significance determined by one-way ANOVA with Dunnett's multiple comparisons test.

For **I-J**: Significance determined by Kruskal-Wallis with Dunn's multiple comparisons test comparing each time point to control.

For **C, E, H, I, J**: Box and whiskers show minimum to maximum values with all independent replicates, center denotes median, and the bounds denote the 25th to 75th percentiles.

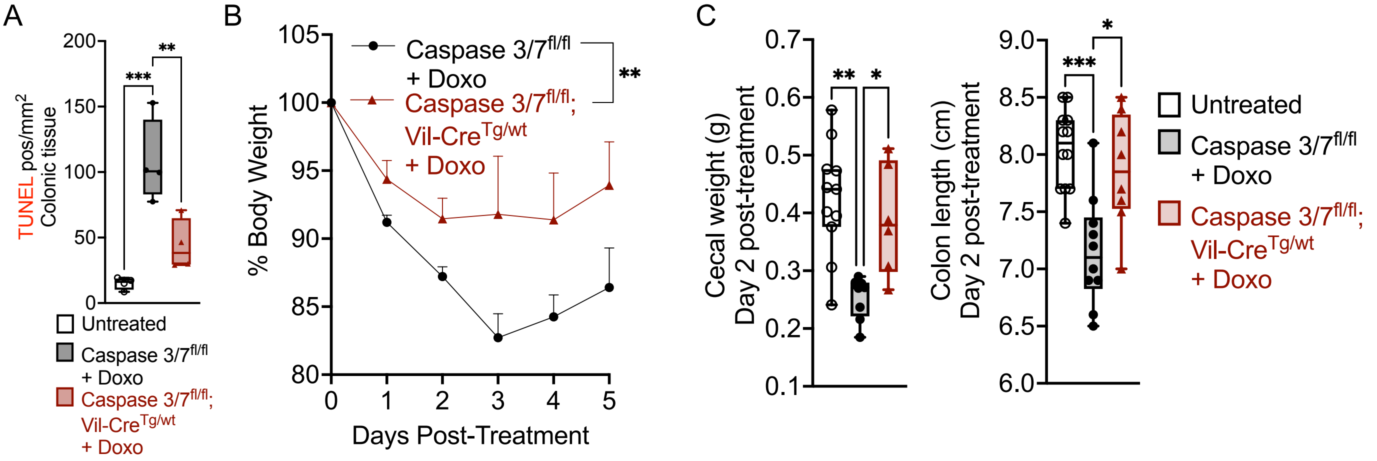

Doxorubicin-induced, Caspase 3/7-dependent mucus production

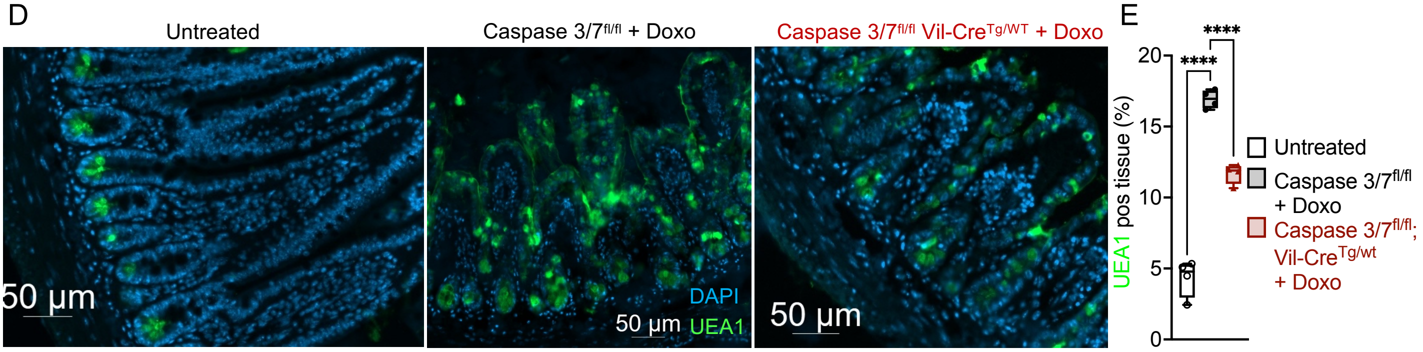

Doxorubicin-induced, Caspase 3/7-dependent dysbiosis

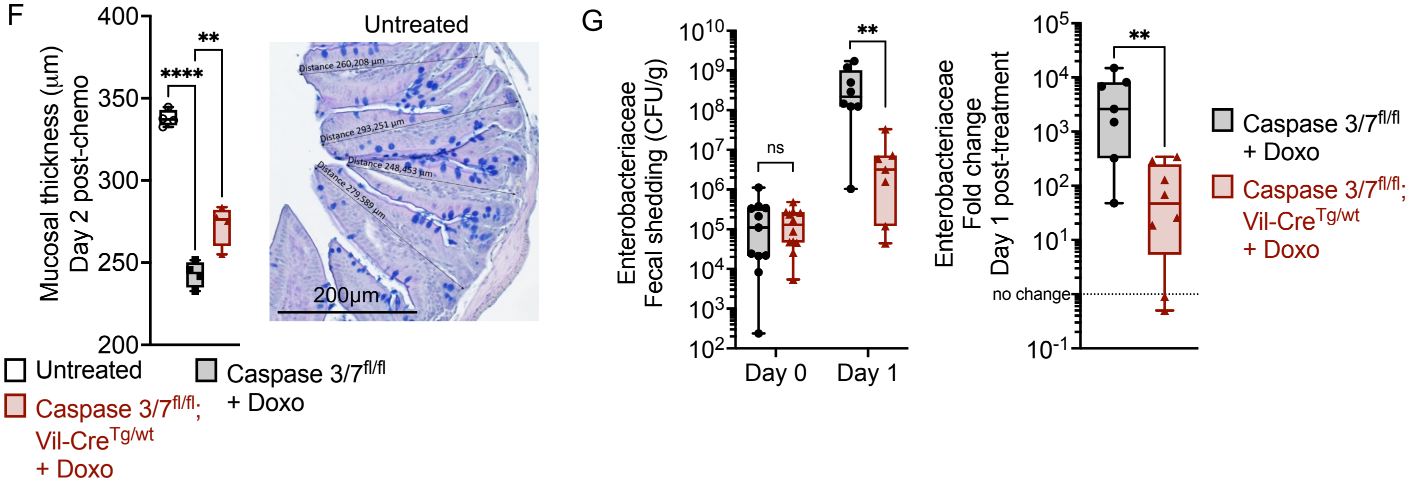

Cisplatin-induced, Caspase 3/7-dependent dysbiosis

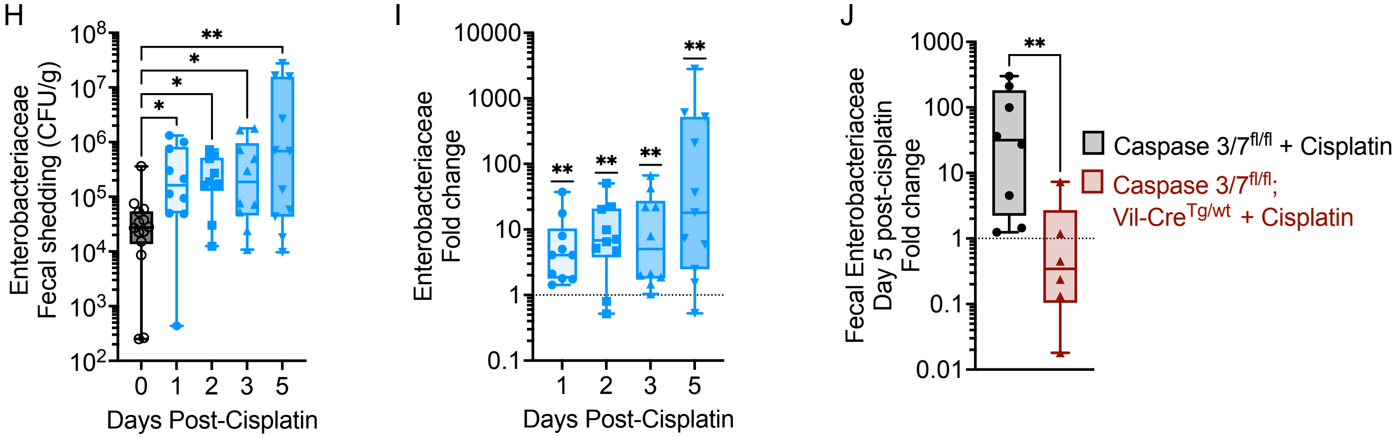

Figure 2. Epithelial cell apoptosis drives disease and dysbiosis

- **A.** TUNEL positive cells per colon tissue section area (mm^2) of indicated genotype and treatment at day 2 post treatment (n= 4 mice per group, averaged values of 10+ tissue sections per mouse shown, n=2 cohorts). Significance determined by one-way ANOVA with Tukey's multiple comparisons test.
- **B.** Weight loss of control Caspase 3/7$^{fl/fl}$ (n= 16) or Vil-Cre$^{+/-}$::Caspase 3/7$^{fl/lfl}$ (n= 12) mice following doxorubicin treatment. Daily weight measurements were normalized to the starting weight of each mouse to calculate % body weight. Significance determined by Mixed-effects model (REML). Mean + standard deviation is shown.
- **C.** Cecal weights (grams) of the indicated treatment and genotype at day 2 post-treatment (n= 6-11 per group). Significance determined by Kruskal-Wallis with Dunn's multiple comparisons test. Colon length (cm) of the indicated treatment and genotype at day 2 post-treatment (n= 8-12 per group). Significance determined by Kruskal-Wallis with Dunn's multiple comparisons test.
- **D.** Representative DAPI and UEA1 stained ileal tissue sections of the indicated treatment and genotype at day 2 post-doxorubicin treatment.
- **E.** UEA1 positive fluorescence as a percentage of ileum tissue area (n= 4 per group over 2 cohorts, averaged values of 10+ tissue sections per mouse shown) at day 2 post-doxorubicin.
- **F.** Mucosal thickness (μm) in the ileum of the indicated treatment and genotype at day 2 post-doxorubicin treatment (n= 4 per group over 2 cohorts, averaged values of 10+ tissue sections per mouse shown). Representative image and measurements from untreated mice shown.

For **E-F**: Significance determined by one-way ANOVA with Dunnett's multiple comparisons test.

- **G.** Enterobacteriaceae CFU per gram of fecal content from indicated genotypes at the indicated day post-doxorubicin treatment (n= 7-12 per genotype per time point, n=4 cohorts). Enterobacteriaceae fold change: Day 1 CFU in feces was normalized to the starting CFU for each mouse (n= 8-9 per genotype, n=3 cohorts).
- **H.** Enterobacteriaceae CFU per gram of fecal content from wildtype C57BL/6J mice at the indicated day post-cisplatin treatment (n= 10-14 per time point, n=3 cohorts). Significance determined by Kruskal-Wallis with Dunn's multiple comparisons test comparing each time point to control.
- **I.** Enterobacteriaceae fold change. CFU in feces at the indicated time post-cisplatin treatment was normalized to the starting CFU for each mouse (n= 10-11 per time point). Significance determined by Wilcoxon Signed Rank Test with a theoretical median of 1.
- **J.** Enterobacteriaceae fold change. Day 5 post-cisplatin CFU in feces was normalized to the starting CFU for each mouse (n= 6-8 per genotype, n=2 cohorts).

For **A-J**: ns $p > 0.05$, * $p \leq 0.05$, ** $p \leq 0.005$, *** $p \leq 0.0005$, **** $p \leq 0.0001$.

For **G, J**: Significance determined by Mann Whitney test.

For **A, C, E-J**: Box and whiskers show minimum to maximum values with all independent replicates, center denotes median, and the bounds denote the 25th to 75th percentiles.

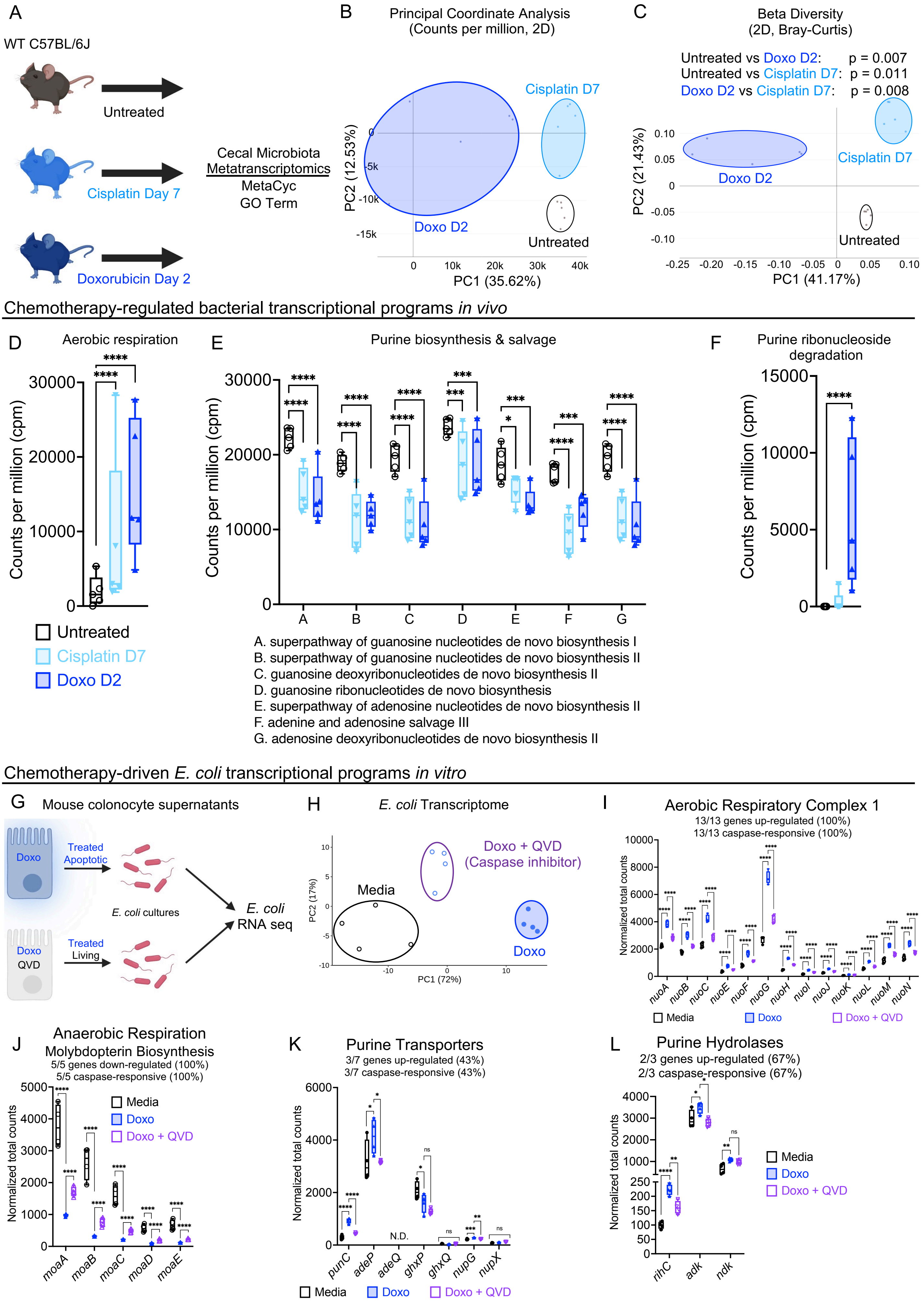
A
WT C57BL/6J
Untreated
Cisplatin Day 7
Doxorubicin Day 2
Cecal Microbiota
Metatranscriptomics
MetaCyc
GO Term
B
Principal Coordinate Analysis
(Counts per million, 2D)
Cisplatin D7
Doxo D2
Untreated
PC2 (12.53%)
PC1 (35.62%)
0
-5k
-10k
-15k
10k
20k
30k
40k
C
Beta Diversity
(2D, Bray-Curtis)
Untreated vs Doxo D2: p = 0.007
Untreated vs Cisplatin D7: p = 0.011
Doxo D2 vs Cisplatin D7: p = 0.008
Doxo D2
Cisplatin D7
Untreated
PC2 (21.43%)
PC1 (41.17%)
0.10
0.05
-0.05
-0.10
-0.25
-0.20
-0.15
-0.10
-0.05
0.05
0.10
Chemotherapy-regulated bacterial transcriptional programs in vivo
D
Aerobic respiration
Counts per million (cpm)
30000
20000
10000
0
****
****
☐ Untreated
☐ Cisplatin D7
☐ Doxo D2
E
Purine biosynthesis & salvage
Counts per million (cpm)
30000
20000
10000
0
A
B
C
D
E
F
G
****
***
*
A. superpathway of guanosine nucleotides de novo biosynthesis I
B. superpathway of guanosine nucleotides de novo biosynthesis II
C. guanosine deoxyribonucleotides de novo biosynthesis II
D. guanosine ribonucleotides de novo biosynthesis
E. superpathway of adenosine nucleotides de novo biosynthesis II
F. adenine and adenosine salvage III
G. adenosine deoxyribonucleotides de novo biosynthesis II
F
Purine ribonucleoside degradation
Counts per million (cpm)
15000
10000
5000
0
****
Chemotherapy-driven E. coli transcriptional programs in vitro
G
Mouse colonocyte supernatants
Doxo
Treated Apoptotic
Doxo QVD
Treated Living
E. coli cultures
E. coli RNA seq
H
E. coli Transcriptome
Doxo + QVD
(Caspase inhibitor)
Media
Doxo
PC2 (17%)
PC1 (72%)
10
5
0
-5
-10
I
Aerobic Respiratory Complex 1
13/13 genes up-regulated (100%)
13/13 caspase-responsive (100%)
Normalized total counts
10000
8000
6000
4000
2000
0
nuoA
nuoB
nuoC
nuoE
nuoF
nuoG
nuoH
nuoI
nuoJ
nuoK
nuoL
nuoM
nuoN
☐ Media
☐ Doxo
☐ Doxo + QVD
J
Anaerobic Respiration
Molybdopterin Biosynthesis
5/5 genes down-regulated (100%)
5/5 caspase-responsive (100%)
Normalized total counts
5000
4000
3000
2000
1000
0
moaA
moaB
moaC
moaD
moaE
☐ Media
☐ Doxo
☐ Doxo + QVD
K
Purine Transporters
3/7 genes up-regulated (43%)
3/7 caspase-responsive (43%)
Normalized total counts
6000
4000
2000
0
N.D.
ns
**
punC
adeP
adeQ
ghxP
ghxQ
nupG
nupX
☐ Media
☐ Doxo
☐ Doxo + QVD
L
Purine Hydrolases
2/3 genes up-regulated (67%)
2/3 caspase-responsive (67%)
Normalized total counts
4000
3000
2000
1000
250
200
150
100
50
0
rihC
adk
ndk
☐ Media
☐ Doxo
☐ Doxo + QVD

Figure 3. Bacterial transcriptional profile during dysbiosis

- **A.** Schematic of experimental groups for *in vivo* cecal microbiota transcriptional analyses.
- **B.** Principal Component Analysis (2D) of MetaCyc transcriptional pathways.
- **C.** Beta Diversity (2D) of MetaCyc transcriptional pathways. Indicated p values calculated by Bray-Curtis index.
- **D.** Total abundance (counts per million, cpm) of bacterial transcripts associated with aerobic respiration.
- **E.** Total abundance (counts per million, cpm) of bacterial transcripts associated with purine biosynthesis and salvage. The seven distinct MetaCyc pathways are indicated below.
- **F.** Total abundance (counts per million, cpm) of bacterial transcripts associated with purine ribonucleotide degradation.

For A-F, n= 5 per group.

For D-F: Statistical significance determined by 2way ANOVA with Dunnett's multiple comparisons test.

- **G.** Schematic of *in vitro* approach to trigger CT26 cell death using apoptosis with or without the pan caspase inhibitor (QVD).
- **H.** Principal Component Analysis (2D) of *E. coli* transcriptome.
- **I.** Normalized total transcript counts of the indicated genes belonging to aerobic respiratory complex 1 (*nuoA-N*).
- **J.** Normalized total transcript counts of the indicated genes belonging to molybdopterin biosynthesis (*moaA-E*).
- **K.** Normalized total transcript counts of the indicated purine transports.
- **L.** Normalized total transcript counts of the indicated purine hydrolases.

For A & G, created with BioRender.com

For G-L, n= 4 per group. Media conditions contain doxorubicin. Statistical significance from RNAseq determined by pairwise comparisons with corrections for false discovery rate (see methods).

For A-L: ns $p > 0.05$, * $p \leq 0.05$, ** $p \leq 0.005$, *** $p \leq 0.0005$, **** $p \leq 0.0001$.

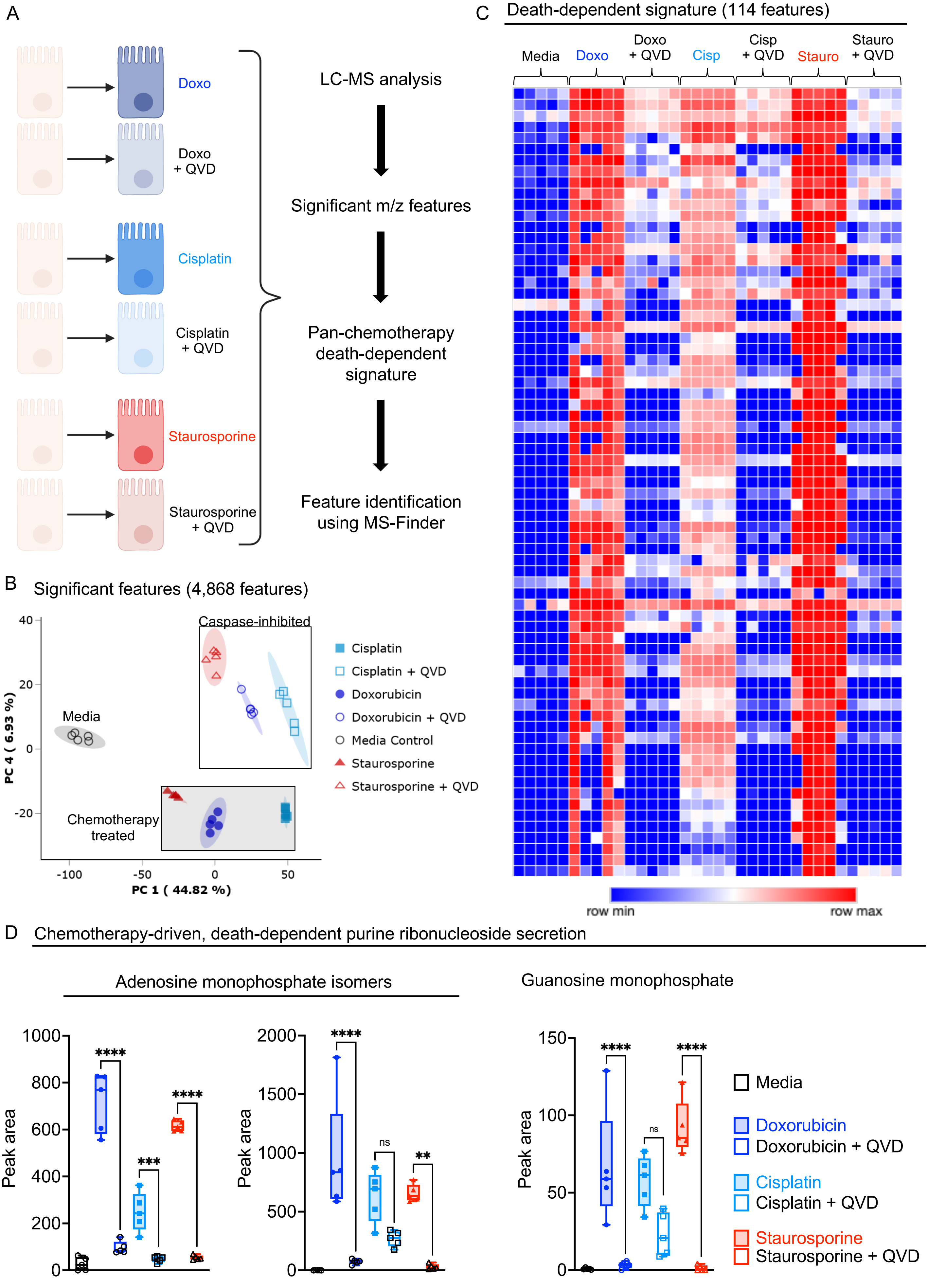

B Significant features (4,868 features)

C Death-dependent signature (114 features)

D Chemotherapy-driven, death-dependent purine ribonucleoside secretion

Adenosine monophosphate isomers

Guanosine monophosphate

Figure 4. Pan-chemotherapy, death-dependent metabolites

A. Schematic and work progression for *in vitro* metabolomics created with BioRender.com.

B. Principal Component Analysis of LC-MS m/z features that were statistically significant, as determined by ANOVA $p < 0.01$.

C. Heat map of 114 m/z features following hierarchical clustering performed on significant features in B.

D. Adenosine monophosphate (AMP) isomers, *m/z* 348.07 at 1.385 min. (left) and *m/z* 348.07 at 1.5515 min. (right), and guanosine monophosphate (GMP) *m/z* 364.07 at 1.5764 min. The identity of AMP and GMP was confirmed by matching the *m/z*, retention times, and MS/MS spectra with those of the respective reference standards. ns $p > 0.05$, ** $p \leq 0.005$, *** $p \leq 0.0005$, **** $p \leq 0.0001$. Box and whiskers show minimum to maximum values with all independent replicates, center denotes median, and the bounds denote the 25th to 75th percentiles.

For A-D, n= 5 per group.

Select apoptosis-dependent metabolites regulate *E. coli* transcription

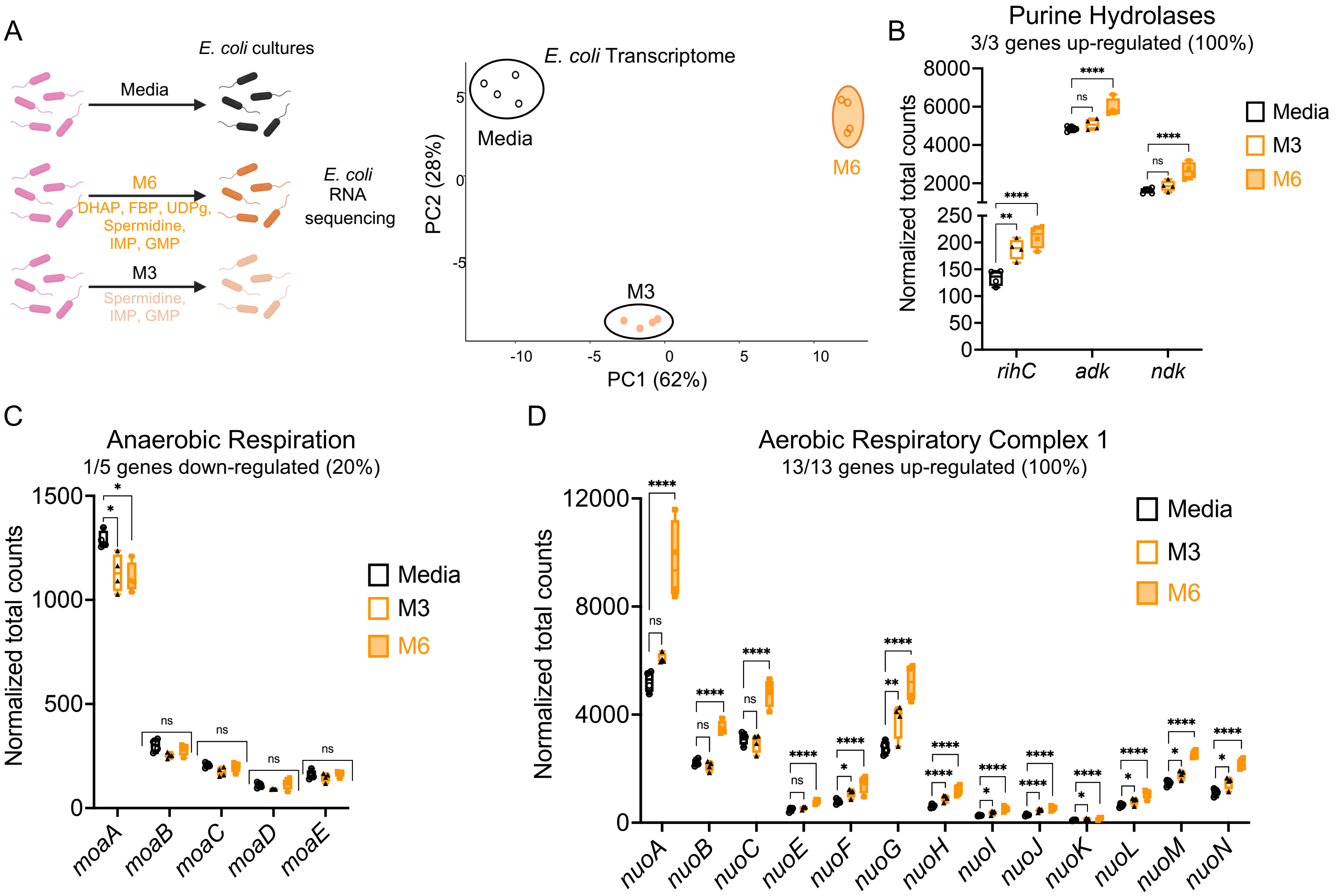

Model for Doxorubicin-induced *E. coli* fitness *in vivo*

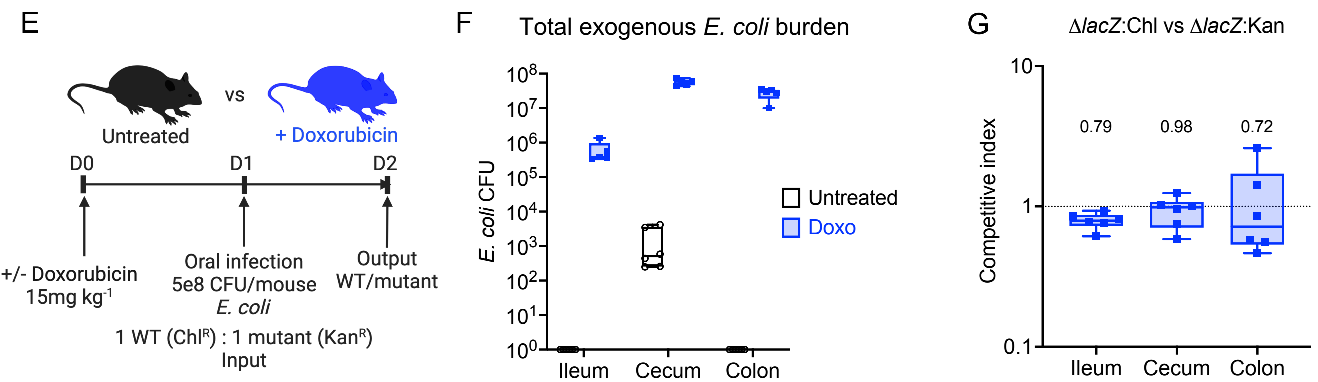

Doxorubicin reduces anaerobic respiration-dependent fitness

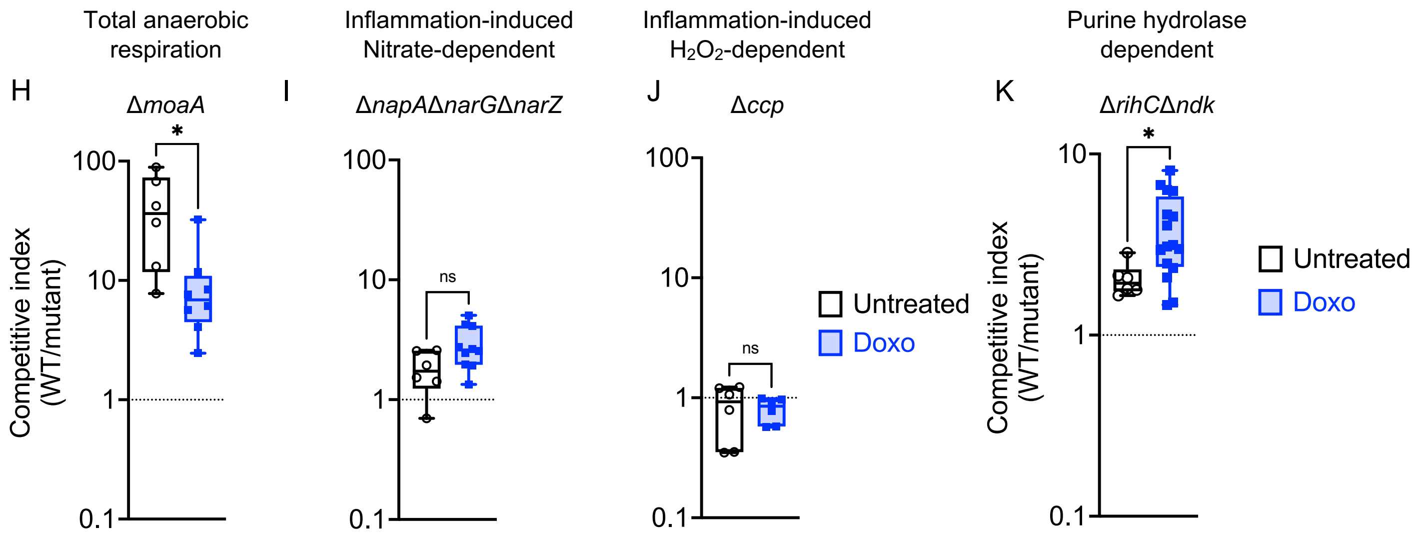

Figure 5. Death-dependent metabolites rewire *E. coli* transcriptome

A. Schematic of *in vitro* RNA sequencing approach (left). Principal Component Analysis (2D) of *E. coli* transcriptome (right).

B. Normalized total transcript counts of the indicated purine hydrolases.

C. Normalized total transcript counts of the indicated anaerobic respiration (molybdopterin biosynthesis) genes (*moaA-E*).

D. Normalized total transcript counts of the indicated genes belonging to aerobic respiratory complex 1 (*nuoA-N*).

For A-D, n= 4 per group. ns $p > 0.05$, * $p \leq 0.05$, ** $p \leq 0.005$, *** $p \leq 0.0005$, **** $p \leq 0.0001$. Statistical significance from RNAseq determined by pairwise comparisons with corrections for false discovery rate (see methods).

E. Schematic of *in vivo* bacterial fitness model.

F. Exogenous *E. coli* CFU in the indicated intestinal tissue compartment with or without doxorubicin pretreatment. n=4-6 mice per group, n=2 cohorts.

G. Competitive index of wildtype *E. coli* with either Chl (SR007) or Kan (SR009) antibiotic resistance cassette inserted into the *lacZ* locus. n=6 mice.

H. Competitive index of wildtype (SR007) vs Δ*moaA* (PC052). n=6-8 mice per group, n=2 cohorts.

I. Competitive index of wildtype (SR007) vs Δ*napA*Δ*narG*Δ*narZ* (PC038). n=6-10 mice per group, n=3 cohorts.

J. Competitive index of wildtype (SR007) vs Δ*ccp* (PC042). n=6 mice per group, n=2 cohorts.

K. Competitive index of wildtype (SR007) vs Δ*rihC*Δ*ndk* (PC035). n=6-16 mice per group, n=3 cohorts.

For A & E, created with BioRender.com

For H-K, ns $p > 0.05$, * $p \leq 0.05$. Statistical significance determined by Mann Whitney test.

For B-D, F-K: Box and whiskers show minimum to maximum values with all independent replicates, center denotes median, and the bounds denote the 25th to 75th percentiles.

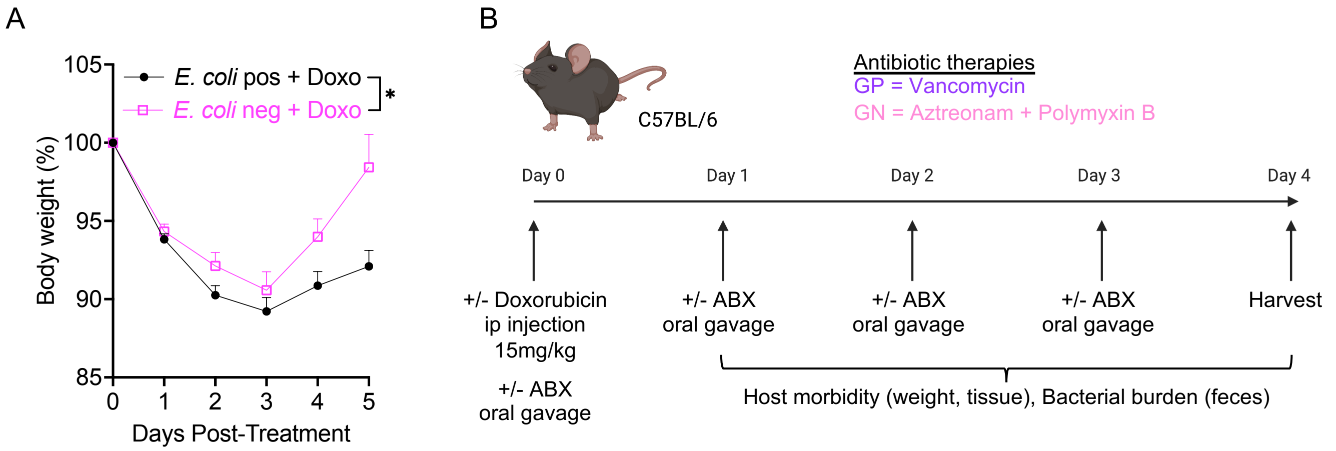

Gram-negative targeting antibiotic therapy restricts Enterobacteriaceae bloom

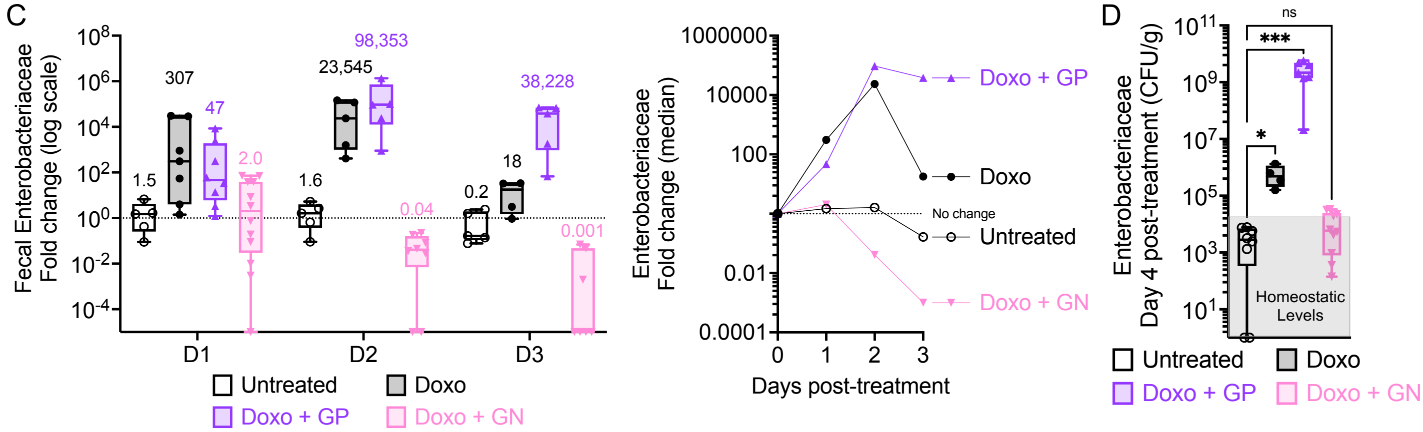

Gram-negative targeting antibiotic therapy improves recovery from chemotherapy

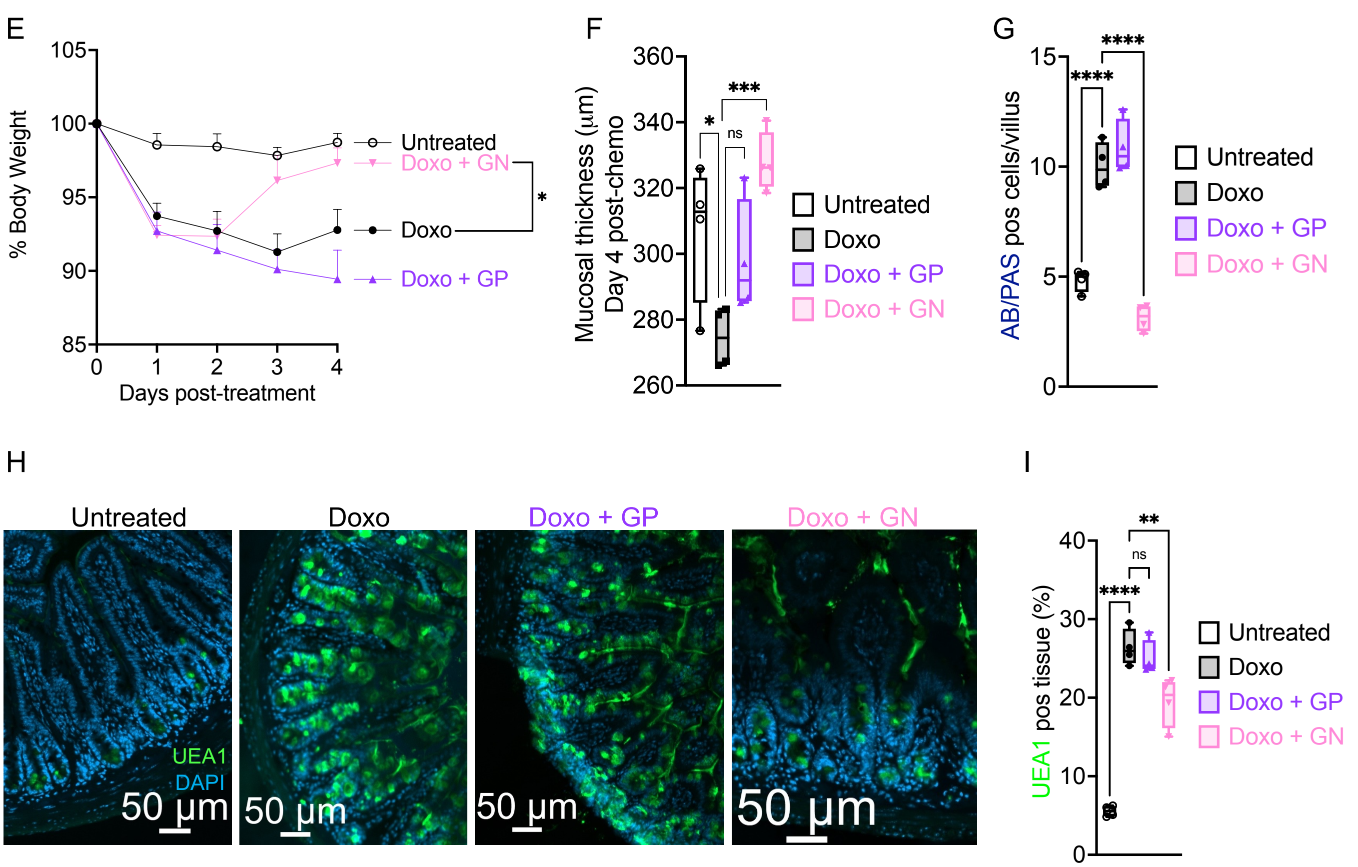

Figure 6. Targeted antibiotic intervention improves disease

- **A.** Weight loss of *E. coli* positive (n= 8) or *E. coli* negative (n= 10) wildtype mice following doxorubicin treatment. Weight measurements were normalized to the starting weight of each mouse to calculate % body weight. *E. coli* colonization status was determined by CFU in feces daily. Significance determined by Mixed-effects model (REML). Mean + standard deviation is shown.
- **B.** Schematic of *in vivo* doxorubicin and antibiotic treatment regimen created with BioRender.com. The first dose of antibiotics was orally administered immediately after IP injection of doxorubicin.
- **C.** Enterobacteriaceae fold change. CFU in feces at the indicated times were normalized to the starting CFU for each mouse (n= 6-12 per time per treatment, n=3 cohorts). The median fold change for each treatment group is listed above each group (left) and plotted over time (right).
- **D.** Tissue-associated Enterobacteriaceae levels within the cecum at day 4 post-doxorubicin treatment. CFU per gram of tissue weight (n= 4-10 per treatment group, n=2 cohorts). Significance determined by Kruskal-Wallis with Dunn's multiple comparisons test comparing each treatment group to untreated controls.
- **E.** Weight loss of wildtype mice with the indicated antibiotic therapy following doxorubicin treatment (n= 6-14 per group, n=3 cohorts). Daily weight measurements were normalized to the starting weight of each mouse to calculate % body weight. Significance determined by 2way ANOVA with Dunnett's multiple comparisons test. Mean + standard deviation is shown.
- **F.** Mucosal thickness (μm) in the ileum of the indicated treatment at day 4 post-doxorubicin treatment (n= 4 mice per group, averaged values of 10+ tissue sections per mouse shown, n=2 cohorts).
- **G.** Number of Alcian Blue positive cells per villus in the ilea of the indicated treatment groups at day 4 post-doxorubicin treatment (n= 4 mice per group, averaged values of 10+ tissue sections per mouse shown, n=2 cohorts).
- **H.** Representative DAPI and UEA1 stained ileal tissue sections of the indicated treatment groups at day 4 post-doxorubicin treatment.
- **I.** UEA1 positive fluorescence as a percentage of ileum tissue area (n= 4 mice per group, averaged values of 10+ tissue sections per mouse shown, n=2 cohorts) at day 4 post-doxorubicin.

For A-I, ns $p > 0.05$, * $p \leq 0.05$, ** $p \leq 0.005$, *** $p \leq 0.0005$, **** $p \leq 0.0001$.

For C, D, F, G, I: Box and whiskers show minimum to maximum values with all independent replicates, center denotes median, and the bounds denote the 25th to 75th percentiles.

For F, G, I: Significance determined by one-way ANOVA with Tukey's multiple comparisons test.

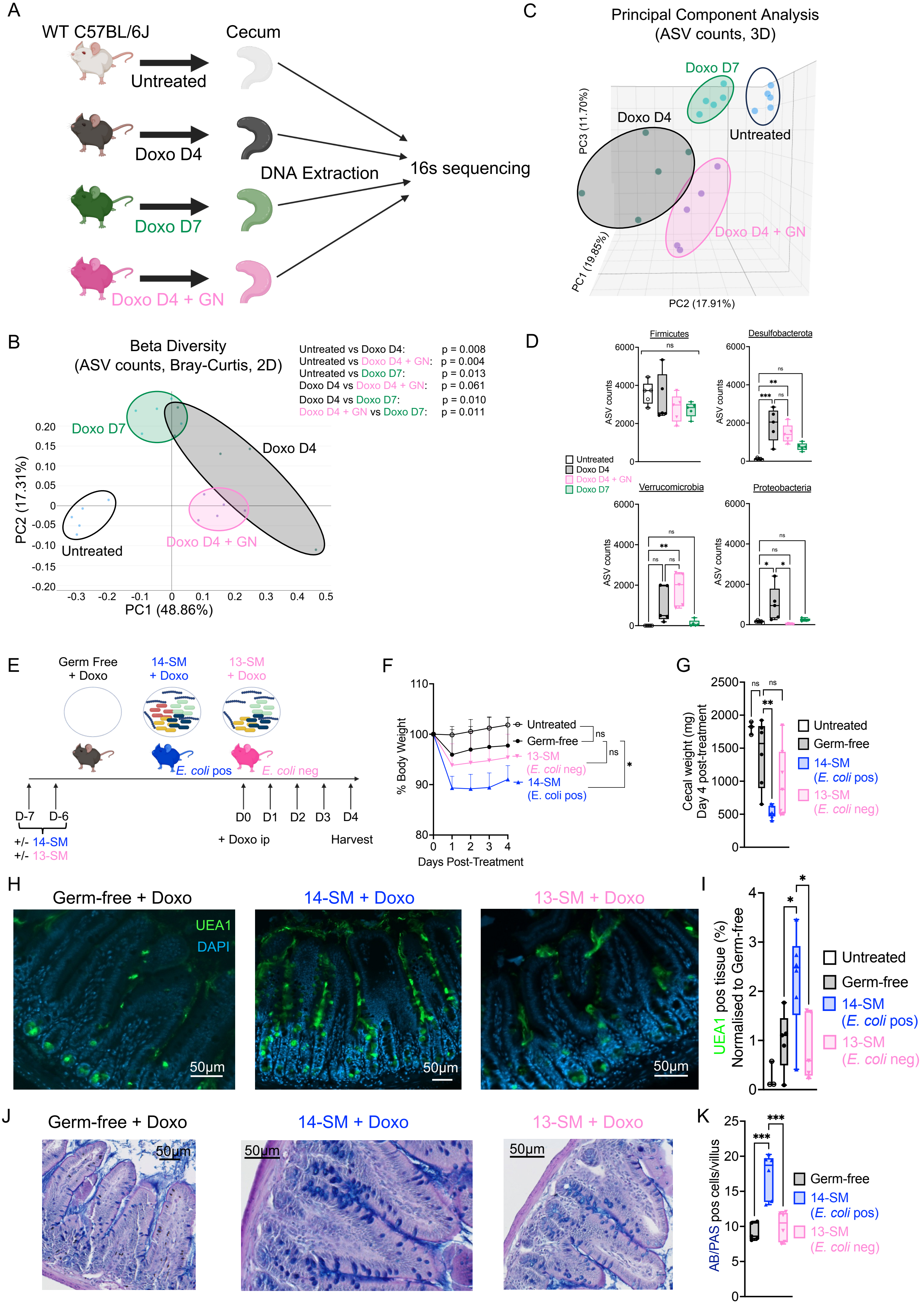
A
WT C57BL/6J
Cecum
Untreated
Doxo D4
Doxo D7
Doxo D4 + GN
DNA Extraction
16s sequencing
B
Beta Diversity
(ASV counts, Bray-Curtis, 2D)
Untreated vs Doxo D4: p = 0.008
Untreated vs Doxo D4 + GN: p = 0.004
Untreated vs Doxo D7: p = 0.013
Doxo D4 vs Doxo D4 + GN: p = 0.061
Doxo D4 vs Doxo D7: p = 0.010
Doxo D4 + GN vs Doxo D7: p = 0.011
PC2 (17.31%)
PC1 (48.86%)
Doxo D7
Doxo D4
Untreated
Doxo D4 + GN
C
Principal Component Analysis
(ASV counts, 3D)
PC3 (11.70%)
PC1 (19.85%)
PC2 (17.91%)
Doxo D7
Doxo D4
Untreated
Doxo D4 + GN
D
Firmicutes
Desulfobacterota
Verrucomicrobia
Proteobacteria
ASV counts
ns
**
***
*
Untreated
Doxo D4
Doxo D4 + GN
Doxo D7
E
Germ Free + Doxo
14-SM + Doxo
13-SM + Doxo
E. coli pos
E. coli neg
D-7
D-6
D0
D1
D2
D3
D4
+/- 14-SM
+/- 13-SM
+ Doxo ip
Harvest
F
% Body Weight
Days Post-Treatment
Untreated
Germ-free
13-SM (E. coli neg)
14-SM (E. coli pos)
ns
*
G
Cecal weight (mg) Day 4 post-treatment
Untreated
Germ-free
14-SM (E. coli pos)
13-SM (E. coli neg)
ns
**
H
Germ-free + Doxo
14-SM + Doxo
13-SM + Doxo
UEA1
DAPI
50µm
I
UEA1 pos tissue (%) Normalised to Germ-free
Untreated
Germ-free
14-SM (E. coli pos)
13-SM (E. coli neg)
*
J
Germ-free + Doxo
14-SM + Doxo
13-SM + Doxo
50µm
K
AB/PAS pos cells/villus
Germ-free
14-SM (E. coli pos)
13-SM (E. coli neg)
***

Figure 7. Enterobacteriaceae bloom delays intestinal recovery

A. Schematic of *in vivo* 16s rRNA sequencing of mouse cecal microbiome

B. Beta Diversity (2D) of ASV counts. Indicated p values calculated by Bray-Curtis index.

C. Principal Component Analysis (2D) of amplicon sequence variant (ASV) counts.

D. Total ASV counts of the indicated bacterial Phyla within the indicated treatment conditions. Significance determined by one-way ANOVA with Tukey's multiple comparisons test. Firmicutes (Bacillota), Proteobacteria (Pseudomonadota).

For A-C, n= 5 per group.

E. Schematic for *in vivo* re-colonization of germ-free mice with a 14-member microbiota (14-SM, *E. coli* positive) or 13-member microbiota (13-SM, *E. coli* negative) followed by doxorubicin treatment.

F. Weight loss of untreated germ-free ("untreated" n= 5), germ-free + doxorubicin ("germ-free" n= 8), 14-SM *E. coli* positive + doxorubicin ("14-SM" n= 7) or 13-SM *E. coli* negative + doxorubicin ("13-SM" n= 7). Daily weight measurements were normalized to the starting (day 0) weight of each mouse to calculate % body weight. n=3 cohorts. Significance determined by 2way ANOVA with Dunnett's multiple comparisons test. Mean + standard deviation is shown.

G. Cecal weight (μg) of untreated germ-free ("untreated" n= 3), germ-free + doxorubicin ("germ-free" n= 6), 14-SM *E. coli* positive + doxorubicin ("14-SM" n= 7) or 13-SM *E. coli* negative + doxorubicin ("13-SM" n= 7). n=3 cohorts.

H. Representative DAPI and UEA1 stained ileal tissue sections of the indicated treatment groups at day 4 post-doxorubicin treatment.

I. UEA1 positive fluorescence as a percentage of ileum tissue area (n= 3-6 mice per group, averaged values of 5-10 tissue sections per mouse shown, n= 2 cohorts) at day 4 post-doxorubicin.

J. Representative Alcian Blue-PAS stained ileal tissue sections of the indicated treatment groups at day 4 post-doxorubicin treatment.

K. Number of Alcian Blue positive cells per villus in the ilea of the indicated treatment groups at day 4 post-doxorubicin treatment (n= 5-6 mice per group, averaged values of 5-10 tissue sections per mouse shown, n= 2 cohorts).

For A-K, ns $p > 0.05$, * $p \leq 0.05$, ** $p \leq 0.005$, *** $p \leq 0.0005$, **** $p \leq 0.0001$.

For A & E, created with BioRender.com

For D, G, I, K: Box and whiskers show minimum to maximum values with all independent replicates, center denotes median, and the bounds denote the 25th to 75th percentiles.

For G, I, K: Significance determined by one-way ANOVA with Dunnett's multiple comparisons test.

STAR METHODS

RESOURCE AVAILABILITY

Lead contact

Further information and requests for resources and reagents should be directed to and will be fulfilled by the lead contact Kodi S. Ravichandran (kodi@wustl.edu).

Materials availability

Unique materials generated that support the findings of this study are available from the lead contact upon request.

Data Availability

Bacterial RNA-seq data have been submitted to the Gene Expression Omnibus (GEO) under accession number GSE244920. Bacterial 16s rRNA-seq data have been submitted to Sequence Read Archive (SRA) under accession number Bioproject PRJNA1018413 (SRA accessions SRR26122319 -SRR26122338). The bacterial metatranscriptomics data have been submitted to SRA under accession number Bioproject PRJNA1020783 (SRA accessions SRR26195156-SRR26195170).

This paper does not report original code.

Any additional information required to reanalyze the data reported in this paper is available from the lead contact upon request.

EXPERIMENTAL MODEL AND STUDY PARTICIPANT DETAILS

Animal studies:

All animal work was approved by the VIB-UGent Center for Inflammation Research Ethical Committee, and the University of Ghent Animal Ethics Committee.

Wild-type C57BL/6J mice were purchased from Janvier Labs or were bred in-house. For all mutant mouse genotypes, fl/fl Cre-negative mice served as littermate controls where appropriate. Vil-cre$^{Tg/wt}$ mice were co-housed with Vil-cre$^{wt/wt}$ controls during development and genotypes were only separated at the beginning of each experiment. *Vil-Cre*$^{Tg/wt}$::*Caspase 3/7*$^{fl/fl}$ mice were generated as described[34]. Germ-free and gnotobiotic experiments were performed in the germ-free facility at the University of Ghent. All mice were 7–14 weeks of age at the time of experimentation, and both male and female mice were used in equal proportions across treatment and control groups. For all experiments, a minimum of 2 independent cohorts were used to ensure reproducibility and an equal mix of male and female mice were used throughout the study.

Bacterial cultures

All bacterial strains are listed in the key resources table. Overnight cultures of *E. coli* strain HS[73] were routinely grown at 37 °C with 200 rpm agitation (aerobic) in LB broth. After overnight culture (approximately 16 h), 1 ml of bacterial culture was pelleted and media removed. Cultures were re-suspended in 1× PBS.

Mammalian cell line culture

All cell lines are listed in the key resources table. CT26 murine colonocytes and HCT116 human colonocytes were routinely cultured in DMEM + 10% FBS. For the induction of cell death, cells were seeded at 4×10^5 cells per ml in 12-well plates. Cells were washed with 1× PBS before the induction of cell death. To induce cell death, cells were treated with either 1μM Staurosporine, 20μg/ml of doxorubicin, or 50μM cisplatin. To inhibit caspase activation, indicated cells were treated with 30μM QVD for 1 hour prior to drug treatment, and fresh QVD was added along with cytotoxic drug. After 24 hours of treatment, supernatant was collected and spun at 330g for 5 min to remove cellular debris. The resulting supernatant was filtered using a 0.2-µm syringe filter and either used immediately or frozen at −80 degrees C for later use. To quantify cell death, cells were stained with annexin V (AV) conjugated to APC for 15 min at room temperature in annexin V binding buffer (BD). Flow cytometry was performed using the FACS Calibur (BD). Data were analysed using FlowJo v.10 software. All independent experiment values shown are the average values of technical duplicates.

METHOD DETAILS

Doxorubicin treatment: Doxorubicin was given as a single intraperitoneal injection at 15 mg kg-1 of mouse body weight while vehicle control (water) was given at similar volumes (approximately 300 µl volumes of water or 1 mg ml−1 doxorubicin solution). Mice were weighed daily, including prior to receiving treatment, and fresh fecal samples were taken at indicated times. Tissues were collected at indicated times after treatment. For bacterial burden measurements and TUNEL staining, luminal contents of the ileum (the last 5–6 cm of the distal end of the small intestine) and the colon were removed. Luminal content was retained in all caecal samples and in samples used for UEA1 staining. For bacterial burden, RNA, and DNA extraction intestinal tissue was homogenized in 1 ml of 1× PBS. Total Enterobacteriaceae burden, including E. coli, was assessed by plating tissue lysates on MacConkey agar without antibiotics. Relative fold-changes were calculated for each mouse by dividing each mouse's Enterobacteriaceae levels at a given time by the starting population taken from the same mouse at day 0, prior to treatment. Endogenous Enterobacteriaceae were identified as genus *Escherichia* (probable *E. coli* or *E. albertii*) following 16s rRNA sequencing on purified genomic

DNA. In addition, *E. coli* identification was confirmed via MALDI–TOF mass spectrometry (Bruker) performed on colonies from MacConkey agar plates. For antibiotic therapy experiments, mice were given daily oral gavage of the indicated antibiotic, or volume-matched vehicle (water) control, starting after doxorubicin injection. Mice were given vancomycin (500μg/ml) or a combination of aztreonam (100μg/ml) and polymyxin B (100μg/ml) via oral gavage in 100μl doses[74,75].

Cisplatin treatment: Cisplatin was given as a single intraperitoneal injection at 10mg kg-1 of mouse body weight while vehicle control (0.9% NaCl) was given at similar volumes. Mice were weighed daily, including prior to receiving treatment, and fresh fecal samples and tissue samples were taken at indicated times. Bacterial burden measurements were calculated as described above.

Germ-free and gnotobiotic mice: Germ-free mice were re-colonized with synthetic microbiota cocktails as previously described[64]. The 14-member synthetic cocktail, including *E. coli*, or the 13-member synthetic cocktail, excluding *E. coli*, were cultured and verified in the inoculum prior to gavage as described[76]. Mice received oral gavage of the indicated cocktail on consecutive days, rested for 1 week, and then were treated with doxorubicin as described above.

Microscopy

Alcian blue-Period Acid Schiff (AB-PAS): Ileal and colonic tissues were dissected, flushed of their lumenal content with PBS, fixed in 10% formalin, embedded in paraffin, and sectioned at 5 µm. Dewaxed slides were incubated in 1% Alcian blue for 20 min. Sections were subsequently washed with water and incubated with 1% periodic acid for 15 min followed by Schiff's reagent for 10 min. Sections were counterstained with Mayer's hematoxylin for 30 s before washing, dehydration, and mounting with Entellan (Merck). Sections were imaged on a Zeiss AxioScan Digital Slide Scanner. In the ileum, the number of AB-PAS positive cells located within the villi were counted across a minimum of 5 villi per tissue section, a minimum of 4 tissue sections per mouse, and a minimum of 3 independent mice per cohort. Broken villi were excluded from analysis.

TUNEL staining: Lumenal content was flushed from ileal and colonic tissues and samples were fixed, embedded, and sectioned as above. The TUNEL assay was performed according to manufacturer's instructions (In situ cell death detection kit, TMR red, Roche) and followed by an overnight incubation at 4 degrees C with DAPI.

Cleaved caspase 3: Staining for activated apoptosis was performed as described[33]. Slides were deparaffinized, rehydrated with an alcohol series and processed for antigen retrieval with Dako citrate buffer for 25 min in a pressure cooker. Endogenous peroxidase activity was blocked using Dako REAL Peroxidase-Blocking Solution for 20 min, followed by three washes in PBS (5 min each). Sections were blocked for 30 min in Dako REAL Antibody Diluent supplemented with 5% goat serum. Incubation with cleaved caspase-3 antibody (1:1,500) was carried out overnight at 4 degrees C in blocking buffer. Sections were washed three times with PBS (5 min each) and incubated with SignalStain Boost IHC Detection Reagent for 30 min. Signal was developed using ImmPACT DAB Substrate followed by haematoxylin counterstaining, dehydration and mounting with Entellan new.

CD45 staining: For CD45 staining, tissues were fixed overnight in 4% neutral buffered formalin, embedded in paraffin and cut into 5-µm sections. Slides were processed as above (cleaved caspase 3) and incubated overnight at 4 °C with a rabbit CD45 antibody. Sections were washed three times with PBS (5 min each) and incubated with SignalStain Boost IHC Detection Reagent for 30 min. Signal was developed using ImmPACT DAB Substrate followed by haematoxylin counterstaining, dehydration and mounting with Entellan new.

Image acquisition: Slides were imaged with an Axio Scan.Z1 (Zeiss), using a 10× Plan-Apochromat 0.45 NA (0.650 µm pixel−1) and a Hamamatsu Orca Flash camera. With an HXP illumination source, the following were used in the acquisition: DAPI (BP 445/50), HE GFP (BP 525/50), HE DsRed (BP 605/70) and Cy5 (BP 690/50). Image analysis was performed using QuPath (version 0.1.2).

16s rRNA sequencing

Sample acquisition: Mouse cecal samples were isolated at the indicated times post the indicated treatments. Ceca were homogenized in 1ml 1x PBS on ice and then cell debris was aggregated by spinning samples down at 1000rpm for 5 minutes at 4 degrees C. The resulting supernatant was collected, transferred to a fresh Eppendorf tube, and then cells were pelleted by centrifugation at 13,000rpm for 10 minutes at 4 degrees C. DNA was extracted using the PureLink™ Microbiome DNA Purification Kit according to the manufacturer's instructions.

Sequencing: DNA samples were quantified using Qubit 4 fluorometer and QubitTM dsDNA HS Assay Kit (Thermofisher Scientific). 16S amplicon sequencing starts with 5ng of isolated genomic DNA. Libraries are constructed by amplification via PCR with primers covering the V3-V4 region (341F & 805R). Sequencing was performed on Illumina Miseq platform 2x250bp.

Analysis: The CosmosID-HUB Microbiome's 16S workflow implements the DADA2 algorithm[77,78] as its core engine and utilizes the Nextflow ampliseq pipeline[79] definitions to run it on a cloud infrastructure. Briefly, primer removal is done with Cutadapt[80], and quality trimming parameters are passed to DADA2 to ensure that the median quality score over the length of the read exceeds a certain Phred score threshold. Within DADA2, forward and reverse reads are each trimmed to a uniform length based on the quality of reads in the sample—higher quality data will generally result in longer reads. DADA2 uses machine learning with a parametric error model to learn the error rates for the forward and reverse reads, based on the premise that correct sequences should be more common than any particular error-variant. DADA2 then applies its core sample inference algorithm to the filtered and trimmed data, applying these learned error models. Paired-end reads are then merged if they have at least 12 bases of overlap and are identical across the entire overlap. The resulting table of sequences and observed frequencies is filtered to remove chimeric sequences (those that exactly match a combination of more-prevalent "parent" sequences). Taxonomy and species-level identification (where possible) are conducted with DADA2's naive Bayesian classifier, using the Silva version 138 database. Lastly, the predicted functional potential of the community was profiled using PICRUST2[81-85]. Briefly, PICRUSt2 (Phylogenetic Investigation of Communities by Reconstruction of Unobserved States) is a tool that predicts functional capabilities and abundances of a microbial community based on the observed amplicon (marker gene) content. Functional capabilities are given by EC classifiers, or MetaCyc ontologies, and these can be aggregated to predict pathways that are likely present in a given sample.

Metatranscriptomics

Sample acquisition: Mouse cecal samples were isolated at the indicated times post the indicated treatments. Ceca were homogenized in 1ml 1x PBS on ice and then cell debris was aggregated by spinning samples down at 1000rpm for 5 minutes at 4 degrees C. The resulting supernatant was collected, transferred to a fresh Eppendorf tube, and then cells were pelleted by centrifugation at 13,000rpm for 10 minutes at 4 degrees C. Cell pellets were resuspended in TriZol and RNA was extracted and DNA removed using the RiboPure RNA Purification Kit according to the manufacturer's instructions.

Sequencing: RNA sample quality was assessed by High Sensitivity RNA Tapestation (Agilent Technologies Inc., California, USA) and quantified by Qubit 2.0 RNA HS assay (ThermoFisher, Massachusetts, USA). Ribosomal RNA was depleted with Ribo-Zero Plus rRNA Removal Kit (Illumina Inc., California, USA). Samples were then randomly primed and fragmented based on manufacturer's recommendation. The first strand is synthesized with the Protoscript II Reverse Transcriptase with a longer extension period, approximately 30 minutes at 42C. All remaining steps for library construction were used according to the NEBNext® UltraTM II Non-Directional RNA Library Prep Kit for Illumina® (New England BioLabs Inc., Massachusetts, USA). Final libraries quantity was assessed by Qubit 2.0 (ThermoFisher, Massachusetts, USA) and quality was assessed by TapeStation HSD1000 ScreenTape (Agilent Technologies Inc., California, USA). Final library size was about 300bp with an insert size of about 150bp. Illumina® 8-nt unique dual-indices were used. Equimolar pooling of libraries was performed based on QC values and sequenced on an Illumina® NovaSeq S4 (Illumina, California, USA) with a read length configuration of 150 PE for 20M PE reads per sample (10M in each direction).

Analysis: The system utilizes a high-performance data-mining k-mer algorithm that rapidly disambiguates millions of short sequence reads into the discrete genomes engendering the particular sequences. The pipeline has two separable comparators: the first consists of a pre-computation phase for reference databases and the second is a per-sample computation. The input to the pre-computation phase are databases of reference genomes, virulence markers and antimicrobial resistance markers that are continuously curated by CosmosID scientists. The output of the pre-computational phase is a phylogeny tree of microbes, together with sets of variable length k-mer fingerprints (biomarkers) uniquely associated with distinct branches and leaves of the tree. The second per-sample computational phase searches the hundreds of millions of short sequence reads, or alternatively contigs from draft de novo assemblies, against the fingerprint sets. This query enables the sensitive yet highly precise detection and taxonomic classification of microbial NGS reads. The resulting statistics are analyzed to return the fine-grain taxonomic and relative abundance estimates for the microbial NGS datasets. To exclude false positive identifications the results are filtered using a filtering threshold derived based on internal statistical scores that are determined by analyzing a large number of diverse metagenomes. The same approach is applied to enable the sensitive and accurate detection of genetic markers for virulence and for resistance to antibiotics. Initial QC, adapter trimming and preprocessing of metagenomic sequencing reads are done using BBduk. The quality controlled reads are then subjected to a translated search against a comprehensive and non-redundant protein sequence database, UniRef 90. The UniRef90 database, provided by UniProt, represents a clustering of all non-redundant protein sequences in UniProt, such that each sequence in a cluster aligns with 90% identity and 80% coverage of the longest sequence in the cluster. The mapping of metagenomic reads to gene sequences are weighted by mapping quality, coverage and gene sequence length to estimate community wide weighted gene family abundances as described by Franzosa et al[42]. Gene families are then annotated to MetaCyc[86] reactions (Metabolic Enzymes) to reconstruct and quantify MetaCyc[86] metabolic pathways in the community as described by Franzosa et al[42]. Furthermore, the UniRef_90 gene families are also regrouped to Enzyme Commission Enzymes, Pfam protein domains, CAZy enzymes and GO Terms in order to get an exhaustive overview of gene functions in the community. Lastly, to facilitate comparisons across multiple samples with different sequencing depths, the abundance values are normalized using Total- sum scaling (TSS) normalization to produce "Copies per million" (analogous to TPMs in RNA- Seq) units.

Intestinal epithelial cell isolation

Mice were euthanized at the indicated times post-doxorubicin treatment. Ileum(10cm) and colon were collected, excess lymphatic tissue was removed, and tissues were stored in cold PBS temporarily. Lumenal content was flushed from ileum and colon with cold PBS. Intestinal tissues were cut longitudinally and excess lumenal content was flushed with additional cold PBS. Intestinal tissues were cut into approximately 0.5cm sections and placed into 50ml conical tubes containing 10ml pre-warmed dissociation buffer (5mM EDTA, 10uM Y-27632, 1mM DTT, 10mM HEPES, Pen/Strep in PBS). Tissues were incubated in 37 degrees C water bath for 15 minutes, turning the tubes upside down 3 times every 5 minutes. Media was passed through a 1000um strainer to remove dissociation buffer, and tissue was transferred to a fresh 50ml conical tube containing 40mL cold PBS. Samples were vortexed for 30 seconds at max speed. Undigested tissue was removed by passing through a 1000um strainer and cells were collected by centrifugation for 500g for 10 minutes at 4 degrees C. The cell pellet was washed 1x with 30ml cold PBS, vortexed for 10 seconds at max speed, and filtered through 70um strainer to remove remaining tissues. Samples were spun down at 4 degrees C, 500g for 10 minutes to obtain pellet and resuspended in cold PBS until cells were lysed for Western blot analyses.

LC-MS

CT26 cells were cultured in DMEM + 10% FBS in phenol red free media. Cell death was induced and cell-free supernatants collected as described above. 1800 μl of methanol was added to 200 μl of supernatant/medium. The samples were vortexed and left at room temperature for 1 hour followed by centrifugation for 5 min at 14,000 rpm. 1000 μl of the methanol extract was transferred to a new Eppendorf and evaporated to dryness under vacuum conditions. The dried methanol extracts were resolubilized in 100 μl cyclohexane and 100 μl milli-Q water and the aqueous phase was analyzed on Ultra Performance Liquid Chromatography High Resolution Mass Spectrometry (UHPLC-HRMS) in positive and negative ionization mode at the VIB Metabolomics Core Ghent. 10 μl was injected on a Waters

Acquity UHPLC device connected to a Vion HDMS Q-TOF mass spectrometer (Waters, Manchester, UK). Chromatographic separation was carried out on an ACQUITY UPLC BEH C18 (150 × 2.1 mm, 1.7 µm) column (Waters, USA), column temperature was maintained at 40 degrees C. A gradient of two buffers was used for separation: buffer A (99:1:0.1 water:acetonitrile:formic acid, pH 3) and buffer B (99:1:0.1 acetonitrile:water:formic acid, pH 3), as follows: 99% A for 0 min decreased to 50% A in 30 min, decreased to 30% from 30 to 35 minutes, and decreased to 0% from 35 to 37 minutes. The flow rate was set to 0.35 mL min−1. Electrospray Ionization (ESI) was applied, LockSpray ion source was operated in negative and positive ionization mode under the following specific conditions: capillary voltage, 2.5 kV (ESI-) and 1 kV (ESI+); source temperature, 120 degrees C; desolvation gas temperature, 550 degrees C; desolvation gas flow, 800 L h−1; and cone gas flow, 50 L h−1. The collision energy for full MS scan was set at 6 eV for low energy settings, for high energy settings (MSe) it was ramped from 20 to 70 eV. For DDA-MS/MS the low mass ramp was ramped between 6-20 uV, and the high mass ramp was ramped between 20-70 eV. Mass range was set from 50 to 1500 Da, scan time was set at 0.1s. Nitrogen (greater than 99.5%) was employed as desolvation and cone gas. Leucine-enkephalin (100 pg µL−1 solubilized in water:acetonitrile 1:1 [v/v], with 0.1% formic acid) was used for the lock mass calibration, with scanning every 2 min at a scan time of 0.1 s. Profile data was recorded through Unifi Workstation v2.0 (Waters). Data processing was performed with Progenesis QI software version 3.0 (Waters) for chromatogram alignment and compound ion detection. The detection limit was set at medium sensitivity with a minimum peak width of 0.04 min. In ESI- and ESI+ ionization, 5207 and 7979 features were detected respectively and aligned to "PooledSample_03", each feature having an m/z and a retention time.

The following filters were applied to analyze the data: average ion intensity ≥ 0.01% of the most intense feature (resulting in 9,985 features) and ANOVA p-value < 0.01 (resulting in 4,868 features). Statistical analyses were performed on ArcSinh-transformed and pareto scaled ion intensities. The metabolic profiles of the significant ANOVA features were clustered using hierarchical cluster analysis (Euclidian distance, average linkage method) resulting in 114 features with the profile of interest. Structural annotation of these features was attempted using MS-FINDER (in silico fragmentation)[87]. The following parameter settings were applied: Spectral database search against Massbank[88], GNPS[89],and ReSpect[90] cut off for spectral match: 80%, formula prediction and structural elucidation by in silico fragmenter using all available local databases, cut off for structural elucidation: 5, MS1 mass tolerance: 10 ppm, MS2 mass tolerance: 50 ppm, relative abundance cut off: 0.1%, LEWIS and SENIOR check: TRUE, element ration check: common range (99.7%), element selection: C, H, N, O, P, S, tree depth: 2. Structural identification of AMP and GMP was performed by comparison of the retention time and mass spectrum of an AMP and GMP reference standard (Sigma-Aldrich).

Bacterial culture

The metabolite mixture 'M6' was composed of spermidine, fructose-1,6-bisphosphate (FBP), dihydroxyacetone phosphate (DHAP), guanosine monophosphate (GMP), inosine monophosphate (IMP) and UDP-glucose while 'M3' was composed of spermidine, GMP, and IMP[53]. *E. coli* was grown aerobically at 37 degrees C with 200rpm agitation to mid-logarithmic growth phase (OD_{600} = 0.4-0.6) in DMEM + 10% FBS with or without M6 or M3 supplementation, or in CT26 supernatants treated with doxorubicin with or without QVD. Metabolites were supplemented at final concentrations of: spermidine (3mM), FBP (95mM), DHAP (20mM), GMP (16mM), IMP (17mM), and UDP-glucose (12mM). Once at mid-logarithmic growth, cultures were centrifuged at 13,000rpm for 10 minutes at 4 degrees C, and the resulting bacterial pellet was resuspended in Trizol and RNA was extracted and DNA removed using the RiboPure RNA Purification Kit according to the manufacturer's instructions.

OD600 measurements: Four millilitres of supernatant or medium controls were inoculated with 1:100 dilutions of overnight cultures of the indicated bacterial species. Cultures were grown at 37 degrees C with 200 rpm agitation (aerobic) and bacterial growth was quantified by OD600 measurements using the Ultrospec 10 (VWR) at the indicated time points.

Bacterial mutagenesis: *E. coli* mutant strains were constructed using lambda red homologous recombination as previously described[91] using the LR primers and plasmids listed in Key Resources. Correct unresolved insertions, antibiotic-resistance profiles, and subsequent resolved deletions after pCP20 transformation and flippase activity were verified using primers listed. For *in vivo* infections, fully resolved mutants were used to then make unresolved *lacZ* insertions as described above, but did not proceed to pCP20-mediated resolution.

Competitive infections: Wildtype C57BL6/J mice, aged 8-10 weeks, were injected with doxorubicin as above or left untreated. Overnight bacterial cultures were grown as above, spun down, and resuspended in 1x PBS to a concentration of 5e9 CFU per ml. Equal volumes of wildtype and mutant bacteria were added so that the final concentration of each strain was approximately 2.5e9 CFU per ml. 1 day post doxorubicin treatment, mice were infected via oral gavage with 5e8 CFU per mouse (2.5e8 CFU per strain) total in a 100 µl inoculum, composing of an approximate 1:1 ratio of wildtype and mutant bacteria (input). The ratio of strains in the input was confirmed by plating the infective dose on MacConkey agar plates containing chloramphenicol (final concentration 4µg per ml) and MacConkey agar plates containing kanamycin (final concentration 50µg per ml). Each strain was confirmed to only grow on the expected antibiotic, and intestinal lysates of uninfected animals treated with doxorubicin were confirmed to be free of chloramphenicol or kanamycin resistant bacteria that would grow on MacConkey agar. 1 day post-infection, corresponding to 2 days post-doxorubicin in treated animals, mice were euthanized and intestinal tissues harvested and lysed as described above. Intestinal lysate dilutions were plated onto MacConkey agar plates containing chloramphenicol (final concentration 4µg per ml) and MacConkey agar plates containing kanamycin (final concentration 50µg per ml) to calculate the ratio of the two strains (output). Competitive indices were calculated as [Output] / [Input] for each tissue. Given that each exogenously introduced strain was deficient for *lacZ*, and was a nonlactose fermenter, any lactose fermenting colonies were not counted and were viewed as "passenger" endogenous Enterobacteriaceae, though these events were rare.

Bacterial RNA sequencing

RNA sequencing was performed by Novogene. An mRNA library was constructed following rRNA depletion using NEBNext Ultra RNA Library Prep Kit for Illumni (NEB), sequencing was performed on the Illumina PE150 platform.

Analysis: Raw reads were first filtered by tile quality using the filterbytile function from bbmap v39.01. Illumina Adapter sequences and low quality bases were then removed through Trim Galore! V0.6.10 (with parameters stringency=5 and length=75) and trimmed sequences were mapped to E. coli HS strain genome assembly (GCF_000017765.1) using STAR v2.7.10 (parameters alignIntronMax=1000000 outFilterMultimapNma=5 and genome indexing with sjdbOverhang=149). Mapping of the reads resulted in 96.5% (87.62–98.8%) of reads uniquely aligned. Features were counted using featureCounts v2.0.1 and the the GTF version of the genome annotation.

R4.2.3 (R Foundation for Statistical Computing, Vienna, Austria) with DESeq2 v 1.38.3 and edgeR v 3.40.2 packages were used throughout the downstream processing and statistical analyses. Features with low read counts across samples were removed with the edgeR filterByExp function using a minimum number of CPM counts of 7 and accounting for the experimental design. Furthermore, samples with technical replicates were collapsed by summing their feature's counts.

DESeq was used to normalize the collapsed counts by correcting library depth with estimated dispersions calculated using a parametric model. DESeq then fitted a negative binomial distribution to allow hypothesis testing with the Wald method. Pairwise comparisons between the 3 treatments in the Doxorubicin and the metabolite supplementation experiments separately were performed. Two metrics were used to consider differentially expressed features: an adjusted p-value (false discovery rate) smaller than 0.05 as a relaxed method and an s-value < 0.005 as the conservative version. This s-value was calculated by shrinking the results with ashr v2.2 using a log fold change threshold of 0.7. GO term overrepresentation analysis was performed to all groups of significant (s-value or fdr) up or downregulated features in each comparison using the enrichGO function from clusterprofiler v4.8.3, correcting results with the Benjamini-Hochberg correction and considering significant GO terms those with a qvalue cutoff of 0.2 and a p-value cutoff of 0.05.

QUANTIFICATION AND STATISTICAL ANALYSIS

Data were assessed for normality by D'Agostino & Pearson and Shapiro-Wilk tests and appropriate statistical tests were chosen. Statistical tests are indicated in figure legends. Data were routinely assessed for outliers by ROUT (Q=1%). All information for data-specific statistical analyses (n, statistical test, etc) can be found in the figure legends.

REFERENCES

1. Deleemans, J.M., Chleilat, F., Reimer, R.A., Baydoun, M., Piedalue, K.-A., Lowry, D.E., Henning, J.-W., and Carlson, L.E. (2022). The Chemo-Gut Pilot Study: Associations between Gut Microbiota, Gastrointestinal Symptoms, and Psychosocial Health Outcomes in a Cross-Sectional Sample of Young Adult Cancer Survivors. Current Oncology *29*, 2973-2994. 10.3390/curroncol29050243.
2. Jones, J.A., Avritscher, E.B.C., Cooksley, C.D., Michelet, M., Bekele, B.N., and Elting, L.S. (2006). Epidemiology of treatment-associated mucosal injury after treatment with newer regimens for lymphoma, breast, lung, or colorectal cancer. Supportive Care in Cancer *14*, 505-515. 10.1007/s00520-006-0055-4.
3. Sonis, S., Elting, L., Keefe, D., Nguyen, H., Grunberg, S., Randolph-Jackson, P., and Brennan, M. (2015). Unanticipated frequency and consequences of regimen-related diarrhea in patients being treated with radiation or chemoradiation regimens for cancers of the head and neck or lung. Supportive Care in Cancer *23*, 433-439. 10.1007/s00520-014-2395-9.
4. Elting, L.S., Cooksley, C., Chambers, M., Cantor, S.B., Manzullo, E., and Rubenstein, E.B. (2003). The burdens of cancer therapy: Clinical and economic outcomes of chemotherapy-induced mucositis. Cancer. 10.1002/cncr.11671.
5. Montassier, E., Gastinne, T., Vangay, P., Al-Ghalith, G.A., Bruley Des Varannes, S., Massart, S., Moreau, P., Potel, G., De La Cochetière, M.F., Batard, E., and Knights, D. (2015). Chemotherapy-driven dysbiosis in the intestinal microbiome. Alimentary Pharmacology and Therapeutics. 10.1111/apt.13302.
6. Shin, N.R., Whon, T.W., and Bae, J.W. (2015). Proteobacteria: Microbial signature of dysbiosis in gut microbiota.
7. Gevers, D., Kugathasan, S., Lee, Vázquez-Baeza, Y., Will, Ren, B., Schwager, E., Knights, D., Se, Yassour, M., et al. (2014). The Treatment-Naive Microbiome in New-Onset Crohn’s Disease. Cell Host & Microbe *15*, 382-392. 10.1016/j.chom.2014.02.005.
8. Lupp, C., Robertson, M.L., Wickham, M.E., Sekirov, I., Champion, O.L., Gaynor, E.C., and Finlay, B.B. (2007). Host-Mediated Inflammation Disrupts the Intestinal Microbiota and Promotes the Overgrowth of Enterobacteriaceae. Cell Host & Microbe *2*, 119-129. 10.1016/j.chom.2007.06.010.
9. Walker, A.W., and Hoyles, L. (2023). Human microbiome myths and misconceptions. Nature Microbiology *8*, 1392-1396. 10.1038/s41564-023-01426-7.
10. Ni, J., Wu, G.D., Albenberg, L., and Tomov, V.T. (2017). Gut microbiota and IBD: causation or correlation? Nature Reviews Gastroenterology & Hepatology *14*, 573-584. 10.1038/nrgastro.2017.88.
11. Sonis, S.T. (2004). The pathobiology of mucositis. Nature Publishing Group.
12. van Vliet, M.J., Harmsen, H.J.M., de Bont, E.S.J.M., and Tissing, W.J.E. (2010). The Role of Intestinal Microbiota in the Development and Severity of Chemotherapy-Induced Mucositis. PLoS Pathogens *6*, 1-7. 10.1371/JOURNAL.PPAT.1000879.
13. Wei, L., Wen, X.S., and Xian, C.J. (2021). Chemotherapy-Induced Intestinal Microbiota Dysbiosis Impairs Mucosal Homeostasis by Modulating Toll-like Receptor Signaling Pathways. International Journal of Molecular Sciences *22*. 10.3390/IJMS22179474.
14. Pammi, M., Cope, J., Tarr, P.I., Warner, B.B., Morrow, A.L., Mai, V., Gregory, K.E., Kroll, J.S., McMurtry, V., Ferris, M.J., et al. (2017). Intestinal dysbiosis in preterm infants preceding necrotizing enterocolitis: a systematic review and meta-analysis. Microbiome *5*. 10.1186/s40168-017-0248-8.

15. Touchefeu, Y., Montassier, E., Nieman, K., Gastinne, T., Potel, G., Bruley Des Varannes, S., Le Vacon, F., and De La Cochetière, M.F. (2014). Systematic review: the role of the gut microbiota in chemotherapy- or radiation-induced gastrointestinal mucositis – current evidence and potential clinical applications. Alimentary Pharmacology & Therapeutics *40*, 409-421. 10.1111/APT.12878.
16. Chambers, L.M., Kuznicki, M., Yao, M., Chichura, A., Gruner, M., Reizes, O., Debernardo, R., Rose, P.G., Michener, C., and Vargas, R. (2020). Impact of antibiotic treatment during platinum chemotherapy on survival and recurrence in women with advanced epithelial ovarian cancer. Gynecologic Oncology *159*, 699-705. 10.1016/j.ygyno.2020.09.010.
17. Zhang, X., Yu, L., Shi, J., Li, S., Yang, S., Gao, W., Yang, S., Cheng, M., Wang, H., Guo, Z., and Geng, C. (2021). Antibiotics modulate neoadjuvant therapy efficiency in patients with breast cancer: a pilot analysis. Scientific Reports *11*. 10.1038/s41598-021-93428-w.
18. Flieger, D., Klassert, C., Hainke, S., Keller, R., Kleinschmidt, R., and Fischbach, W. (2007). Phase II Clinical Trial for Prevention of Delayed Diarrhea with Cholestyramine/Levofloxacin in the Second-Line Treatment with Irinotecan Biweekly in Patients with Metastatic Colorectal Carcinoma. Oncology *72*, 10-16. 10.1159/000111083.
19. De Jong, F.A., Kehrer, D.F.S., Mathijssen, R.H.J., Creemers, G.-J., De Bruijn, P., Van Schaik, R.H.N., Planting, A.S.T., Van Der Gaast, A., Eskens, F.A.L.M., Janssen, J.T.P., et al. (2006). Prophylaxis of Irinotecan-Induced Diarrhea with Neomycin and Potential Role for <i>UGT1A1*28</i> Genotype Screening: A Double-Blind, Randomized, Placebo-Controlled Study. The Oncologist *11*, 944-954. 10.1634/theoncologist.11-8-944.
20. Kim, S., Covington, A., and Pamer, E.G. (2017). The intestinal microbiota: Antibiotics, colonization resistance, and enteric pathogens. Immunological Reviews *279*, 90-105. 10.1111/imr.12563.
21. Iwamoto, M., Koji, T., Makiyama, K., Kobayashi, N., and Nakane, P.K. (1996). Apoptosis of crypt epithelial cells in ulcerative colitis. Journal of Pathology. 10.1002/(SICI)1096-9896(199610)180:2<152::AID-PATH649>3.0.CO;2-Y.
22. Boada-Romero, E., Martinez, J., Heckmann, B.L., and Green, D.R. (2020). The clearance of dead cells by efferocytosis.
23. Doran, A.C., Yurdagul, A., and Tabas, I. (2020). Efferocytosis in health and disease.
24. Mattioli, R., Ilari, A., Colotti, B., Mosca, L., Fazi, F., and Colotti, G. (2023). Doxorubicin and other anthracyclines in cancers: Activity, chemoresistance and its overcoming. Mol Aspects Med *93*, 101205. 10.1016/j.mam.2023.101205.
25. Peterson, D.E., Bensadoun, R.J., Roila, F., and Group, E.G.W. (2010). Management of oral and gastrointestinal mucositis: ESMO Clinical Practice Guidelines. Ann Oncol *21 Suppl 5*, v261-265. 10.1093/annonc/mdq197.
26. Ijiri, K., and Potten, C.S. (1987). Further studies on the response of intestinal crypt cells of different hierarchical status to eighteen different cytotoxic agents. British Journal of Cancer *55*, 113-113. 10.1038/BJC.1987.25.
27. Dekaney, C.M., Gulati, A.S., Garrison, A.P., Helmrath, M.A., and Henning, S.J. (2009). Regeneration of intestinal stem/progenitor cells following doxorubicin treatment of mice. American Journal of Physiology - Gastrointestinal and Liver Physiology. 10.1152/ajpgi.90446.2008.

28. Boussios, S., Pentheroudakis, G., Katsanos, K., and Pavlidis, N. (2012). Systemic treatment-induced gastrointestinal toxicity: Incidence, clinical presentation and management.
29. Mohammed, A.I., Celentano, A., Paolini, R., Low, J.T., McCullough, M.J., O' Reilly, L.A., and Cirillo, N. (2023). Characterization of a novel dual murine model of chemotherapy-induced oral and intestinal mucositis. Scientific Reports *13*. 10.1038/s41598-023-28486-3.
30. King, S.L., Mohiuddin, J.J., and Dekaney, C.M. (2013). Paneth cells expand from newly created and preexisting cells during repair after doxorubicin-induced damage. Am J Physiol Gastrointest Liver Physiol *305*, G151-162. 10.1152/ajpgi.00441.2012.
31. Sharpen, J.D.A., Dolan, B., Nyström, E.E.L., Birchenough, G.M.H., Arike, L., Martinez-Abad, B., Johansson, M.E.V., Hansson, G.C., and Recktenwald, C.V. (2022). Transglutaminase 3 crosslinks the secreted gel-forming mucus component Mucin-2 and stabilizes the colonic mucus layer. Nature Communications *13*. 10.1038/s41467-021-27743-1.
32. Garabedian, E.M., Roberts, L.J.J., McNevin, M.S., and Gordon, J.I. (1997). Examining the Role of Paneth Cells in the Small Intestine by Lineage Ablation in Transgenic Mice. Journal of Biological Chemistry *272*, 23729-23740. 10.1074/jbc.272.38.23729.
33. Anderson, C.J., Medina, C.B., Barron, B.J., Karvelyte, L., Aaes, T.L., Lambertz, I., Perry, J.S.A., Mehrotra, P., Gonçalves, A., Lemeire, K., et al. (2021). Microbes exploit death-induced nutrient release by gut epithelial cells. Nature 2021 596:7871 *596*, 262-267. 10.1038/s41586-021-03785-9.
34. Ghazavi, F., Huysentruyt, J., Coninck, J.D., Kourula, S., Martens, S., Hassannia, B., Wartewig, T., Divert, T., Roelandt, R., Popper, B., et al. (2022). Executioner caspases 3 and 7 are dispensable for intestinal epithelium turnover and homeostasis at steady state. Proceedings of the National Academy of Sciences *119*, e2024508119-e2024508119. 10.1073/PNAS.2024508119.
35. Pacheco, A.R., Curtis, M.M., Ritchie, J.M., Munera, D., Waldor, M.K., Moreira, C.G., and Sperandio, V. (2012). Fucose sensing regulates bacterial intestinal colonization. Nature *492*, 113-117. 10.1038/nature11623.
36. Harrison, S.D., Jr. (1981). Toxicologic evaluation of cis-diamminedichloroplatinum II in B6D2F1 mice. Fundam Appl Toxicol *1*, 382-385.
37. Bearcroft, C.P., Domizio, P., Mourad, F.H., Andre, E.A., and Farthing, M.J. (1999). Cisplatin impairs fluid and electrolyte absorption in rat small intestine: a role for 5-hydroxytryptamine. Gut *44*, 174-179. 10.1136/gut.44.2.174.
38. Hu, J.N., Yang, J.Y., Jiang, S., Zhang, J., Liu, Z., Hou, J.G., Gong, X.J., Wang, Y.P., Wang, Z., and Li, W. (2021). Panax quinquefolium saponins protect against cisplatin evoked intestinal injury via ROS-mediated multiple mechanisms. Phytomedicine *82*, 153446. 10.1016/j.phymed.2020.153446.
39. Perše, M. (2021). Cisplatin Mouse Models: Treatment, Toxicity and Translatability. Biomedicines *9*, 1406. 10.3390/biomedicines9101406.
40. Khan, R., Khan, A.Q., Qamar, W., Lateef, A., Tahir, M., Rehman, M.U., Ali, F., and Sultana, S. (2012). Chrysin protects against cisplatin-induced colon. toxicity via amelioration of oxidative stress and apoptosis: probable role of p38MAPK and p53. Toxicol Appl Pharmacol *258*, 315-329. 10.1016/j.taap.2011.11.013.
41. Zhao, L., Xing, C., Sun, W., Hou, G., Yang, G., and Yuan, L. (2018). Lactobacillus supplementation prevents cisplatin-induced cardiotoxicity possibly by inflammation

inhibition. Cancer Chemotherapy and Pharmacology *82*, 999-1008. 10.1007/S00280-018-3691-8/FIGURES/4.

42. Franzosa, E.A., McIver, L.J., Rahnavard, G., Thompson, L.R., Schirmer, M., Weingart, G., Lipson, K.S., Knight, R., Caporaso, J.G., Segata, N., and Huttenhower, C. (2018). Species-level functional profiling of metagenomes and metatranscriptomes. Nat Methods *15*, 962-968. 10.1038/s41592-018-0176-y.
43. Chanin, R.B., Winter, M.G., Spiga, L., Hughes, E.R., Zhu, W., Taylor, S.J., Arenales, A., Gillis, C.C., Büttner, L., Jimenez, A.G., et al. (2020). Epithelial-Derived Reactive Oxygen Species Enable AppBCX-Mediated Aerobic Respiration of Escherichia coli during Intestinal Inflammation. Cell Host & Microbe *28*, 780-788.e785. 10.1016/j.chom.2020.09.005.
44. Hughes, E.R., Winter, M.G., Duerkop, B.A., Spiga, L., Furtado De Carvalho, T., Zhu, W., Gillis, C.C., Büttner, L., Smoot, M.P., Behrendt, C.L., et al. (2017). Microbial Respiration and Formate Oxidation as Metabolic Signatures of Inflammation-Associated Dysbiosis. Cell Host & Microbe *21*, 208-219. 10.1016/j.chom.2017.01.005.
45. Byndloss, M.X., Olsan, E.E., Rivera-Chavez, F., Tiffany, C.R., Cevallos, S.A., Lokken, K.L., Torres, T.P., Byndloss, A.J., Faber, F., Gao, Y., et al. (2017). Microbiota-activated PPAR-gamma signaling inhibits dysbiotic Enterobacteriaceae expansion. Science *357*, 570-575. 10.1126/science.aam9949.
46. Castle, J.C., Loewer, M., Boegel, S., de Graaf, J., Bender, C., Tadmor, A.D., Boisguerin, V., Bukur, T., Sorn, P., Paret, C., et al. (2014). Immunomic, genomic and transcriptomic characterization of CT26 colorectal carcinoma. BMC Genomics *15*, 190. 10.1186/1471-2164-15-190.
47. Miller, B.M., Liou, M.J., Zhang, L.F., Nguyen, H., Litvak, Y., Schorr, E.-M., Jang, K.K., Tiffany, C.R., Butler, B.P., and Bäumler, A.J. (2020). Anaerobic Respiration of NOX1-Derived Hydrogen Peroxide Licenses Bacterial Growth at the Colonic Surface. Cell Host & Microbe *28*, 789-797.e785. 10.1016/j.chom.2020.10.009.
48. Chioccioli, S., Del Duca, S., Vassallo, A., Castronovo, L.M., and Fani, R. (2020). Exploring the role of the histidine biosynthetic hisF gene in cellular metabolism and in the evolution of (ancestral) genes: from LUCA to the extant (micro)organisms. Microbiol Res *240*, 126555. 10.1016/j.micres.2020.126555.
49. Rodionova, I.A., Gao, Y., Sastry, A., Hefner, Y., Lim, H.G., Rodionov, D.A., Saier, M.H., and Palsson, B.O. (2021). Identification of a transcription factor, PunR, that regulates the purine and purine nucleoside transporter punC in E. coli. Communications Biology *4*. 10.1038/s42003-021-02516-0.
50. Patching, S.G., Baldwin, S.A., Baldwin, A.D., Young, J.D., Gallagher, M.P., Henderson, P.J.F., and Herbert, R.B. (2005). The nucleoside transport proteins, NupC and NupG, from Escherichia coli: specific structural motifs necessary for the binding of ligands. Organic & Biomolecular Chemistry *3*, 462. 10.1039/b414739a.
51. Petersen, C., and Møller, L.B. (2001). The RihA, RihB, and RihC Ribonucleoside Hydrolases of Escherichia coli. Journal of Biological Chemistry *276*, 884-894. 10.1074/jbc.m008300200.
52. Kasahara, K., Kerby, R.L., Zhang, Q., Pradhan, M., Mehrabian, M., Lusis, A.J., Bergström, G., Bäckhed, F., and Rey, F.E. (2023). Gut bacterial metabolism contributes to host global purine homeostasis. Cell Host & Microbe *31*, 1038-1053.e1010. 10.1016/j.chom.2023.05.011.

53. Medina, C.B., Mehrotra, P., Arandjelovic, S., Perry, J.S.A., Guo, Y., Morioka, S., Barron, B., Walk, S.F., Ghesquière, B., Krupnick, A.S., et al. (2020). Metabolites released from apoptotic cells act as tissue messengers. Nature. 10.1038/s41586-020-2121-3.
54. Rowley, C.A., Sauder, A.B., and Kendall, M.M. (2020). The Ethanolamine-Sensing Transcription Factor EutR Promotes Virulence and Transmission during Citrobacter rodentium Intestinal Infection. Infect Immun *88*. 10.1128/IAI.00137-20.
55. Jones, S.A., Chowdhury, F.Z., Fabich, A.J., Anderson, A., Schreiner, D.M., House, A.L., Autieri, S.M., Leatham, M.P., Lins, J.J., Jorgensen, M., et al. (2007). Respiration of Escherichia coli in the mouse intestine. Infect Immun *75*, 4891-4899. 10.1128/IAI.00484-07.
56. Winter, S.E., Winter, M.G., Xavier, M.N., Thiennimitr, P., Poon, V., Keestra, A.M., Laughlin, R.C., Gomez, G., Wu, J., Lawhon, S.D., et al. (2013). Host-Derived Nitrate Boosts Growth of E. coli in the Inflamed Gut. Science *339*, 708-711. 10.1126/science.1232467.
57. Lopez, C.A., Rivera-Chávez, F., Byndloss, M.X., and Bäumler, A.J. (2015). The Periplasmic Nitrate Reductase NapABC Supports Luminal Growth of Salmonella enterica Serovar Typhimurium during Colitis. Infection and Immunity *83*, 3470-3478. 10.1128/IAI.00351-15.
58. Mason, M.G., Shepherd, M., Nicholls, P., Dobbin, P.S., Dodsworth, K.S., Poole, R.K., and Cooper, C.E. (2009). Cytochrome bd confers nitric oxide resistance to Escherichia coli. Nature Chemical Biology *5*, 94-96. 10.1038/nchembio.135.
59. Glaser, M., Nulty, W., and Vagelos, P.R. (1975). Role of adenylate kinase in the regulation of macromolecular biosynthesis in a putative mutant of Escherichia coli defective in membrane phospholipid biosynthesis. J Bacteriol *123*, 128-136. 10.1128/jb.123.1.128-136.1975.
60. Montassier, E., Batard, E., Massart, S., Gastinne, T., Carton, T., Caillon, J., Le Fresne, S., Caroff, N., Hardouin, J.B., Moreau, P., et al. (2014). 16S rRNA gene pyrosequencing reveals shift in patient faecal microbiota during high-dose chemotherapy as conditioning regimen for bone marrow transplantation. Microbial ecology *67*, 690-699. 10.1007/S00248-013-0355-4/FIGURES/8.
61. Rigby, R.J., Carr, J., Orgel, K., King, S.L., Lund, P.K., and Dekaney, C.M. (2016). Intestinal bacteria are necessary for doxorubicin-induced intestinal damage but not for doxorubicin-induced apoptosis. Gut Microbes. 10.1080/19490976.2016.1215806.
62. Carr, J.S., King, S., and Dekaney, C.M. (2017). Depletion of enteric bacteria diminishes leukocyte infiltration following doxorubicininduced small intestinal damage in mice. PLoS ONE *12*. 10.1371/journal.pone.0173429.
63. Rivera-Chávez, F., Zhang, L.F., Faber, F., Lopez, C.A., Byndloss, M.X., Olsan, E.E., Xu, G., Velazquez, E.M., Lebrilla, C.B., Winter, S.E., and Bäumler, A.J. (2016). Depletion of Butyrate-Producing Clostridia from the Gut Microbiota Drives an Aerobic Luminal Expansion of Salmonella. Cell Host & Microbe *19*, 443-454. 10.1016/j.chom.2016.03.004.
64. Desai, M.S., Seekatz, A.M., Koropatkin, N.M., Kamada, N., Hickey, C.A., Wolter, M., Pudlo, N.A., Kitamoto, S., Terrapon, N., Muller, A., et al. (2016). A Dietary Fiber-Deprived Gut Microbiota Degrades the Colonic Mucus Barrier and Enhances Pathogen Susceptibility. Cell *167*, 1339-1353.e1321. 10.1016/j.cell.2016.10.043.
65. Wolter, M., Grant, E.T., Boudaud, M., Pudlo, N.A., Pereira, G.V., Eaton, K.A., Martens, E.C., and Desai, M.S. (2024). Diet-driven differential response of Akkermansia

muciniphila modulates pathogen susceptibility. Molecular Systems Biology *20*, 596-625. 10.1038/s44320-024-00036-7.

66. Zhu, W., Winter, M.G., Byndloss, M.X., Spiga, L., Duerkop, B.A., Hughes, E.R., Büttner, L., De Lima Romão, E., Behrendt, C.L., Lopez, C.A., et al. (2018). Precision editing of the gut microbiota ameliorates colitis. Nature *553*, 208-211. 10.1038/nature25172.
67. Duszyc, K., von Pein, J.B., Ramnath, D., Currin-Ross, D., Verma, S., Lim, F., Sweet, M.J., Schroder, K., and Yap, A.S. (2023). Apical extrusion prevents apoptosis from activating an acute inflammatory program in epithelia. Dev Cell. 10.1016/j.devcel.2023.08.009.
68. Christgen, S., Zheng, M., Kesavardhana, S., Karki, R., Malireddi, R.K.S., Banoth, B., Place, D.E., Briard, B., Sharma, B.R., Tuladhar, S., et al. (2020). Identification of the PANoptosome: A Molecular Platform Triggering Pyroptosis, Apoptosis, and Necroptosis (PANoptosis). Frontiers in Cellular and Infection Microbiology *10*, 237-237. 10.3389/fcimb.2020.00237.
69. Goh, E.B., Bledsoe, P.J., Chen, L.L., Gyaneshwar, P., Stewart, V., and Igo, M.M. (2005). Hierarchical control of anaerobic gene expression in Escherichia coli K-12: the nitrate-responsive NarX-NarL regulatory system represses synthesis of the fumarate-responsive DcuS-DcuR regulatory system. J Bacteriol *187*, 4890-4899. 10.1128/JB.187.14.4890-4899.2005.
70. Tan, C.A.Z., Chong, K.K.L., Yeong, D.Y.X., Ng, C.H.M., Ismail, M.H., Yap, Z.H., Khetrapal, V., Tay, V.S.Y., Drautz-Moses, D.I., Ali, Y., et al. (2024). Purine and carbohydrate availability drive Enterococcus faecalis fitness during wound and urinary tract infections. mBio *15*, e0238423. 10.1128/mbio.02384-23.
71. Schirmer, M., Strazar, M., Avila-Pacheco, J., Rojas-Tapias, D.F., Brown, E.M., Temple, E., Deik, A., Bullock, K., Jeanfavre, S., Pierce, K., et al. (2024). Linking microbial genes to plasma and stool metabolites uncovers host-microbial interactions underlying ulcerative colitis disease course. Cell Host Microbe *32*, 209-226 e207. 10.1016/j.chom.2023.12.013.
72. Zeng, B., Huang, Y., Chen, S., Xu, R., Xu, L., Qiu, J., Shi, F., Liu, S., Zha, Q., Ouyang, D., and He, X. (2022). Dextran sodium sulfate potentiates NLRP3 inflammasome activation by modulating the KCa3.1 potassium channel in a mouse model of colitis. Cellular & Molecular Immunology *19*, 925-943. 10.1038/s41423-022-00891-0.
73. Rasko, D.A., Rosovitz, M.J., Myers, G.S.A., Mongodin, E.F., Fricke, W.F., Gajer, P., Crabtree, J., Sebaihia, M., Thomson, N.R., Chaudhuri, R., et al. (2008). The Pangenome Structure of Escherichia coli: Comparative Genomic Analysis of E. coli Commensal and Pathogenic Isolates. Journal of Bacteriology *190*, 6881-6893. 10.1128/JB.00619-08.
74. Jason, Ravindran, R., Chassaing, B., Frederic, Mohan, Bower, M., Hakimpour, P., Kiran, Helder, Yarovinsky, F., et al. (2014). TLR5-Mediated Sensing of Gut Microbiota Is Necessary for Antibody Responses to Seasonal Influenza Vaccination. Immunity *41*, 478-492. 10.1016/j.immuni.2014.08.009.
75. Slowicka, K., Petta, I., Blancke, G., Hoste, E., Dumas, E., Sze, M., Vikkula, H., Radaelli, E., Haigh, J.J., Jonckheere, S., et al. (2020). Zeb2 drives invasive and microbiota-dependent colon carcinoma. Nature Cancer 2020 1:6 *1*, 620-634. 10.1038/s43018-020-0070-2.
76. Steimle, A., De Sciscio, A., Neumann, M., Grant, E.T., Pereira, G.V., Ohno, H., Martens, E.C., and Desai, M.S. (2021). Constructing a gnotobiotic mouse model with a

synthetic human gut microbiome to study host–microbe cross talk. STAR Protocols *2*, 100607-100607. 10.1016/J.XPRO.2021.100607.

77. Callahan, B.J., McMurdie, P.J., and Holmes, S.P. (2017). Exact sequence variants should replace operational taxonomic units in marker-gene data analysis. The ISME Journal *11*, 2639-2643. 10.1038/ismej.2017.119.
78. Callahan, B.J., McMurdie, P.J., Rosen, M.J., Han, A.W., Johnson, A.J.A., and Holmes, S.P. (2016). DADA2: High-resolution sample inference from Illumina amplicon data. Nature Methods *13*, 581-583. 10.1038/nmeth.3869.
79. Straub, D., Blackwell, N., Langarica-Fuentes, A., Peltzer, A., Nahnsen, S., and Kleindienst, S. (2020). Interpretations of Environmental Microbial Community Studies Are Biased by the Selected 16S rRNA (Gene) Amplicon Sequencing Pipeline. Front Microbiol *11*, 550420. 10.3389/fmicb.2020.550420.
80. Martin, M. (2011). Cutadapt removes adapter sequences from high-throughput sequencing reads. EMBnet.journal *17*, 10. 10.14806/ej.17.1.200.
81. Douglas, G.M., Maffei, V.J., Zaneveld, J.R., Yurgel, S.N., Brown, J.R., Taylor, C.M., Huttenhower, C., and Langille, M.G.I. (2020). PICRUSt2 for prediction of metagenome functions. Nature Biotechnology *38*, 685-688. 10.1038/s41587-020-0548-6.
82. Barbera, P., Kozlov, A.M., Czech, L., Morel, B., Darriba, D., Flouri, T., and Stamatakis, A. (2019). EPA-ng: Massively Parallel Evolutionary Placement of Genetic Sequences. Syst Biol *68*, 365-369. 10.1093/sysbio/syy054.
83. Czech, L., Barbera, P., and Stamatakis, A. (2020). Genesis and Gappa: processing, analyzing and visualizing phylogenetic (placement) data. Bioinformatics *36*, 3263-3265. 10.1093/bioinformatics/btaa070.
84. Mirarab, S., Nguyen, N., and Warnow, T. (2012). SEPP: SATe-enabled phylogenetic placement. Pac Symp Biocomput, 247-258. 10.1142/9789814366496_0024.
85. Louca, S., and Doebeli, M. (2018). Efficient comparative phylogenetics on large trees. Bioinformatics *34*, 1053-1055. 10.1093/bioinformatics/btx701.
86. Caspi, R., Foerster, H., Fulcher, C.A., Kaipa, P., Krummenacker, M., Latendresse, M., Paley, S., Rhee, S.Y., Shearer, A.G., Tissier, C., et al. (2008). The MetaCyc Database of metabolic pathways and enzymes and the BioCyc collection of Pathway/Genome Databases. Nucleic Acids Res *36*, D623-631. 10.1093/nar/gkm900.
87. Tsugawa, H., Kind, T., Nakabayashi, R., Yukihira, D., Tanaka, W., Cajka, T., Saito, K., Fiehn, O., and Arita, M. (2016). Hydrogen Rearrangement Rules: Computational MS/MS Fragmentation and Structure Elucidation Using MS-FINDER Software. Anal Chem *88*, 7946-7958. 10.1021/acs.analchem.6b00770.
88. Horai, H., Arita, M., Kanaya, S., Nihei, Y., Ikeda, T., Suwa, K., Ojima, Y., Tanaka, K., Tanaka, S., Aoshima, K., et al. (2010). MassBank: a public repository for sharing mass spectral data for life sciences. J Mass Spectrom *45*, 703-714. 10.1002/jms.1777.
89. Wang, M., Carver, J.J., Phelan, V.V., Sanchez, L.M., Garg, N., Peng, Y., Nguyen, D.D., Watrous, J., Kapono, C.A., Luzzatto-Knaan, T., et al. (2016). Sharing and community curation of mass spectrometry data with Global Natural Products Social Molecular Networking. Nature Biotechnology *34*, 828-837. 10.1038/nbt.3597.
90. Sawada, Y., Nakabayashi, R., Yamada, Y., Suzuki, M., Sato, M., Sakata, A., Akiyama, K., Sakurai, T., Matsuda, F., Aoki, T., et al. (2012). RIKEN tandem mass spectral database (ReSpect) for phytochemicals: a plant-specific MS/MS-based data resource and database. Phytochemistry *82*, 38-45. 10.1016/j.phytochem.2012.07.007.

91. Datsenko, K.A., and Wanner, B.L. (2000). One-Step Inactivation of Chromosomal Genes in Escherichia Coli K-12 Using PCR Products. Proceedings of the National Academy of Sciences of the United States of America *97*, 6640-6645.

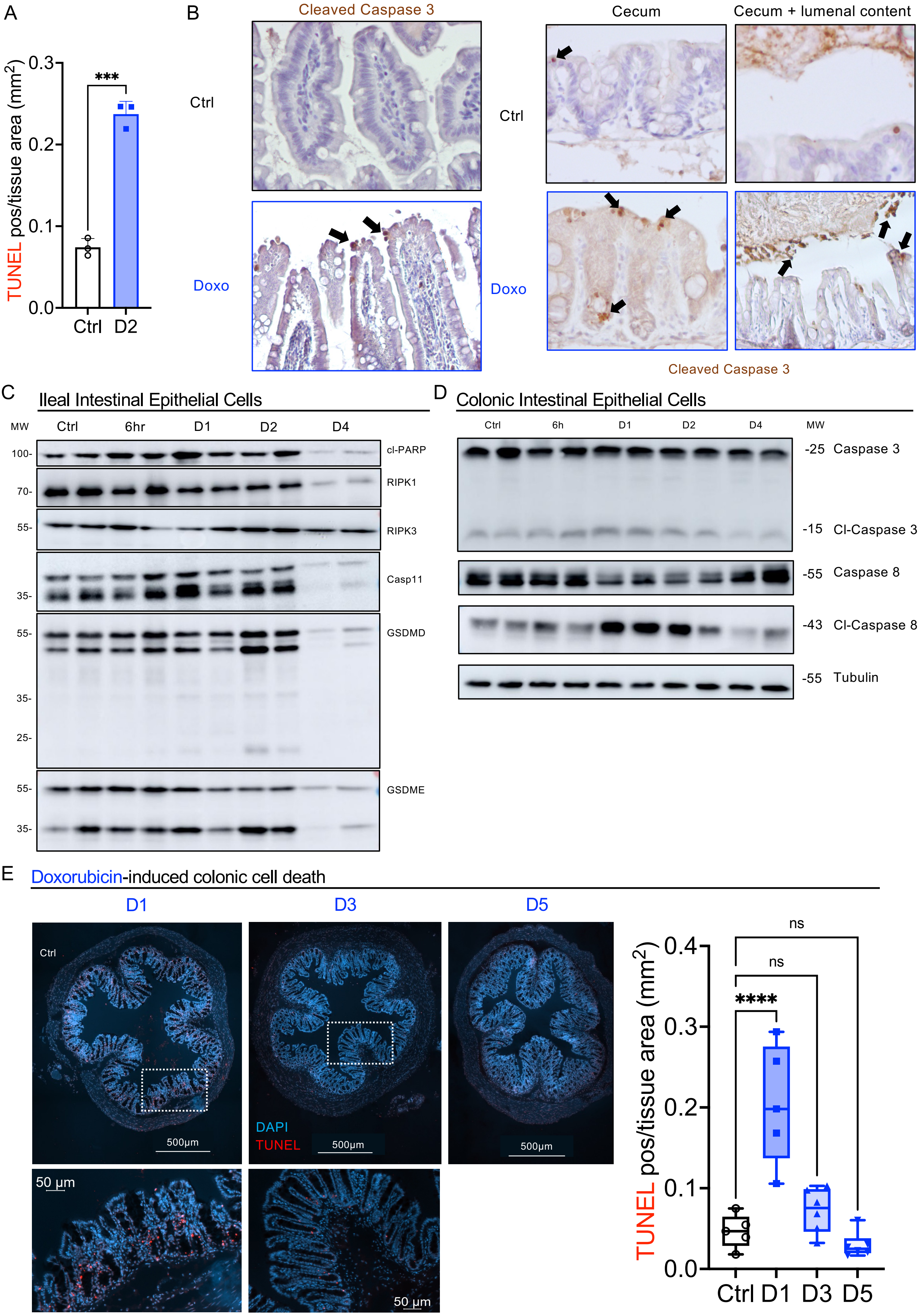
A
0.3
0.2
0.1
0.0
***
TUNEL pos/tissue area (mm^2)
Ctrl
D2
B
Cleaved Caspase 3
Ctrl
Doxo
Cecum
Cecum + lumenal content
Ctrl
Doxo
Cleaved Caspase 3
C
Ileal Intestinal Epithelial Cells
MW
Ctrl
6hr
D1
D2
D4
100-
70-
55-
35-
55-
35-
25-
55-
35-
cl-PARP
RIPK1
RIPK3
Casp11
GSDMD
GSDME
D
Colonic Intestinal Epithelial Cells
Ctrl
6h
D1
D2
D4
MW
-25
Caspase 3
-15
Cl-Caspase 3
-55
Caspase 8
-43
Cl-Caspase 8
-55
Tubulin
E
Doxorubicin-induced colonic cell death
D1
D3
D5
Ctrl
DAPI
TUNEL
500μm
500μm
500μm
50 μm
50 μm
0.4
0.3
0.2
0.1
0.0
ns
ns
****
TUNEL pos/tissue area (mm^2)
Ctrl
D1
D3
D5

Supplementary Figure 1 (corresponding with Main Text Figure 1)
Doxorubicin induces intestinal apoptosis.

- **A.** TUNEL positive cells per ileum tissue section area (mm^2) at indicated days post-doxorubicin (n= 3 mice per group, averaged values of 5-10 sections per mouse shown). Significance determined by unpaired t test. Mean + standard deviation is shown with individual replicates displayed.
- **B.** Cleaved caspase 3 staining in the ileum (left) or cecum (right) or control untreated mice or mice day 1 post-doxorubicin treatment. Black arrows indicate cleaved caspase 3 positive cells.
- **C.** Immunoblot of the indicated cell death effector proteins. Cell lysates were prepped from ileal intestinal epithelial cells isolated at the indicated time post-doxorubicin treatment *in vivo* (n= 2 per time point shown). Loading controls from these lysates are shown in Figure 1F.
- **D.** Immunoblot of the indicated apoptosis or loading control (tubulin) proteins. Cell lysates were prepped from colonic intestinal epithelial cells isolated at the indicated time post-doxorubicin treatment *in vivo* (n= 2 per time point shown).
- **E.** TUNEL positive cells per colon tissue section area (mm^2) at indicated days post-doxorubicin (n= 5-6 mice per group, averaged values of 5-10 sections per mouse shown, n=2 cohorts). Significance determined by one-way ANOVA with Dunnett's multiple comparisons test. Box and whiskers show minimum to maximum values with all independent replicates, center denotes median, and the bounds denote the 25th to 75th percentiles.

For A-E, ns $p > 0.05$, * $p \leq 0.05$, ** $p \leq 0.005$, *** $p \leq 0.0005$, **** $p \leq 0.0001$.

A

Doxorubicin-induced disease

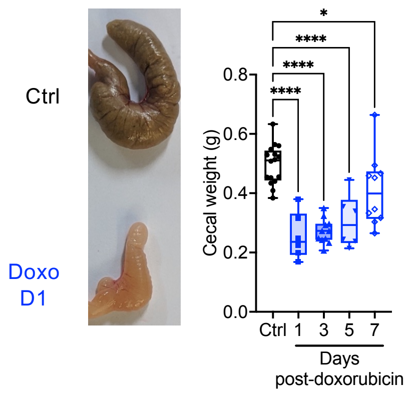

B

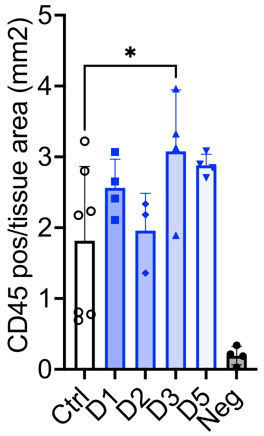

Doxorubicin-induced ileal mucus-producing cells

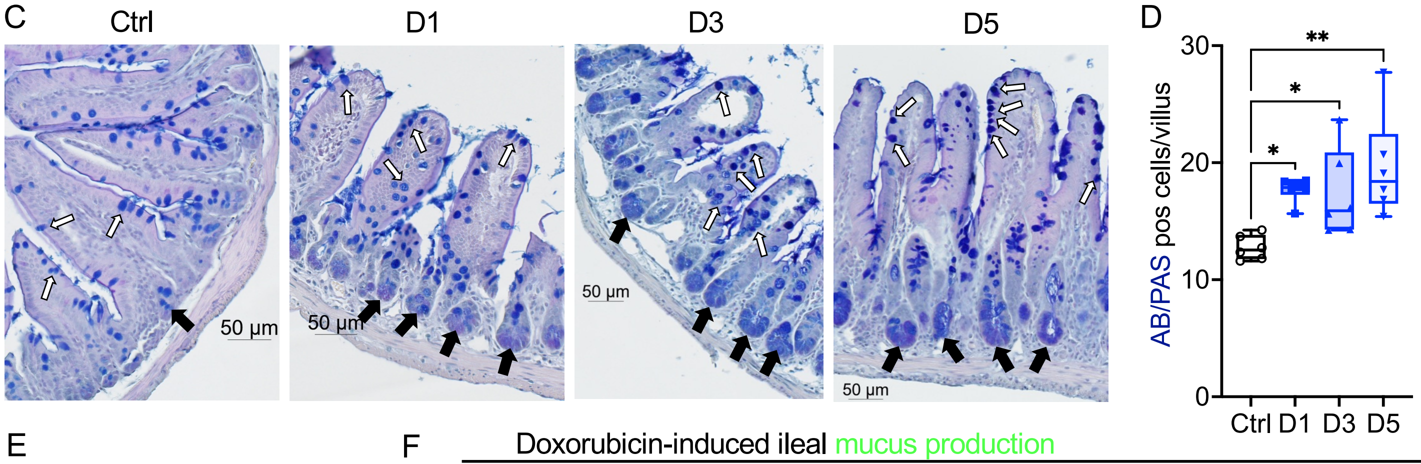

E

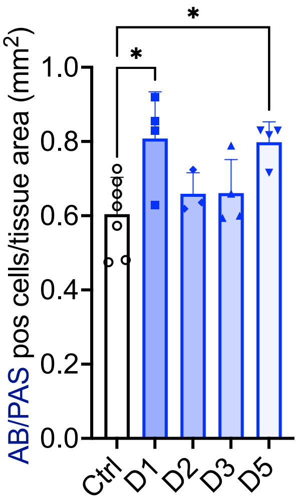

F

Doxorubicin-induced ileal mucus production

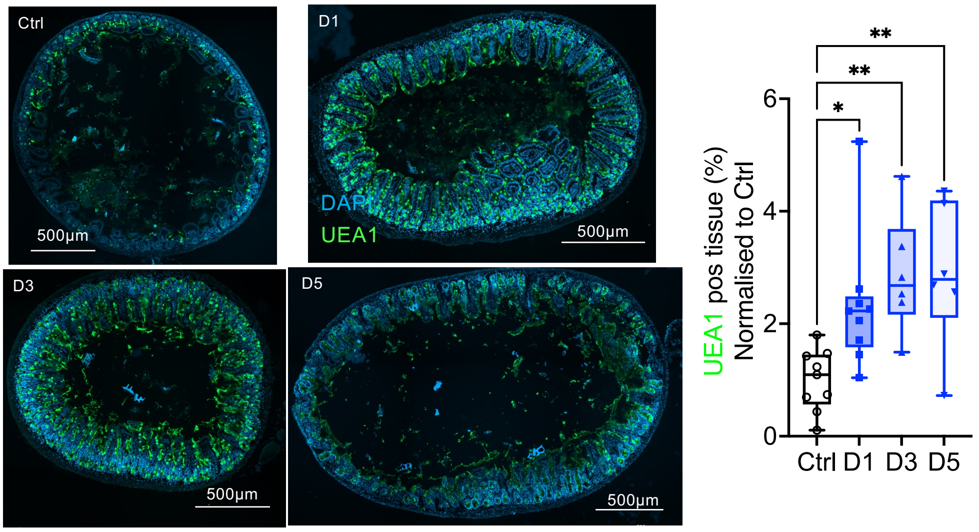

G

Doxorubicin-induced colonic mucus production

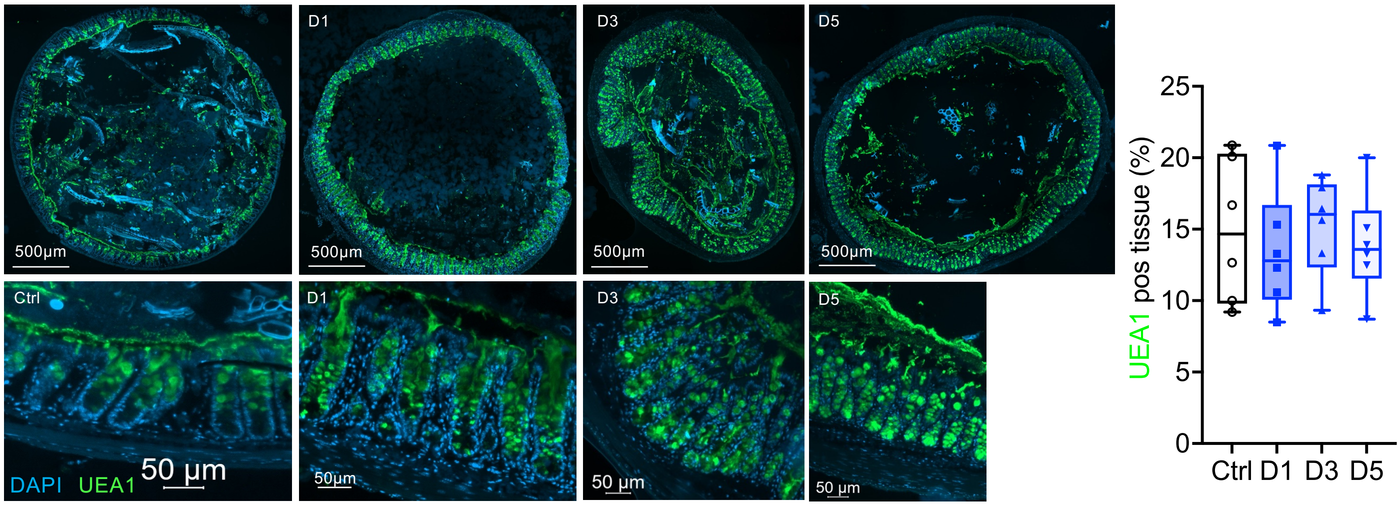

Supplementary Figure 2 (corresponding with Main Text Figure 1)
Doxorubicin induces intestinal mucositis.

- **A.** Image of control or day 1 post-doxorubicin treated ceca (left) and corresponding cecal weights at the indicated times post-treatment (n= 6-16 per time point, n= 4 cohorts). Significance determined by one-way ANOVA with Holm-Sidak's multiple comparisons test. Box and whiskers show minimum to maximum values with all independent replicates, center denotes median, and the bounds denote the 25th to 75th percentiles.
- **B.** CD45 positive cells per ileal tissue section area (mm^2) at indicated days post-doxorubicin (n= 3-6 per time point, averaged values of 5-10 sections per mouse shown, n=2 cohorts). "Neg" refers to unstained controls. Mean + standard deviation is shown with individual replicates displayed.
- **C.** Representative Alcian Blue-PAS-stained ileal tissue sections of the indicated times post-doxorubicin treatment. White arrows indicate AB-PAS positive cells located within the villi (goblet cells). Black arrows indicate AB-PAS positive cells located within the crypts (Paneth cells).
- **D.** Number of Alcian Blue-PAS positive cells per villus in the ilea at the indicated times post-doxorubicin treatment (n= 6 mice per group, averaged values of 5-10 tissue sections per mouse shown, n=2 cohorts). Significance determined by one-way ANOVA with Dunnett's multiple comparisons test. Box and whiskers show minimum to maximum values with all independent replicates, center denotes median, and the bounds denote the 25th to 75th percentiles.
- **E.** Number of Alcian Blue-PAS positive cells ileal tissue area (mm^2) at the indicated times post-doxorubicin treatment (n= 3-6 mice per group, averaged values of 5-10 tissue sections per mouse shown, n=2 cohorts). Significance determined by one-way ANOVA with Dunnett's multiple comparisons test. Mean + standard deviation is shown with individual replicates displayed.
- **F.** Representative DAPI and UEA1 stained ileal tissue sections of control untreated or indicated times post-doxorubicin treated animals. Lower images are higher magnification of the matched image above. UEA1 positive fluorescence as a percentage of ileum tissue area (n= 6-9 mice per group, averaged values of 5-10 tissue sections per mouse shown, n=2 cohorts) normalized to control untreated animals, corresponding to the data in Figure 1H. Significance determined by one-way ANOVA with Dunnett's multiple comparisons test. Box and whiskers show minimum to maximum values with all independent replicates, center denotes median, and the bounds denote the 25th to 75th percentiles.
- **G.** Representative DAPI and UEA1 stained colonic tissue sections of control untreated or indicated times post-doxorubicin treated animals. Lower images are higher magnification of the matched image above (left). UEA1 positive fluorescence as a percentage of colon tissue area (n= 6-9 mice per group, averaged values of 5-10 tissue sections per mouse shown, n=2 cohorts). Box and whiskers show minimum to maximum values with all independent replicates, center denotes median, and the bounds denote the 25th to 75th percentiles.

For A-G, ns $p > 0.05$, * $p \leq 0.05$, ** $p \leq 0.005$, *** $p \leq 0.0005$, **** $p \leq 0.0001$.

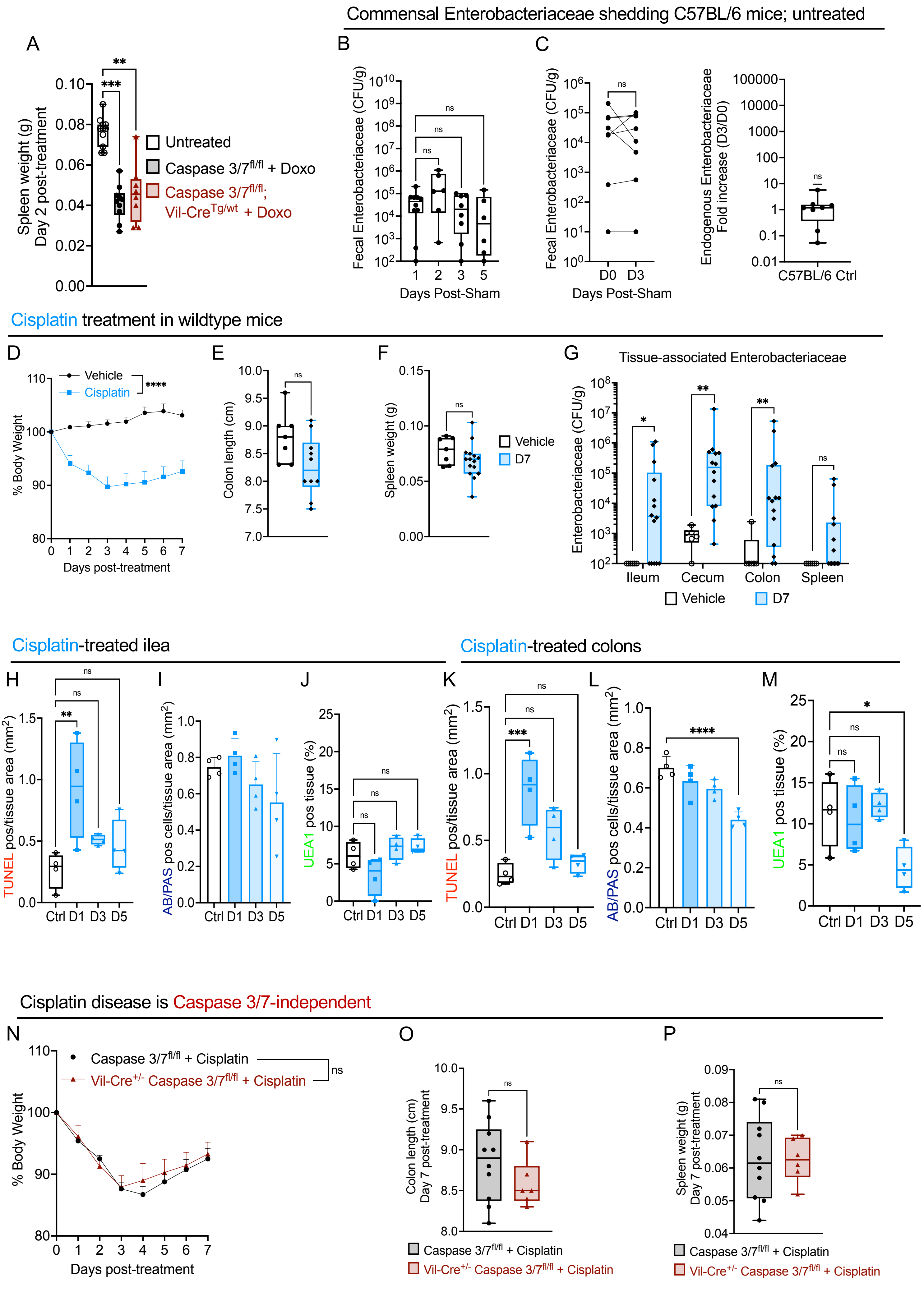
Commensal Enterobacteriaceae shedding C57BL/6 mice; untreated
A
Spleen weight (g) Day 2 post-treatment
0.10
0.08
0.06
0.04
0.02
0.00
***
**
Untreated
Caspase 3/7fl/fl + Doxo
Caspase 3/7fl/fl; Vil-CreTg/wt + Doxo
B
Fecal Enterobacteriaceae (CFU/g)
Days Post-Sham
1 2 3 5
ns
C
Fecal Enterobacteriaceae (CFU/g)
D0 D3
Days Post-Sham
Endogenous Enterobacteriaceae Fold increase (D3/D0)
100000
10000
1000
100
10
1
0.1
0.01
C57BL/6 Ctrl
Cisplatin treatment in wildtype mice
D
% Body Weight
Vehicle
Cisplatin
****
Days post-treatment
E
Colon length (cm)
F
Spleen weight (g)
Vehicle
D7
G
Tissue-associated Enterobacteriaceae
Enterobacteriaceae (CFU/g)
Ileum Cecum Colon Spleen
*
Cisplatin-treated ilea
Cisplatin-treated colons
H
TUNEL pos/tissue area (mm2)
I
AB/PAS pos cells/tissue area (mm2)
J
UEA1 pos tissue (%)
K
TUNEL pos/tissue area (mm2)
L
AB/PAS pos cells/tissue area (mm2)
M
UEA1 pos tissue (%)
Ctrl D1 D3 D5
Cisplatin disease is Caspase 3/7-independent
N
% Body Weight
Caspase 3/7fl/fl + Cisplatin
Vil-Cre+/- Caspase 3/7fl/fl + Cisplatin
ns
Days post-treatment
O
Colon length (cm) Day 7 post-treatment
P
Spleen weight (g) Day 7 post-treatment
Caspase 3/7fl/fl + Cisplatin
Vil-Cre+/- Caspase 3/7fl/fl + Cisplatin

Supplementary Figure 3 (corresponding with Main Text Figure 2)
Chemotherapy-induced dysbiosis and disease.

- **A.** Spleen weights (grams) of the indicated treatment and genotype at day 2 post-treatment (n= 8-11 per group). Significance determined by Kruskal-Wallis with Dunn's multiple comparisons test. Box and whiskers show minimum to maximum values with all independent replicates, center denotes median, and the bounds denote the 25th to 75th percentiles.
- **B.** Enterobacteriaceae CFU per gram of fecal content from wildtype C57BL/6J mice at the indicated day post-sham treatment (n= 6-10 per time point). Significance determined by Kruskal-Wallis with Dunn's multiple comparisons test comparing each time point to control. Box and whiskers show minimum to maximum values with all independent replicates, center denotes median, and the bounds denote the 25th to 75th percentiles.
- **C.** Enterobacteriaceae CFU per gram of fecal content from wildtype C57BL/6J mice at the indicated day post-sham treatment from paired samples (left, n= 6). Significance determined by Wilcoxon matched-pairs signed rank test. Enterobacteriaceae fold change (right). Day 3 post-sham CFU in feces was normalized to the starting day 0 CFU for each mouse (n= 8). Significance determined by Wilcoxon signed rank test with a theoretical median of 1. Box and whiskers show minimum to maximum values with all independent replicates, center denotes median, and the bounds denote the 25th to 75th percentiles.
- **D.** Weight loss of control (n= 7) or cisplatin-treated (n= 8) wildtype C57BL/6J mice, n=2 cohorts. Daily weight measurements were normalized to the starting (day 0) weight of each mouse to calculate % body weight. Significance determined by 2way ANOVA with Sidak's multiple comparisons test. Mean + standard deviation is shown.
- **E.** Colon length (cm) of the control (n= 7) or at day 7 post-cisplatin (n= 10), n=3 cohorts. Significance determined by unpaired t test. Box and whiskers show minimum to maximum values with all independent replicates, center denotes median, and the bounds denote the 25th to 75th percentiles.
- **F.** Spleen weight (grams) of the control (n= 7) or at day 7 post-cisplatin (n= 15), n=3 cohorts. Significance determined by unpaired t test. Box and whiskers show minimum to maximum values with all independent replicates, center denotes median, and the bounds denote the 25th to 75th percentiles.
- **G.** Tissue-associated Enterobacteriaceae levels within the indicated tissue compartments at 7 days post-cisplatin treatment. Colony forming units (CFU) per gram of tissue weight (n= 6-14 per group, n=3 cohorts). Significance determined by Mann Whitney test comparing each tissue independently. Box and whiskers show minimum to maximum values with all independent replicates, center denotes median, and the bounds denote the 25th to 75th percentiles.
- **H.** TUNEL positive cells per ileum tissue section area (mm^2) at indicated days post-cisplatin (n= 4 mice per group, averaged values of 5-10 sections per mouse shown). Significance determined by one-way ANOVA with Dunnett's multiple comparisons test. Box and whiskers show minimum to maximum values with all independent replicates, center denotes median, and the bounds denote the 25th to 75th percentiles.
- **I.** Alcian Blue-PAS positive cells per ileum tissue section area (mm^2) at indicated days post-cisplatin (n= 4 mice per group, averaged values of 5-10 sections per mouse shown). Mean + standard deviation is shown with individual replicated displayed.
- **J.** UEA1 positive cells per ileum tissue section area (mm^2) at indicated days post-cisplatin (n= 4 mice per group, averaged values of 5-10 sections per mouse shown). Significance determined by one-way ANOVA with Dunnett's multiple comparisons test.

Box and whiskers show minimum to maximum values with all independent replicates, center denotes median, and the bounds denote the 25th to 75th percentiles.

K. TUNEL positive cells per colon tissue section area (mm^2) at indicated days post-cisplatin (n= 4 mice per group, averaged values of 5-10 sections per mouse shown). Significance determined by one-way ANOVA with Dunnett's multiple comparisons test. Box and whiskers show minimum to maximum values with all independent replicates, center denotes median, and the bounds denote the 25th to 75th percentiles.

L. Alcian Blue-PAS positive cells per colon tissue section area (mm^2) at indicated days post-cisplatin (n= 4 mice per group, averaged values of 5-10 sections per mouse shown). Significance determined by one-way ANOVA with Dunnett's multiple comparisons test. Mean + standard deviation is shown with individual replicated displayed.

M. UEA1 positive cells per colon tissue section area (mm^2) at indicated days post-cisplatin (n= 4 mice per group, averaged values of 5-10 sections per mouse shown). Significance determined by one-way ANOVA with Dunnett's multiple comparisons test.

N. Weight loss of control Caspase 3/7$^{fl/fl}$ (n= 10) or Vil-Cre$^{+/-}$::Caspase 3/7$^{fl/lfl}$ (n= 6) mice following cisplatin treatment, n=2 cohorts. Daily weight measurements were normalized to the starting (day 0) weight of each mouse to calculate % body weight. Significance determined by 2way ANOVA. Mean + standard deviation is shown.

O. Colon length (cm) of the control (n= 10) or Vil-Cre$^{+/-}$::Caspase 3/7$^{fl/lfl}$ (n= 6) mice at day 7 post-cisplatin, n=2 cohorts. Significance determined by unpaired t test. Box and whiskers show minimum to maximum values with all independent replicates, center denotes median, and the bounds denote the 25th to 75th percentiles.

P. Spleen weight (grams) of the control (n= 10) or Vil-Cre$^{+/-}$::Caspase 3/7$^{fl/lfl}$ (n= 6) mice at day 7 post-cisplatin, n=2 cohorts. Significance determined by unpaired t test. Box and whiskers show minimum to maximum values with all independent replicates, center denotes median, and the bounds denote the 25th to 75th percentiles.

For A-P, ns $p > 0.05$, * $p \leq 0.05$, ** $p \leq 0.005$, *** $p \leq 0.0005$, **** $p \leq 0.0001$.

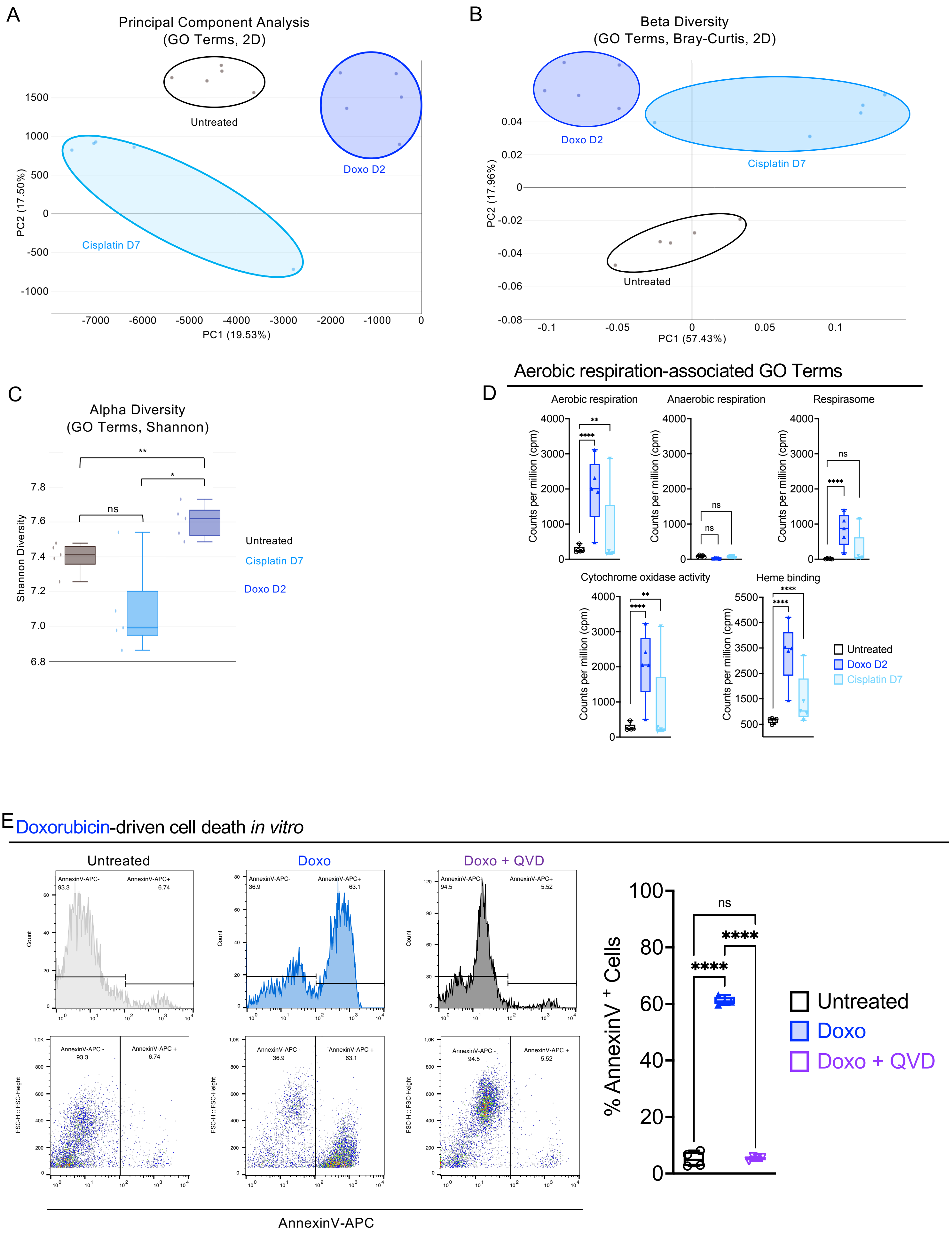
A
Principal Component Analysis
(GO Terms, 2D)
Untreated
Doxo D2
Cisplatin D7
PC2 (17.50%)
PC1 (19.53%)
1500
1000
500
0
-500
-1000
-7000
-6000
-5000
-4000
-3000
-2000
-1000
0
B
Beta Diversity
(GO Terms, Bray-Curtis, 2D)
Doxo D2
Cisplatin D7
Untreated
PC2 (17.96%)
PC1 (57.43%)
0.04
0.02
0
-0.02
-0.04
-0.06
-0.08
-0.1
-0.05
0
0.05
0.1
C
Alpha Diversity
(GO Terms, Shannon)
Shannon Diversity
**
*
ns
7.8
7.6
7.4
7.2
7.0
6.8
Untreated
Cisplatin D7
Doxo D2
Aerobic respiration-associated GO Terms
D
Aerobic respiration
Anaerobic respiration
Respirasome
Cytochrome oxidase activity
Heme binding
Counts per million (cpm)
4000
3000
2000
1000
0
5500
4500
3500
2500
1500
500
****
**
ns
Untreated
Doxo D2
Cisplatin D7
E Doxorubicin-driven cell death *in vitro*
Untreated
Doxo
Doxo + QVD
AnnexinV-APC-
AnnexinV-APC+
93.3
6.74
36.9
63.1
94.5
5.52
Count
FSC-H :: FSC-Height
AnnexinV-APC
% AnnexinV + Cells
100
80
60
40
20
0
ns
****
****
Untreated
Doxo
Doxo + QVD

Supplementary Figure 4 (corresponding with Main Text Figure 3)
Chemotherapy-induced transcriptional signature

- **A.** Principal Component Analysis (2D) of GO Term transcriptional pathways.
- **B.** Beta Diversity (2D) of GO Term transcriptional pathways.
- **C.** Alpha Diversity of GO Term transcriptional pathways via Shannon's diversity index.
- **D.** Total abundance (counts per million, cpm) of bacterial transcripts associated with aerobic respiration GO Terms. Statistical significance determined by 2way ANOVA with Dunnett's multiple comparisons test. Box and whiskers show minimum to maximum values with all independent replicates, center denotes median, and the bounds denote the 25th to 75th percentiles.
- **E.** Representative flow cytometry gates (left) of CT26 cells treated with doxorubicin or doxorubicin + QVD for 24 hours. X-axis: AnnexinV-APC. Y-axis: Forward scatter. Quantification of AnnexinV-positive cells (right). n= 4 per group. Box and whiskers show minimum to maximum values with all independent replicates, center denotes median, and the bounds denote the 25th to 75th percentiles. Statistical significant determined by one-way ANOVA with Tukey's multiple comparisons test.

For A-E, ns $p > 0.05$, * $p \leq 0.05$, ** $p \leq 0.005$, *** $p \leq 0.0005$, **** $p \leq 0.0001$.

Chemotherapy-induced death in mouse and human colonocytes

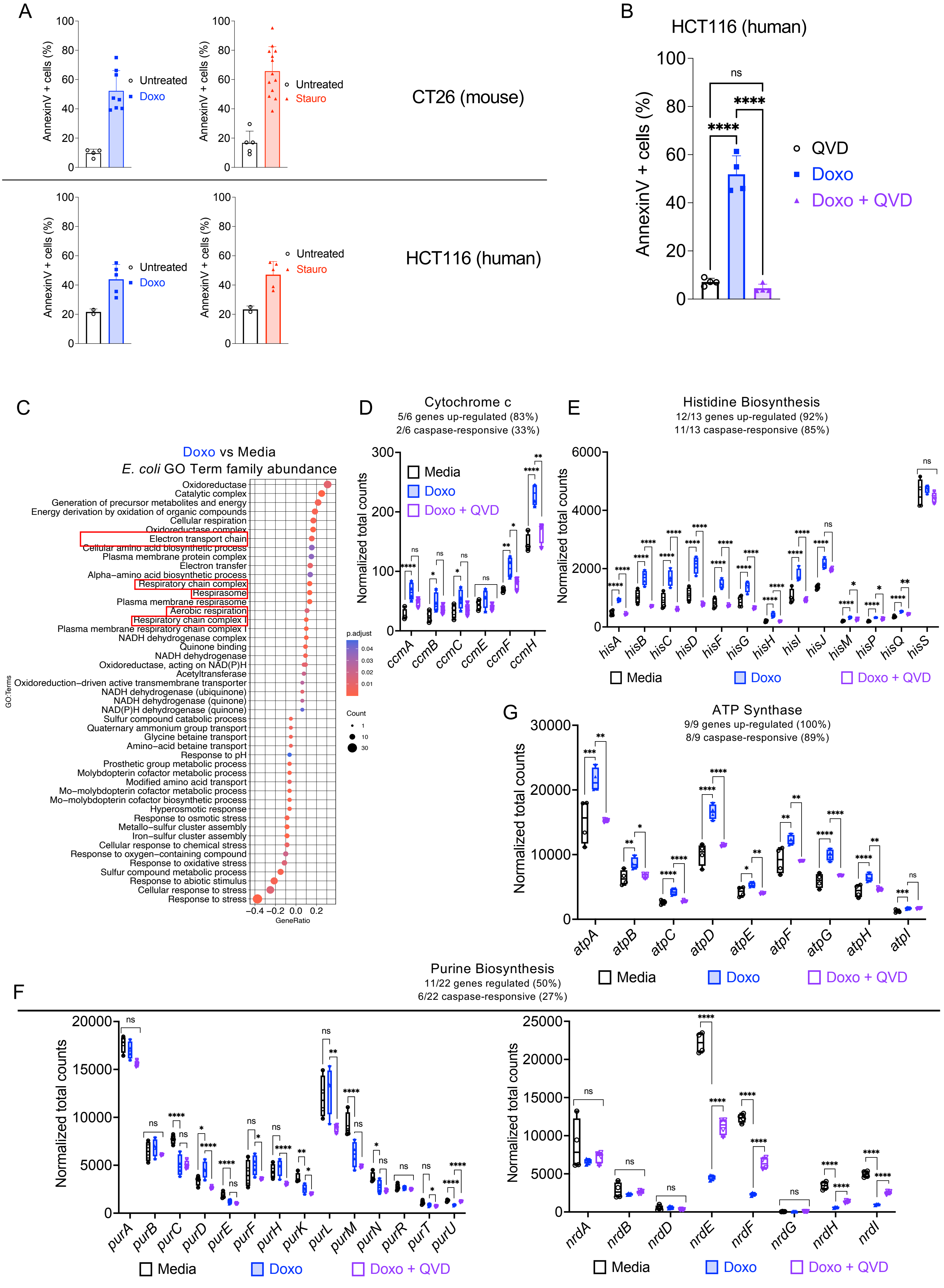

Supplementary Figure 5 (corresponding with Main Text Figure 3)
Death-dependent *E. coli* transcriptional signature

A. Quantification of AnnexinV-positive CT26 (top) or HCT116 (bottom) cells treated with either doxorubicin or staurosporine. n= 2-13 per group. Mean + standard deviation is shown with individual replicates displayed.

B. Quantification of AnnexinV-positive HCT116 cells after treatment with doxorubicin and/or QVD. n= 4 per group. Statistical significance determined by one-way ANOVA with Tukey's multiple comparisons test. Mean + standard deviation is shown with individual replicates displayed.

C. GO Term enrichment analysis of *E. coli* transcripts grown in doxorubicin-treated supernatants compared to media controls.

D. Normalized total transcript counts of the indicated cytochrome c genes. Box and whiskers show minimum to maximum values with all independent replicates, center denotes median, and the bounds denote the 25th to 75th percentiles.

E. Normalized total transcript counts of the indicated histidine biosynthesis genes. Box and whiskers show minimum to maximum values with all independent replicates, center denotes median, and the bounds denote the 25th to 75th percentiles.

F. Normalized total transcript counts of the indicated purine biosynthesis genes. Box and whiskers show minimum to maximum values with all independent replicates, center denotes median, and the bounds denote the 25th to 75th percentiles.

G. Normalized total transcript counts of the indicated ATP synthase genes. Box and whiskers show minimum to maximum values with all independent replicates, center denotes median, and the bounds denote the 25th to 75th percentiles.

For A-G, ns $p > 0.05$, * $p \leq 0.05$, ** $p \leq 0.005$, *** $p \leq 0.0005$, **** $p \leq 0.0001$.

For C-G n=4 per group. Media conditions contain doxorubicin. Statistical significance from RNAseq determined by pairwise comparisons with corrections for false discovery rate (see methods).

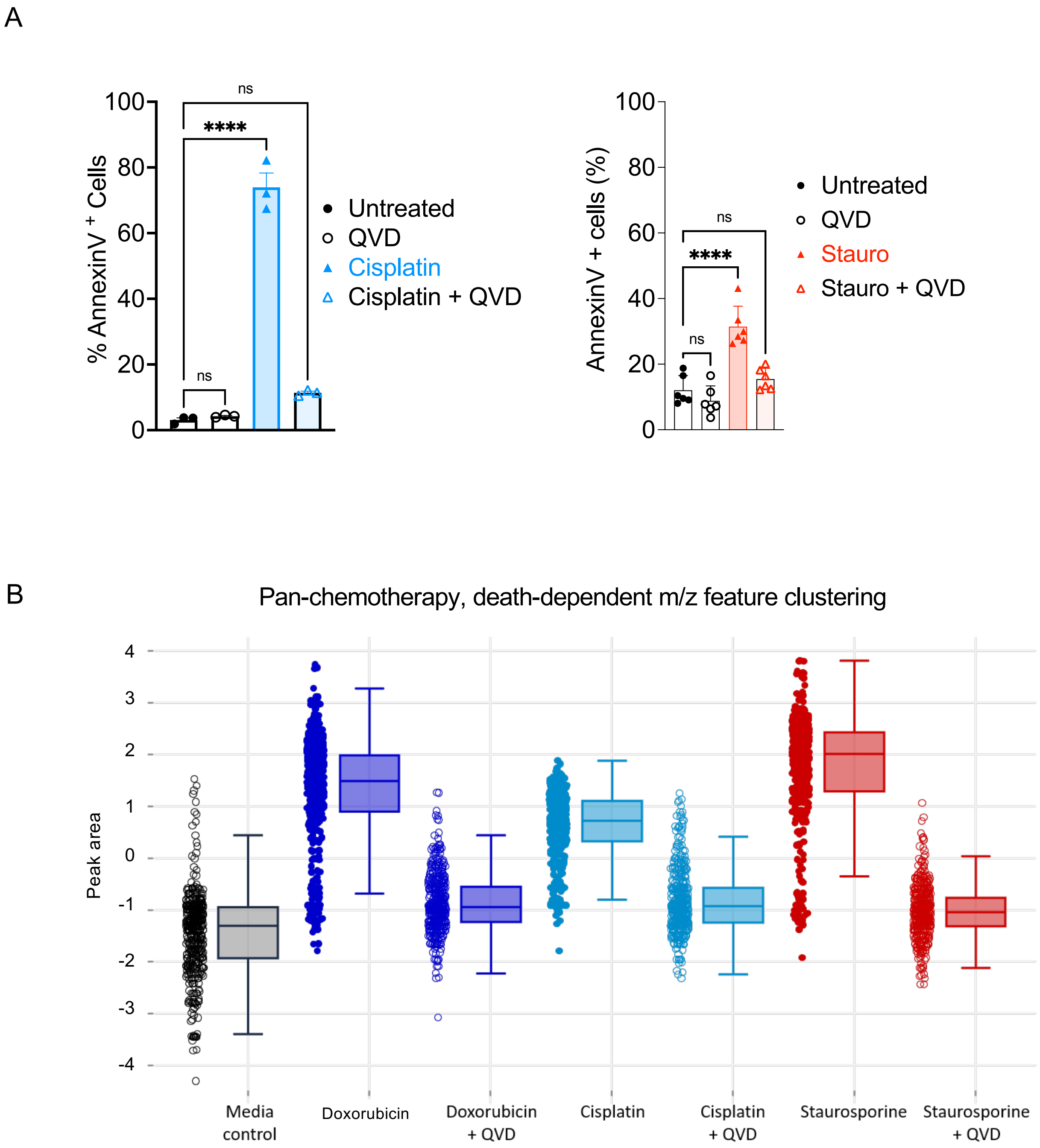
A
100
80
60
40
20
0
% AnnexinV + Cells
ns
****
ns
● Untreated
○ QVD
▲ Cisplatin
△ Cisplatin + QVD
100
80
60
40
20
0
AnnexinV + cells (%)
ns
****
ns
● Untreated
○ QVD
▲ Stauro
△ Stauro + QVD
B
Pan-chemotherapy, death-dependent m/z feature clustering
Peak area
4
3
2
1
0
-1
-2
-3
-4
Media control
Doxorubicin
Doxorubicin + QVD
Cisplatin
Cisplatin + QVD
Staurosporine
Staurosporine + QVD

Supplementary Figure 6 (corresponding with Main Text Figure 4)
Chemotherapy-induced metabolite release.

- **A.** Quantification of AnnexinV-positive CT26 cells after treatment with cisplatin (left, n=3 per group) or staurosporine (Stauro, right, n=6 per group) and/or QVD. Statistical significance determined by one-way ANOVA with Tukey's multiple comparisons test. Mean + standard deviation is shown with individual replicates displayed.
- **B.** Hierarchical clustering performed on significant features from Figure 4B, as similarly shown in Figure 4C. *m/z* ion intensities are ArcSinh-transformed and pareto scaled.

Death-dependent metabolites reduce *de novo* purine synthesis pathway

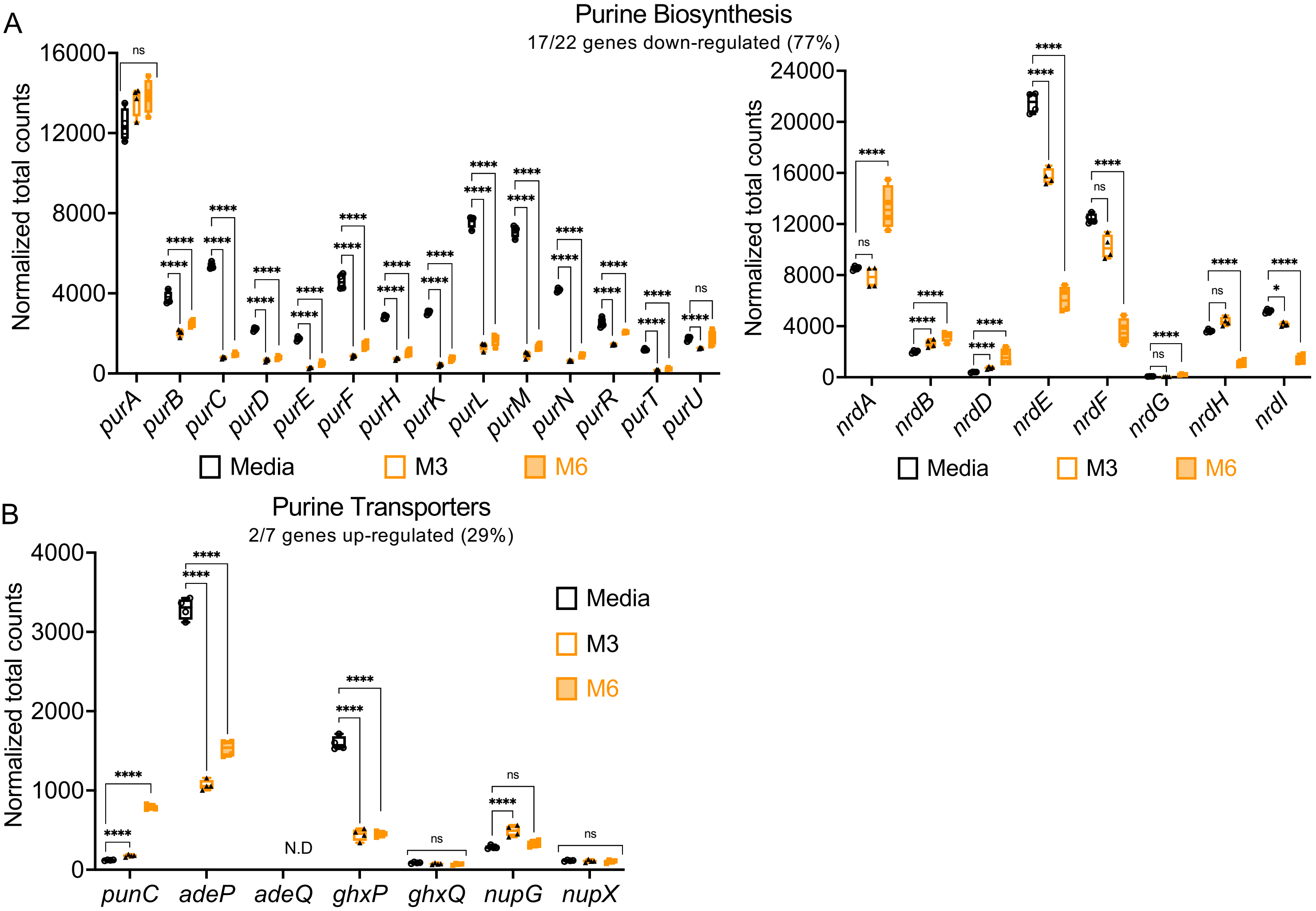

Metabolites recapitulate death-dependent histidine synthesis and energy favorability

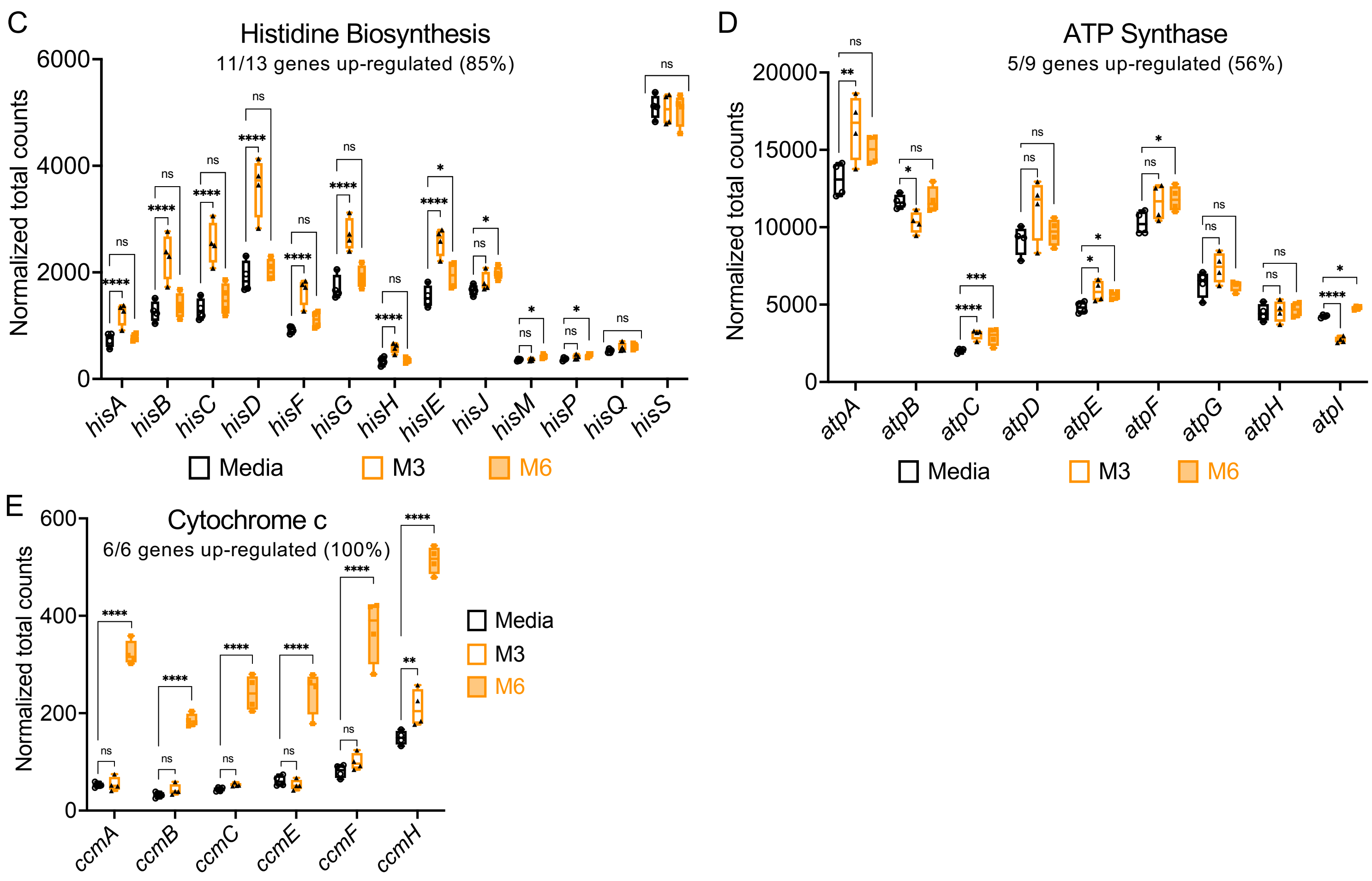

Supplementary Figure 7 (corresponding with Main Text Figure 5)
Metabolites rewire *E. coli* transcription.

- **A.** Normalized total transcript counts of the indicated purine biosynthesis genes.
- **B.** Normalized total transcript counts of the indicated purine transporter genes.
- **C.** Normalized total transcript counts of the indicated histidine biosynthesis genes.
- **D.** Normalized total transcript counts of the indicated ATP synthase genes.
- **E.** Normalized total transcript counts of the indicated cytochrome c genes.

For A-E: ns $p > 0.05$, * $p \leq 0.05$, ** $p \leq 0.005$, *** $p \leq 0.0005$, **** $p \leq 0.0001$. Box and whiskers show minimum to maximum values with all independent replicates, center denotes median, and the bounds denote the 25th to 75th percentiles. Statistical significance from RNAseq determined by pairwise comparisons with corrections for false discovery rate (see methods).

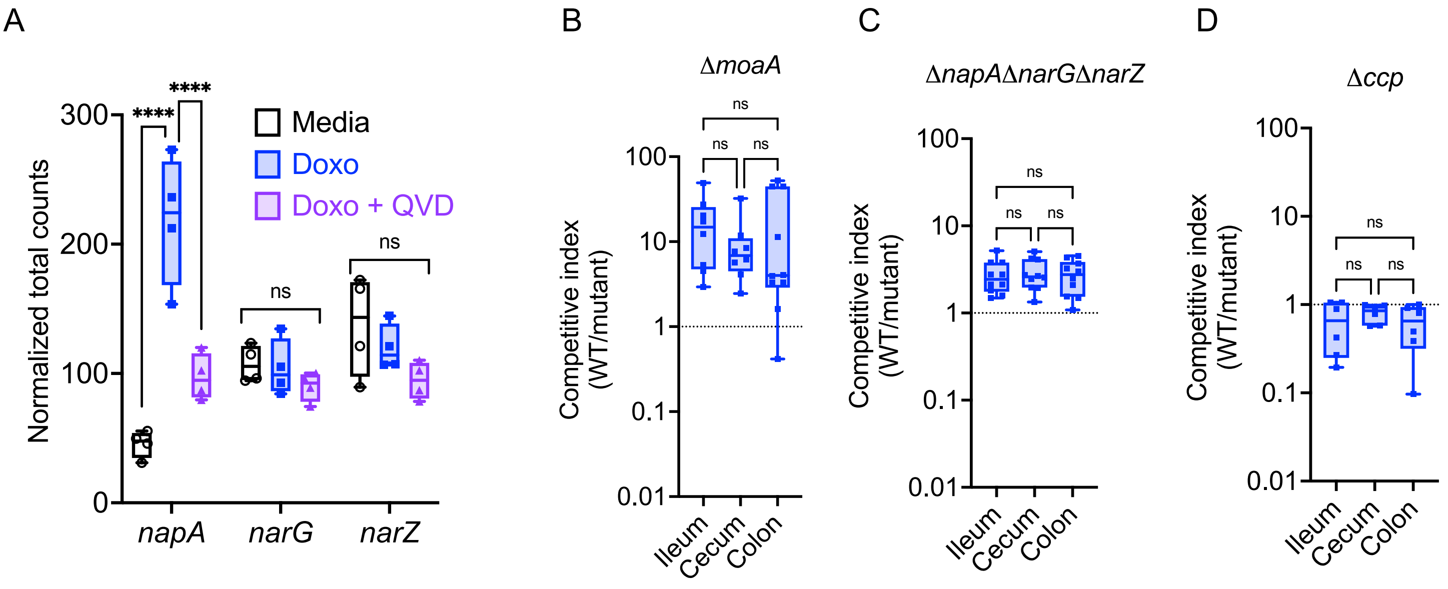

Doxorubicin reduces expression and fitness requirement for high-affinity, low oxygen abundance, cytochrome CydAB

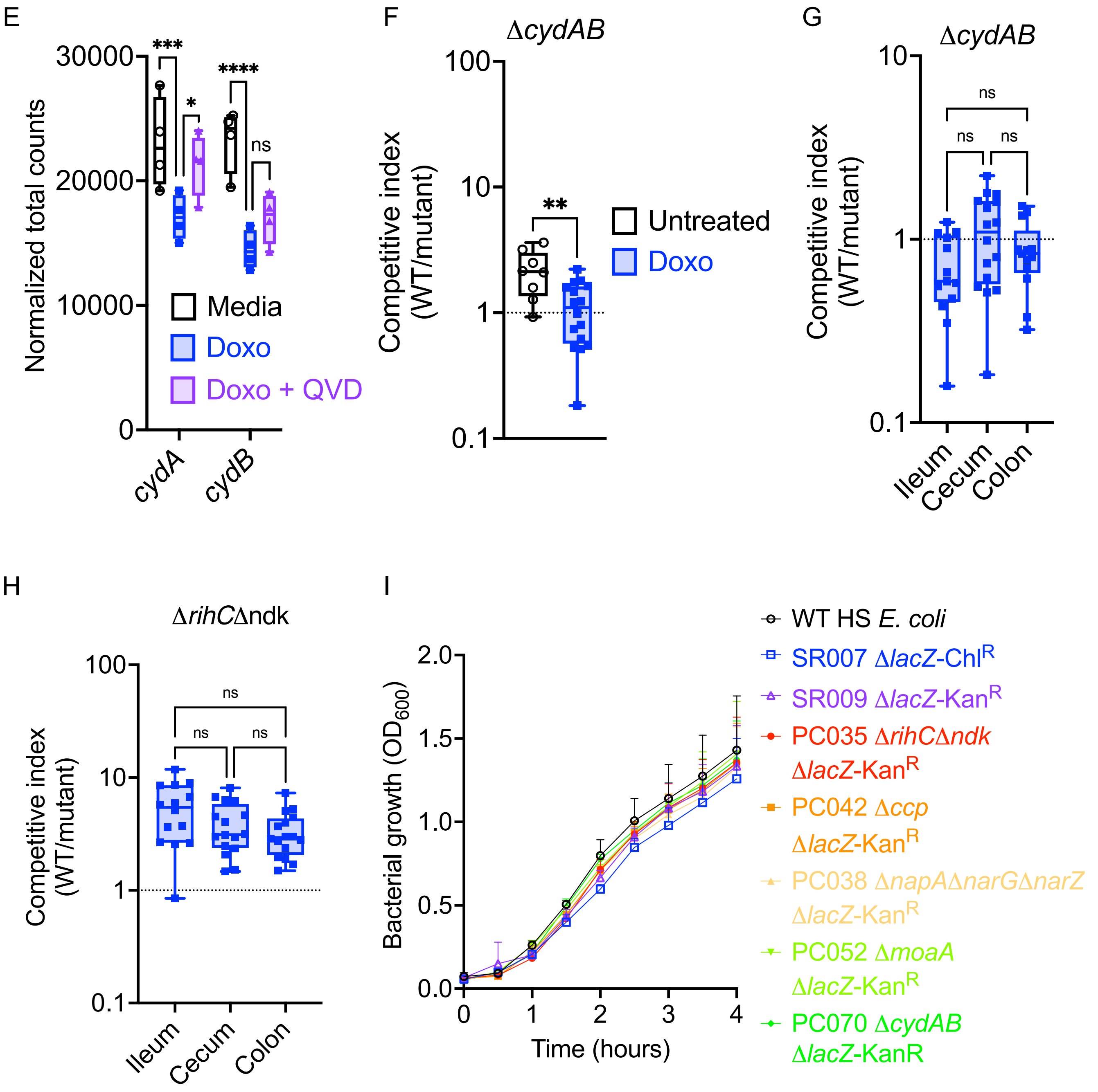

Supplementary Figure 8 (corresponding with Main Text Figure 5)
Chemotherapy-driven changes in *E. coli* fitness.

- **A.** Normalized total transcript counts of the indicated nitrate reductase genes.
- **B.** Competitive index of wildtype (SR007) vs Δ*moaA* (PC052) in the indicated intestinal tissue post doxorubicin treatment. n=8 mice per group, n=2 cohorts.
- **C.** Competitive index of wildtype (SR007) vs Δ*napA*Δ*narG*Δ*narZ* (PC038) in the indicated intestinal tissue post doxorubicin treatment. n=10 mice per group, n=3 cohorts.
- **D.** Competitive index of wildtype (SR007) vs Δ*ccp* (PC042) in the indicated intestinal tissue post doxorubicin treatment. n=6 mice per group, n=2 cohorts.
- **E.** Normalized total transcript counts of the indicated *cydA* and *cydB* genes.
- **F.** Competitive index of wildtype (SR007) vs Δ*cydAB* (PC070). n= 8-16 mice per group, n=4 cohorts. Statistical significance determined by Mann-Whitney test.
- **G.** Competitive index of wildtype (SR007) vs Δ*cydAB* (PC070). n=8-16 mice per group, n=4 cohorts.
- **H.** Competitive index of wildtype (SR007) vs Δ*rihC*Δ*ndk* (PC035). n=6-16 mice per group, n=3 cohorts.
- **I.** Bacterial growth as measured by OD_{600} measurements over time of the indicated bacterial strain. Mean + standard deviation is shown. n=4 per strain.

For A-I: ns $p > 0.05$, * $p \leq 0.05$, ** $p \leq 0.005$, *** $p \leq 0.0005$, **** $p \leq 0.0001$. Box and whiskers show minimum to maximum values with all independent replicates, center denotes median, and the bounds denote the 25th to 75th percentiles.

For B-D, G-H: Statistical significance determined by Kruskal-Wallis test with Dunn's multiple comparisons test.

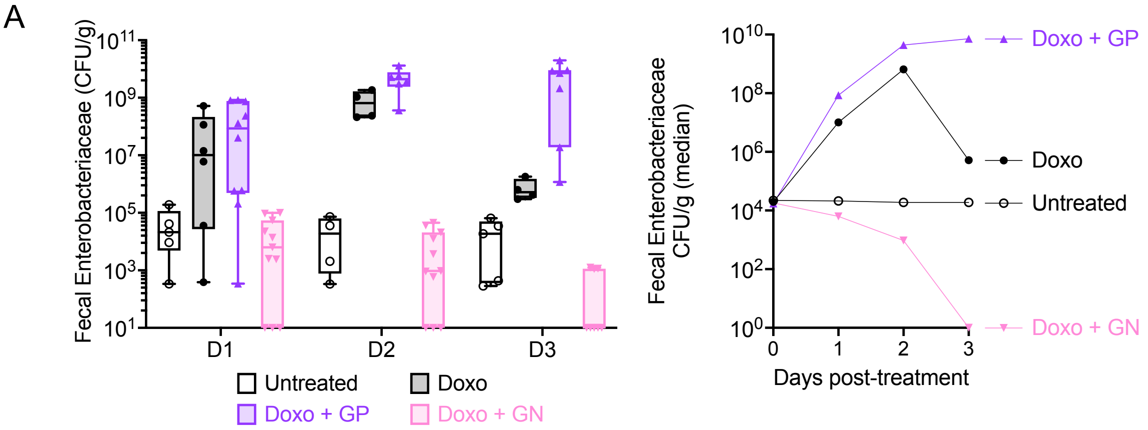
A
Fecal Enterobacteriaceae (CFU/g)
10^{11}
10^{9}
10^{7}
10^{5}
10^{3}
10^{1}
D1
D2
D3
☐ Untreated
▨ Doxo
▨ Doxo + GP
▨ Doxo + GN
Fecal Enterobacteriaceae CFU/g (median)
10^{10}
10^{8}
10^{6}
10^{4}
10^{2}
10^{0}
0
1
2
3
Days post-treatment
Doxo + GP
Doxo
Untreated
Doxo + GN

Supplementary Figure 9 (corresponding with Main Text Figure 6)
Antibiotics alter intestinal Enterobacteriaceae.

- **A.** Enterobacteriaceae CFU. CFU in feces at the indicated times of each antibiotic treatment group post-doxorubicin treatment (n= 4-11 per time per treatment). The median CFU per gram of feces for each treatment group is plotted over time (right). Box and whiskers show minimum to maximum values with all independent replicates, center denotes median, and the bounds denote the 25th to 75th percentiles.

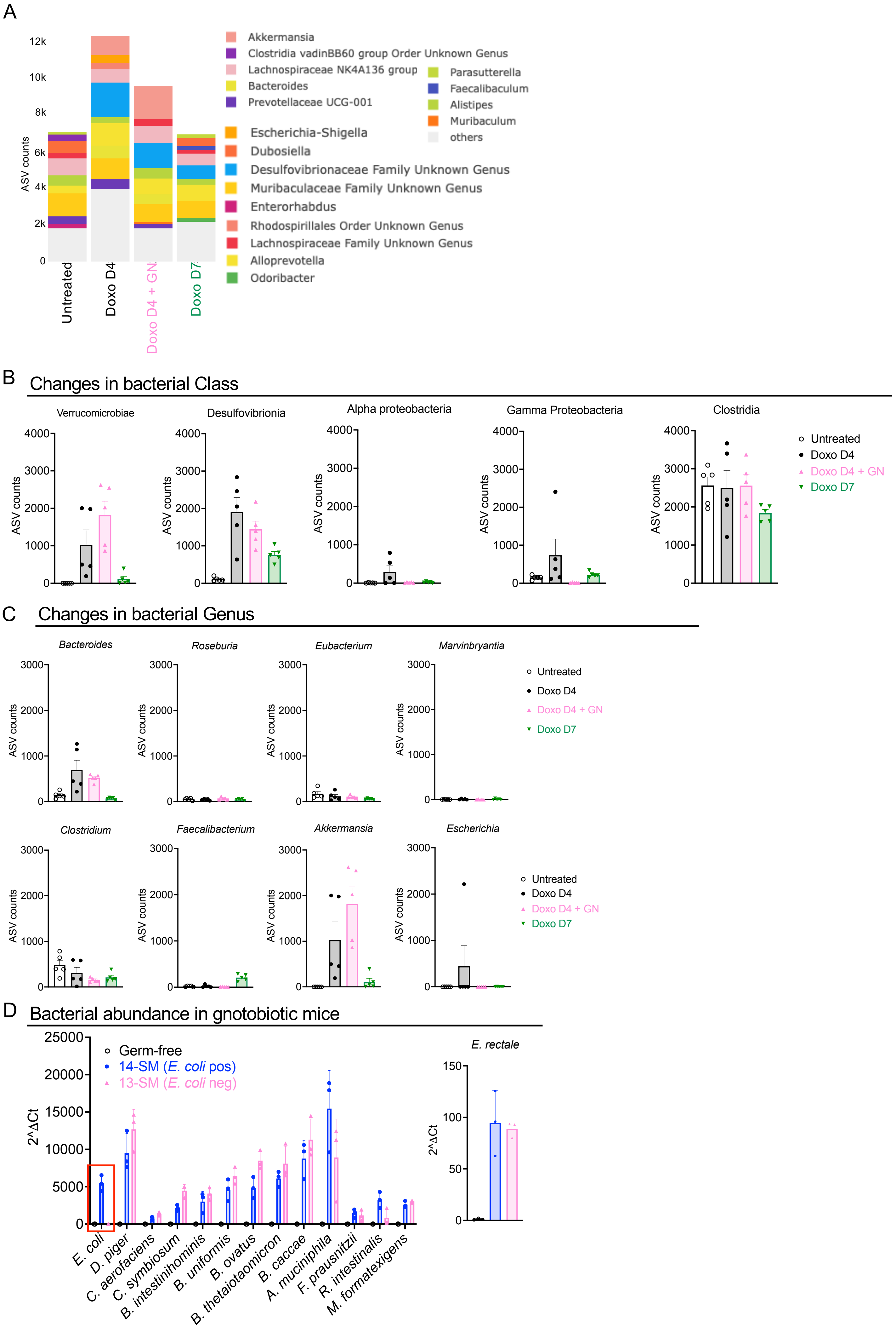
A
12k
10k
8k
6k
4k
2k
0
ASV counts
Untreated
Doxo D4
Doxo D4 + GN
Doxo D7
Akkermansia
Clostridia vadinBB60 group Order Unknown Genus
Lachnospiraceae NK4A136 group
Bacteroides
Prevotellaceae UCG-001
Parasutterella
Faecalibaculum
Alistipes
Muribaculum
others
Escherichia-Shigella
Dubosiella
Desulfovibrionaceae Family Unknown Genus
Muribaculaceae Family Unknown Genus
Enterorhabdus
Rhodospirillales Order Unknown Genus
Lachnospiraceae Family Unknown Genus
Alloprevotella
Odoribacter
B
Changes in bacterial Class
Verrucomicrobiae
Desulfovibrionia
Alpha proteobacteria
Gamma Proteobacteria
Clostridia
4000
3000
2000
1000
0
ASV counts
Untreated
Doxo D4
Doxo D4 + GN
Doxo D7
C
Changes in bacterial Genus
Bacteroides
Roseburia
Eubacterium
Marvinbryantia
Clostridium
Faecalibacterium
Akkermansia
Escherichia
3000
2000
1000
0
ASV counts
Untreated
Doxo D4
Doxo D4 + GN
Doxo D7
D
Bacterial abundance in gnotobiotic mice
25000
20000
15000
10000
5000
0
2^ΔCt
Germ-free
14-SM (E. coli pos)
13-SM (E. coli neg)
E. coli
D. piger
C. aerofaciens
C. symbiosum
B. intestinihominis
B. uniformis
B. ovatus
B. thetaiotaomicron
B. caccae
A. muciniphila
F. prausnitzii
R. intestinalis
M. formatexigens
E. rectale
150
100
50
0
2^ΔCt

Supplementary Figure 10 (corresponding with Main Text Figure 7)
Time and antibiotic-dependent microbial changes.

- **A.** Bacterial genus composition, based on total ASV counts, within the indicated treatment conditions.
- **B.** Total ASV counts of the indicated bacterial Class within the indicated treatment conditions. Mean + standard deviation with individual replicates is shown.
- **C.** Total ASV counts of the indicated bacterial Genus within the indicated treatment conditions. Mean + standard deviation with individual replicates is shown.
- **D.** Bacterial species abundance in 14-SM or 13-SM re-colonized mice via qPCR. Ct values from technical duplicates were averaged and delta Ct values were calculated as (germ-free control group average) – (individual test mouse value) for each species, and then 2^delta Ct was calculated. Mean + standard deviation with individual replicates is shown.